IN VIVO CORONARY WALL SHEAR STRESS DETERMINATION USING CT, MRI, AND COMPUTATIONAL FLUID DYNAMICS

A Dissertation
Presented to
The Academic Faculty

by

Kevin Robert Johnson

In Partial Fulfillment
of the Requirements for the Degree
Doctor of Philosophy in the
School of Biomedical Engineering

Georgia Institute of Technology
and
Emory University
May 2007

IN VIVO CORONARY WALL SHEAR STRESS DETERMINATION USING CT, MRI, AND COMPUTATIONAL FLUID DYNAMICS

Approved by:

John N. Oshinski, Ph.D., Advisor
School of Biomedical Engineering
Georgia Institute of Technology / Emory University

Stefan Tigges, M.D.
School of Medicine
Department of Radiology
Emory University

Don P. Giddens, Ph.D.
College of Engineering
Georgia Institute of Technology

Andrew Karellas, Ph.D.
School of Medicine
Department of Radiology
Emory University

W. Robert Taylor, Ph.D., M.D.
School of Medicine
Department of Cardiology
Emory University

Date Approved: March 14, 2007

For family…

ACKNOWLEDGEMENTS

The saying goes that it takes a village to raise a child. The same is undoubtedly true for the final completion of my formal education.

I must start with those that raised the child, most notably my parents Gary and Judy Johnson. From kindergarten to graduate school, they have supported me in ways that can not be described or surpassed. It was their belief as I was growing up that learning was my job. And since learning isn't a very lucrative profession, they were always there to see that my needs were always met until I could stand on my own. Any perceived success of mine is owed to them. And what of my younger brother David? You didn't get yours before I did; but I know your determination won't let you stop before you've realized your own goals. God has great things in store for you and your intellect will benefit the masses. If your drive can at all be attributed to sibling rivalry, then I am honored for it. I must also thank my grandparents Robert Cecil and Laura Gentry for instilling the importance of education in their children as well as the importance of family. Granddaddy earned his Ph.D. while being a husband and raising a family. He also typed his entire dissertation on a typewriter which to me seems almost as daunting. I can only aspire to one day be the scholar, husband, and father that he was. Beyond these immediate family members, I have been blessed with an extended family that has been incredibly supporting and loving along every step of my journey.

Perhaps as important as what research you do is who you do it under. My path did not go exactly according to the original plan; but I could not have had the privilege of a better advisor than Dr. John Oshinski. For five years, he has been a source of guidance,

encouragement, and sometimes not so gentle prodding for me to get things done – but in a good way. All this plus he can always be counted on for serious debate about ACC sports. What else could you ask for? I must also thank Puneet Sharma who, along with John, mentored me in the realm of MRI. Puneet also paved the way as John's first graduated Ph.D. student at Georgia Tech – even if it seems he still hasn't technically left the lab.

Now for my partners in crime. I've spent four years sitting next to Jana Delfino. If we didn't get along so well, I'm sure we'd have driven each other crazy. As it stands, I think we've succeeded in keeping each other sane. Despite what you claim, I'm sure you'll survive the three months in the lab without me. I know that you will be able to handle whatever comes your way – including your impending motherhood. To all the other past and present cave dwellers – Binjian, Brandon, Smbat, Trevor, Rick, Marijn, Hui, Bob, Thomas, and Charles, I thank you for your part in making life in a windowless, underground lab bearable and even enjoyable at times.

For making my life outside of the windowless, underground lab bearable and even enjoyable a lot of the time, I thank the community of Dunwoody United Methodist Church and especially my many Disciple Bible study groups, Reverend Stephen Streett, and the 180° youth ministry. The time I have spent with these groups has been a true blessing. I have known Stephen for almost fifteen years and in that time he has been a minister, mentor, coach, and now colleague and trusted friend. If God sees fit to lead my life away from Atlanta, a large part of my heart will remain with these ministries.

I'm sure the following will read like a laundry list; but these people must be mentioned. Marvis Zanders is tremendous in her support of the Fritz Philips MRI lab. If

you ever need something greased, she's your squeaky wheel. I must also thank the administrative staff of the BME department including Leita Young, Beth Bullock, and Sally Gerrish and previously Pat Fowler and Chris Ruffin for always making things run smoothly in a new program. Dr. Salil Patel did much of the early work for Chapter 3 of this dissertation. Dr. Gopi Sirineni and Dr. Krishna Patel provided their expertise for Chapter 4. They also provided an enlightening conference weekend of Indian music and lessons in the rules of cricket. Any CT experiments would not have been possible without Melissa or Lucienne behind the controls. Similarly, I am greatly indebted to Bobbie Burrow and the numerous MRI staff at Emory Hospital for their friendship, guidance, and maybe sometimes tolerance. The completion of MRI studies in Chapter 5 could not have been possible without the help of Dr. Steven Lloyd at the University of Alabama at Birmingham who gave us time on his scanner when Emory decided to remove the 3.0T scanner from the hospital. Sam Fielden devised the vessel sharpness technique used in Chapter 4 and wrote MATLAB code in 2 hours that certainly would have taken me 2 weeks. Dr. Tracy Faber provided both the DICOM header extraction program used in Chapter 6 and the physical subjects who were borrowed from her FUSION study along with Dr. Cesar Santana.

Finally, I must thank whoever is reading this – for it means either that you have been an influential part of my life or that perhaps my work will be influential in yours. Thank you all.

TABLE OF CONTENTS

LIST OF TABLES

LIST OF FIGURES

LIST OF ABBREVIATIONS

WSS	wall shear stress
CFD	computational fluid dynamics
CT	computed tomography
MRI	magnetic resonance imaging
PC-MRI	phase contrast magnetic resonance imaging
SNR	signal to noise ratio
T	Tesla
EC	endothelial cell
ICAM	intercellular adhesion molecule
VCAM	vascular cell adhesion molecule
ECG	electrocardiogram
CTCA	computed tomography coronary angiography
bpm	beats per minute
MRA	magnetic resonance angiography
RCA	right coronary artery
IVUS	intravascular ultrasound
LAD	left anterior descending coronary artery
LCX	left circumflex coronary artery
CC	cranial-caudal
RL	right-left
AP	anterior-posterior
keV	kiloelectron volt
mA	milliamp

MPR	multiplanar reconstruction
PVA	polyvinyl alcohol
FLASH	fast low angle shot
FOV	field of view
TR	repetition time
TE	echo time
ROI	region of interest
RMS	root mean squared
StdDev, sd	standard deviation
IRB	Institutional Review Board
LM	left main coronary artery
DICOM	digital imaging and communications in medicine
NURBS	nonuniform rational B-spline

LIST OF SYMBOLS

t_{rot}	rotation time
τ	wall shear stress
η	viscosity
∇	gradient vector
ν	velocity
$\frac{\partial \nu}{\partial r}$	partial derivative of velocity with respect to radius
Q	volumetric flow rate
D	diameter
$\Delta x, \Delta y, \Delta z$	incremental displacement in x, y, and z directions
r	Pearson's correlation coefficient
α	flip angle
$flow_{collection}$	collected flow
$flow_{PC\text{-}MRI}$	flow measured by PC-MRI
N	number of measurements
$N \cdot s/m^2$	Newton-second per meter-squared

SUMMARY

Wall shear stress (WSS) has long been identified as a factor in the development of atherosclerotic lesions. Autopsy studies have revealed a strong tendency for lesion development at arterial branch sites and along the inner walls of curvature – areas that, in theory, should experience low WSS. Calculations of coronary artery WSS have typically been based upon average models of coronary artery geometry with average flow conditions and then compared to average lesion distributions. With all the averaging involved, a more detailed knowledge of the correlation between WSS and atherosclerotic lesion development might be obscured. Recent advancements in hemodynamic modeling now enable the calculation of WSS in individual subjects. An image-based approach for patient-specific calculation of *in vivo* WSS using computational fluid dynamics (CFD) would allow a more direct study of this correlation. New state-of-the-art technologies in multi-detector computed tomography (CT) and 3.0 Tesla magnetic resonance imaging (MRI) offer potential improvements for the measurement of coronary artery geometry and blood flow.

The overall objective of this research was to evaluate the quantitative accuracy of multi-detector CT and 3.0 Tesla MRI and incorporate those imaging modalities into a patient-specific CFD model of coronary artery WSS. Using a series of vessel motion phantoms, it has been shown that 64-detector CT can provide accurate measurements of coronary artery geometry for heart rates below 70 beats per minute. A flow phantom was

used to validate the use of navigator-echo gated, phase contrast MRI at 3.0 Tesla to measure velocity of coronary blood flow. Patient-specific, time-resolved CFD models of coronary WSS were created for two subjects. Furthermore, it was determined that population-average velocity curves or steady state velocities can predict locations of high or low WSS with high degrees of accuracy compared to the use of patient-specific blood flow velocity measurements as CFD boundary conditions. This work is significant because it constitutes the first technique to non-invasively calculate *in vivo* coronary artery WSS using image-based, patient-specific modeling.

CHAPTER 1

INTRODUCTION

Introduction

Wall shear stress (WSS) is the force that a moving fluid exerts on its boundaries in the direction of flow. In the physiological setting, it is the friction-like, shearing force that is felt by endothelial cells that line the walls of blood vessels. Low or oscillatory WSS has been shown to have a significant effect on many factors in the development of atherosclerotic lesions. While the majority of studies investigating the relationship between WSS and atherosclerosis involve *in vitro* experiments that examine protein expression and signaling at the cellular level, other work has sought to correlate the spatial distribution of atherosclerotic lesions with the magnitude of WSS experienced at those locations of the vasculature.

Autopsy studies have revealed a strong tendency for lesion development at arterial branch sites and along the inner walls of curvature – areas that, in theory, should experience low WSS. It is difficult, however, to observe or calculate the flow and WSS in an autopsy specimen. For this reason, calculations of coronary artery WSS have been based upon models of coronary artery geometry. These models are usually created using *average* measurements and *average* flow conditions and then compared to an *average* pathology distribution of lesions. With all the averaging involved, a more detailed knowledge of the correlation between WSS and atherosclerotic lesion development might be obscured. It follows that a method to compare WSS and disease distribution in a non-invasive, patient-specific manner would be desirable.

Current imaging modalities such as computed tomography (CT) and magnetic resonance imaging (MRI) allow for determination of vessel geometry and diameter; but determination of *in vivo* WSS has proven more elusive. To do so requires knowledge of the velocity profile within the blood vessel. An MRI technique known as phase contrast MRI (PC-MRI) can measure *in vivo* flow in the coronary arteries but lacks the spatial resolution required to obtain a full profile across the vessel. If, as it appears, it is not possible to directly measure *in vivo* WSS, one is forced to return to the approach of a model; but now using patient-specific parameters.

The approach to modeling that will be employed is computational fluid dynamics (CFD) which can perform complex simulation and analysis of the Navier-Stokes equations for fluid flow within a given volume. With a three-dimensional model of the fluid volume and defined boundary conditions at the inlet and outlet of that volume, CFD is able to calculate the flow conditions at any point within the volume. This is accomplished by breaking the large volume up into thousands of minute volume elements and then iteratively applying the laws of continuity and conservation of mass to each element through the entirety of the volume until a solution is reached that satisfies all boundary conditions.

Motivation

The development of multi-detector CT scanners and increased field strength MRI scanners continues to advance the capabilities of their respective imaging modalities. New three-dimensional reconstruction and visualization techniques available with 64-detector CT platforms can generate vessel models that can be used in CFD analysis.

Increases in signal-to-noise ratio (SNR) allow improved spatial resolution with 3.0T MRI and offer a new level of accuracy for coronary flow measurements. In their clinical setting, however, both of these modalities are used primarily in a qualitative fashion. *Quantitative evaluation of 64-detector CT measurements and 3.0T PC-MRI has not been performed.* Nor have the two techniques been paired with CFD for patient-specific modeling of coronary artery WSS. Combination of these two imaging modalities with CFD would constitute a powerful tool for performing hemodynamic studies.

Problem Statement

While either CT or MRI can identify the presence of lumen constricting lesions, they are not well suited for study of lesion composition. This information is also desirable and only available by histological methods following autopsy or biopsy. Histology studies differentiate between a stable plaque and "vulnerable" plaque. Stable plaques have a predominantly fibrous composition and have low risk for rupture. Vulnerable plaques, on the other hand, are characterized by lipid pools covered by a thin fibrous cap that is prone to rupture and cause clotting that can lead to heart attack or stroke[2, 3]. The relationship between lesion composition and hemodynamics remains unknown and uninvestigated due to the lack of patient-specific hemodynamics and histology studies.

An ideal situation would be to examine the coronary arteries by CT and MRI, calculate WSS, and then have the arteries available for histological study. This opportunity indeed presents itself in heart transplant patients who can be imaged prior to their transplant. Unfortunately, most heart failure patients on the transplant list have

implanted devices such as pacemakers or defibrillators that exclude them from MRI. This leads to another question that needs to be explored: are patient-specific blood flow boundary conditions necessary for accurate WSS calculations? If an average velocity waveform can be used as boundary conditions while maintaining the validity of the calculated WSS distribution, obtaining patient-specific velocity information by a lengthy MRI session becomes unnecessary. Therefore, *this thesis intends to evaluate the quantitative accuracy of the imaging modalities involved in creating a patient-specific CFD model of coronary WSS as well as determine the importance of patient-specific flow for such a model.*

Approach

In any quantitative evaluation, it is important to have known reference values with which to compare the measurements that are being evaluated. Imaging of human subjects to accomplish this task is not feasible due to the uncontrollable nature of the human body. Instead, a series of "phantoms" will be used that can have known geometries and controllable motion and flow conditions. A phantom is any sample or model that takes the place of a human body during imaging. Phantoms are used extensively in the calibration of both CT and MRI. In this thesis, a motion phantom will be designed and used to evaluate the accuracy of CT geometry reconstructions. A flow phantom will be designed and used to evaluate the accuracy of flow measurements obtained by 3.0T PC-MRI.

In order to design a motion phantom, it is necessary to have an understanding of what motion a human coronary artery experiences *in vivo*. To this end, a preliminary

study must be done to define coronary artery motion. This can be achieved through analysis of bi-plane coronary angiography studies. These studies record the motion of the coronary arteries over time as contrast media is injected directly into the arteries by a catheter. Landmarks can be identified in both views at branch points of the arteries and traced frame by frame over the cardiac cycle. The recording of two orthogonal views allows for the calculation of a three-dimensional path of motion.

With coronary motion defined, it is then possible to create a CT vessel phantom capable of replicating that motion. With a vessel model of known geometry, the accuracy of CT volume reconstruction under *in vivo* conditions can be evaluated. Similarly, the accuracy of 3.0T PC-MRI can be studied using a flow pump and a vessel phantom.

Next, an image based three-dimensional model defined by CT must be created and combined with PC-MRI velocity data to form a computational fluid dynamics simulation of blood flow through a patient's coronary arteries. Once this model is established, boundary conditions can be altered to investigate the importance of patient-specific velocity compared to a standard, "average" velocity waveform or even steady flow.

Thesis Organization

The organization of this thesis closely follows the progression of experiments detailed above. Each chapter, while providing a necessary piece of the overall research puzzle, can also be read as an individual study with a focus separate from the other chapters. This style of organization is appropriate given the variety of topics that are covered.

Chapter 2 provides additional background regarding previous studies of the relationship between atherosclerosis and WSS. It includes a basic overview of the MRI and CT imaging modalities and their use in cardiac imaging applications. Finally, it discusses previous attempts to model or calculate *in vivo* WSS.

Chapter 3 details coronary artery motion through a study of angiography cines. First, motion of the coronary arteries in several patients is aggregated for the purpose of creating a series of reference motion trajectories for future phantom studies. Then the motion is also analyzed to identify periods of the cardiac cycle during which the coronary arteries are at rest or moving at a slower velocity.

Chapter 4 involves the development and use of a moving CT imaging phantom to evaluate the accuracy of 64-detector CT in measuring features of coronary geometry. This is done through a series of imaging sessions with a range of heart rates. Diameters will be measured on vessel phantoms of differing size.

Chapter 5 is an evaluation of small diameter vessel velocity measurements by 3.0T PC-MRI. Using another vessel phantom, repeated scans will be acquired over a range of velocities and flow rates typical of coronary artery flow.

Chapter 6 serves to bring the previous two chapters together for a singular purpose in the creation of a CFD model of coronary flow using 64-detector CT to define the vessel boundaries and 3.0T PC-MRI to define velocity boundary conditions. Flow simulations then determine the necessity of patient-specific velocity information.

Chapter 7 contains a recap of what is detailed in this body of work, draws some general conclusions, discusses the potential impact of these findings, and makes suggestions for future paths of investigation to build upon this work.

CHAPTER 2

CLINICAL BACKGROUND AND SIGNIFICANCE

Wall Shear Stress and Atherosclerosis

Wall shear stress (WSS) has long been implicated as a factor in the development of atherosclerotic lesions. WSS is the frictional drag force that blood exerts on the wall of blood vessels in the direction of flow. At the cellular level, *in-vitro* studies have shown a relationship between WSS and endothelial cell (EC) morphology[4-6], EC attachment to the extracellular matrix[7-10], and production of cell surface proteins that increase monocyte adhesion, such as ICAM and VCAM[11, 12]. From these studies, it is clear that low or oscillatory WSS enables a series of events that affect EC function in ways associated with early development of atherosclerosis.

On a macroscopic level, regions of low or oscillating WSS have also been linked to early atherosclerotic lesions, intimal thickening, and plaque rupture[13-19]. Studies of autopsy specimens have shown that lesions are more likely to occur at specific sites such as inner walls of curvature, branch points, and bifurcations[15, 20-23]. Model or flow studies examining local hemodynamics in these areas have suggested a link to low WSS[17, 24-26]. These studies, however, were conducted in average models of vessel geometry using average blood flow velocity waveforms. Since there is significant variation in coronary geometry between individuals [27] and areas of low and high shear stress may be very close together, comparing WSS results from *average* models to

average lesion distributions may be unreliable in identifying the exact relationship between WSS and atherosclerosis.

Coronary Artery Imaging

There are several different imaging modalities that are currently used in the clinical setting to examine the coronary arteries. Among these are CT, MRI, intravascular ultrasound, and x-ray angiography. Cardiac catheterization with x-ray angiography is the diagnostic gold standard for coronary visualization and identification of the presence and degree of lumen narrowing. While it is a common procedure, it is invasive and not without risk of adverse events[28]. For the purposes of developing a three-dimensional model for WSS analysis, x-ray angiography results in only a 2D image. Bi-planar angiography can be used to create a three-dimensional frame but assumptions must be made regarding the cross-sectional shape of the vessel lumen[29]. Another invasive technique, intravascular ultrasound yields very detailed images of the vessel lumen but reveals nothing of the vessel's three-dimensional shape. MRI and CT are the only noninvasive imaging modalities capable of providing both a three-dimensional structure of the coronary arteries as well as cross-sectional views of the vessel lumen. They, however, are not without their own limitations.

The largest obstacle to obtaining high quality MRI or CT images of the coronary arteries is motion artifact. Motion artifacts occur when the object being imaged moves during image acquisition. These artifacts cause blurring in the final, reconstructed image. For cardiac imaging, this motion is generated by respiration and by the contraction and relaxation of the heart as it is beating. The small size of the coronary arteries only

amplifies the effect of respiratory and cardiac motion. In cases where a cross-sectional image is acquired over multiple heart beats, the artery lumen may be displaced a distance greater than its diameter and look like two vessels side by side. Respiratory motion has long been accommodated by imaging during a breath hold in CT and MRI or by the use of navigator echo gating in MRI[30]. Cardiac motion, however, cannot be stopped in a manner similar to holding your breath. Techniques have been developed in both CT and MRI to decrease the effect of cardiac motion. These include shortening the image acquisition time, ECG triggering, and retrospective reconstruction techniques using data from multiple heart beats to generate a single image.

Computed Tomography Coronary Angiography

Recent advances in CT technology now allow for improved image quality of coronary arteries for heart rates lower than 70 beats per minute[31-33]. Spiral CT scanners acquire image data over a continuous volume as the patient passes through the gantry while the X-ray source and detectors rotate at speeds as fast as 300msec per rotation. New scanners with 64 or more detector rows can image the entire heart during one breath hold with an in-plane resolution of 0.35mm and slice thickness of 0.40mm resulting in near isometric volume elements. Multi-sector image reconstruction techniques use projection data from up to four consecutive heart beats and have improved temporal resolution to 63msec during the cardiac cycle – fast enough to potentially acquire images without significant motion artifacts. With greater spatial resolution than MRI and image acquisition that is not averaged over many heartbeats, CTCA should be capable of providing more reliable geometric boundary conditions for CFD simulations.

Multi-sector Reconstruction

Multi-slice spiral CT scanners acquire continuous data in time and space. Once that raw data is acquired, it must be processed to represent an image from one window of time. This is done using retrospective ECG gating. ECG data is recorded simultaneously with the CT scan. In most clinical applications, images are then reconstructed using only the data acquired during a fixed amount of time after the R-wave. Other gating alternatives include data reconstruction at a defined fraction of the R-R interval or reconstruction at a specified amount of time prior to the next R-wave[34]. Single-sector reconstruction techniques generate images from data acquired during one cardiac cycle. Two-sector reconstruction uses data from two sequential heartbeats to form one slice of the eventual three-dimensional image[35, 36]. As shown in Figure 2.1, two-sector reconstruction can decrease the image acquisition window in the cardiac cycle by a factor of two compared to conventional one-sector reconstruction. This is made possible by the

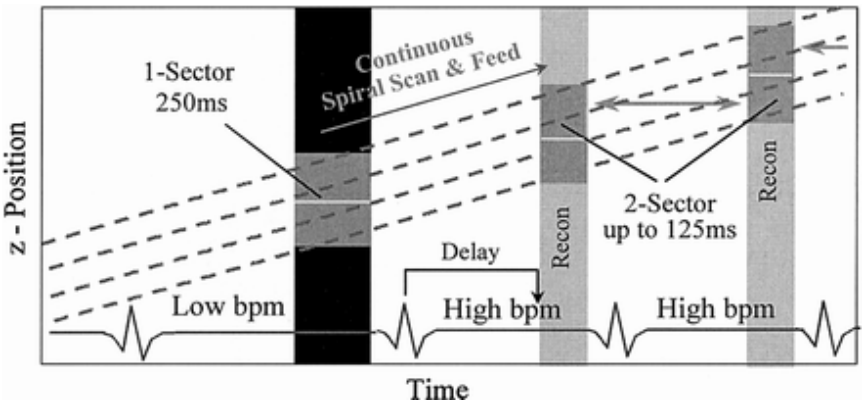

Figure 2.1 Retrospective gating techniques for 4-slice CT reconstruction (Kopp, 2001)

manipulation of the pitch or table speed such that one slice of the subject is scanned by multiple detectors in consecutive rotations of the gantry. Half of the image data is collected during each pass of the gantry and reconstructed to generate a whole image. A critical assumption made when using this method is that there is no net movement of the artery being imaged between the two data acquisition segments. While this technique increases temporal resolution, it introduces a small degree of data averaging and also increases the radiation exposure and dose to the patient.

Effect of Heart Rate on Temporal Resolution in Multi-sector Reconstruction

Prior to the advent of multisector reconstruction techniques, the temporal resolution of CT scans was solely dependent upon the rotation speed of the CT gantry. Since CT collects data as a projection, only an 180˚ sweep, referred to as a "half-scan", of the gantry is necessary to acquire a full two-dimensional image. The temporal resolution of the scan, in that case, would be half the time it takes for the gantry to rotate around the patient. Multisector reconstruction generates an image from data acquired during multiple heart beats, thereby decreasing the size of the data acquisition window in the cardiac cycle. It is important to note, however, that a full 180˚ of projection data is still required to reconstruct the image. Since the rotation of the CT gantry and the cardiac cycle are both periodic in nature, their synchronization comes into play when acquiring a half-scan over multiple heart beats at the same phase of the cardiac cycle. As described by Flohr and Ohnesorge, the effective temporal resolution becomes highly dependent upon the patient's heart rate[37].

In the optimal case for two-sector reconstruction, the CT scanner will reconstruct a 90˚ arc of data from one heartbeat and the complimentary 90˚ in the next heartbeat – resulting in an effective temporal resolution of one-fourth the gantry rotation time, t_{rot}. This scenario is illustrated in Figure 2.2. The sinusoidal curve juxtaposed above the ECG curve represents the location of the CT gantry as it rotates with a given period. Points A and B denote the gantry position at 60% of the cardiac cycle of two consecutive heart beats. The effective temporal resolution of this scan would be 102msec. If, however, the cardiac cycle and gantry rotation are perfectly synchronized and only a 90˚ projection was acquired with each heartbeat, the same 90˚ would be acquired each time. In that instance, the one-sector reconstruction temporal resolution of ½ t_{rot} can not be improved upon (Figure 2.3, effective temporal resolution equals 250msec).

Most frequently, there will be some amount of missing data if the data reconstruction window is limited to ¼ t_{rot}. In this scenario, the reconstruction window during one of the cardiac cycles must be extended to acquire a full dataset and the effective temporal resolution must be reported as the longer of the two acquisition windows (Figure 2.4, effective temporal resolution equals 160msec). This relationship between gantry rotation time and heart rate results in a "saw tooth" shaped temporal resolution curve that oscillates between ½ t_{rot} and ¼ t_{rot} (Figure 2.5). It should be noted that, with this relationship, a faster gantry rotation speed does not necessarily yield better temporal resolution for a given heart rate. For this reason, it is also conceivable that a faster heart rate will result in better temporal resolution. This scenario is examined in Chapter 4 of this dissertation.

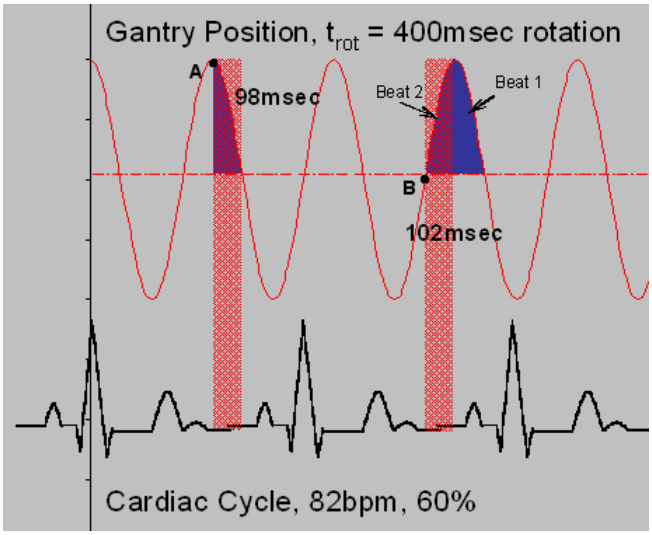

Figure 2.2 Optimal two-sector reconstruction temporal resolution

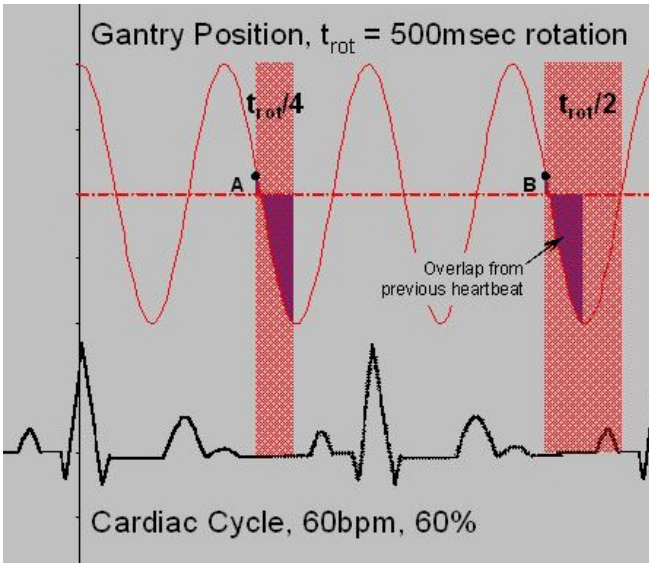

Figure 2.3 Worst two-sector reconstruction temporal resolution

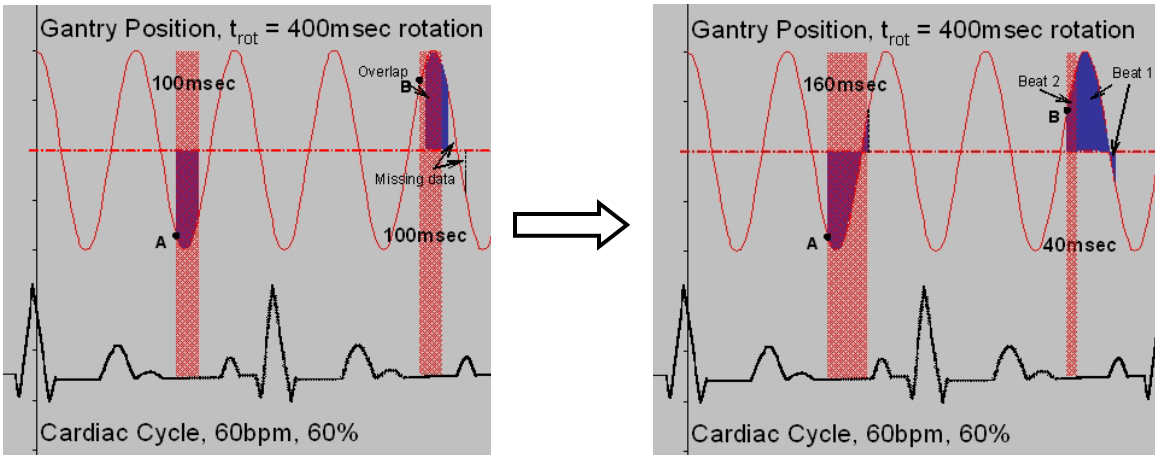

Figure 2.4 Intermediate two-sector reconstruction temporal resolution

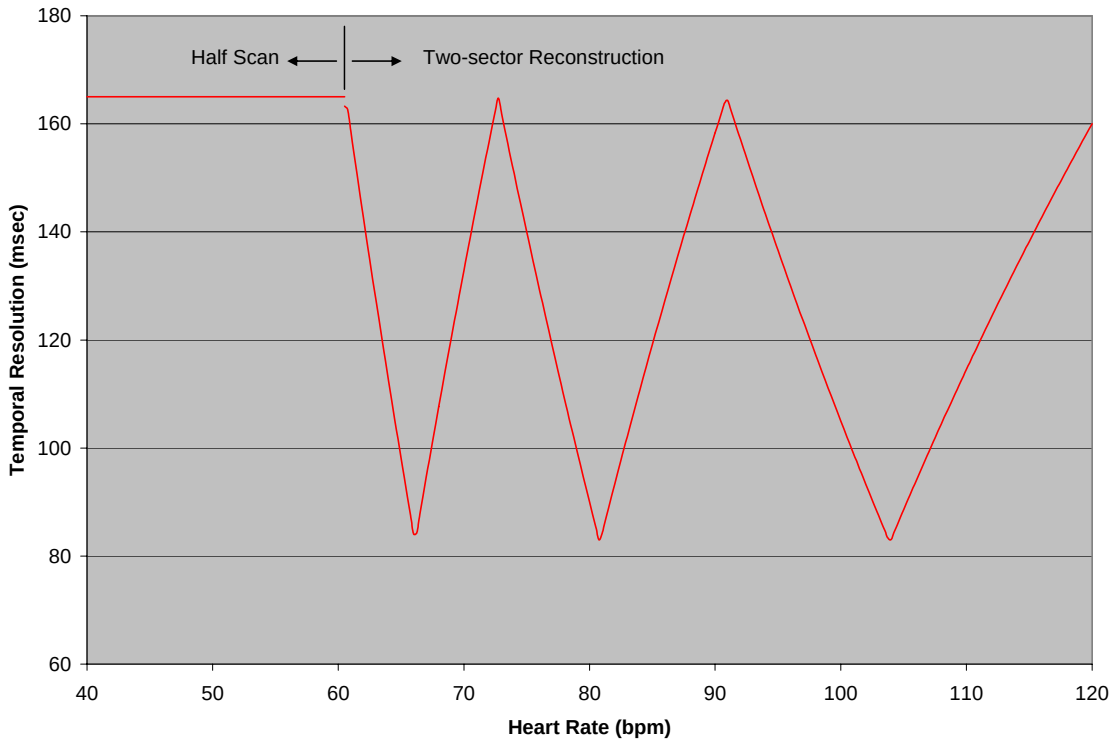

Figure 2.5 CT temporal resolution as function of heart rate for 330msec rotation

Magnetic Resonance Imaging

Magnetic resonance imaging (MRI) uses short radiofrequency pulses to knock protons out of alignment with a large magnetic field. Images are reconstructed using signal from the rotating transverse magnetization of those protons as they return, or relax, back to alignment with the main field. This signal is a vector quantity with both a magnitude (measure of how much the magnetization has relaxed) and a phase (how far ahead or behind the protons are rotating compared to a reference). In most imaging techniques, phase images are not reconstructed.

In phase contrast magnetic resonance imaging (PC-MRI), two additional velocity-encoding gradients are added that cause a known phase shift. These velocity-encoding gradients are opposed (one negative and one positive) such that the second pulse cancels the phase shift acquired in static tissue during the first pulse. However, protons that move during the time between the two pulses, such as contracting heart tissue or blood flowing through a vessel, acquire a phase shift directly proportional to the velocity at which those protons were moving. Since there are still uncontrolled contributors to the phase signals, the velocity-encoded image must be subtracted from a reference scan obtained without the additional gradient pulses. The resulting image is called a "phase velocity map" and shows static tissue grey (zero phase shift) and moving tissue either lighter or darker (positive or negative phase shift) depending on the direction and magnitude of the velocity[38, 39]. In the phase image shown in Figure 2.6 (left), bright flow going into the image plane can be seen in the ascending aorta (Ao) whereas, in the descending aorta (DescAo), dark flow is coming out of the image plane. PC-MRI can be

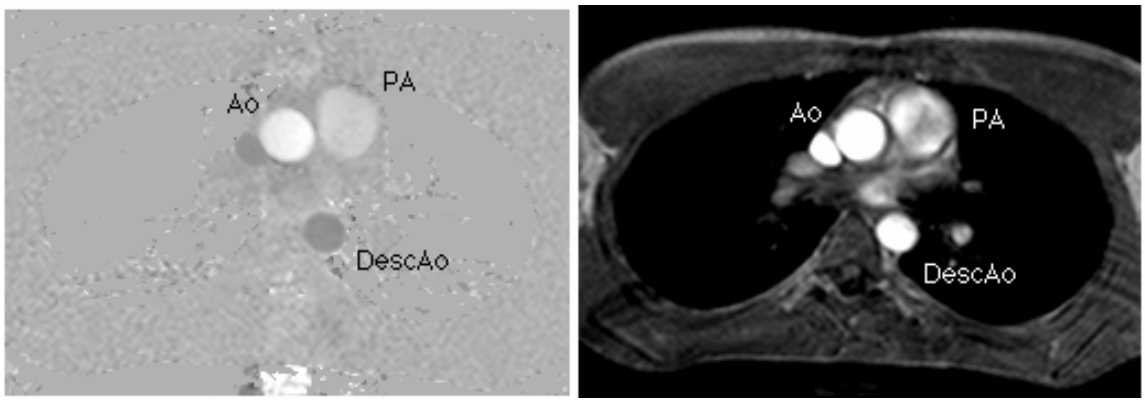

Figure 2.6 PC-MRI Image

conducted to acquire a static image and can also be acquired in cine mode – resulting in a series of velocity maps over a given time course, such as the cardiac cycle.

Both conventional imaging sequences and phase-contrast imaging techniques are used in clinical application and are employed in Chapter 5 of this dissertation. Their capabilities and limitations are discussed at greater length below.

Coronary Magnetic Resonance Angiography

Coronary magnetic resonance angiography (MRA) is a term used to collectively describe any imaging sequence designed to visualize the coronary arteries. Some coronary MRA sequences involve the intravenous injection of a contrast agent[40] while others utilize the magnetic or hemodynamic properties of the flowing blood to generate contrast from surrounding tissue[41]. While CT has been the more common imaging modality for visualization of the coronary vessels, coronary MRA has shown promise for the detection of coronary artery stenoses[42-45]. Two recent head-to-head comparison

studies concluded that MRA can identify significant coronary artery disease with equivalent or better diagnostic accuracy compared to 4 and 16-slice CT[46, 47].

As noted earlier, the two primary obstacles for coronary imaging are respiratory motion and cardiac motion. In one 2006 study, one-third of patients were unable to hold their breath suitably for high resolution cardiac MR imaging during a breath-hold [48]. Navigator echo gating is a technique that allows image acquisition during free breathing. A small excitation pulse is positioned over the diaphragm to monitor the patient's respiration – only allowing data acquisition during end-expiration when the border between the lung and liver is within an automatically determined acceptance window [49]. Figure 2.7 illustrates the positioning of the navigator echo and monitoring of the lung/liver border over time. The red dots indicate the position of the lung/liver border for each cardiac cycle. The width of the acceptance window (shown in blue) can be set by the operator. Image data is not acquired during cardiac cycles falling outside of the acceptance window. Use of navigator echo gating increases the total duration of the scan

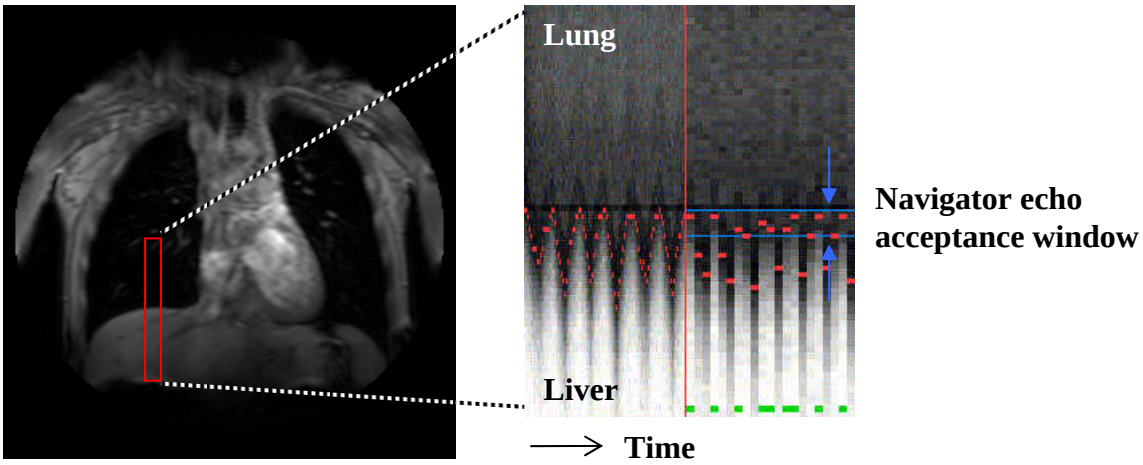

Figure 2.7 Illustration of navigator echo gating

but can allow choosing scan parameters to improve image quality or temporal resolution[50, 51].

Cardiac motion, however, can not be avoided and can only be minimized by the planning of faster imaging sequences and the timing of image acquisition to periods of the cardiac cycle during which the heart is moving more slowly. Typically, a transverse cine of the heart is obtained to view a segment of the right coronary artery (RCA) in cross-section. The frame-to-frame motion of the mid-RCA is followed and the phases with the least displacement between them are then chosen as the timing window during subsequent coronary MRA [52]. It has been shown that this patient-specific approach yields better quality images than predefined trigger delays based on heart rate dependent empirical formulas[53].

Phase Contrast Magnetic Resonance Imaging

Since most of the tissues in the relaxed human body either do not experience motion or move very slowly, phase velocity mapping is primarily a tool employed to observe fluid flow – most commonly blood flow. Flow curves can be obtained using phase-contrast cines over the course of the cardiac cycle. This technique has been validated with good agreement in 1.5T scanners compared to Doppler ultrasound and oximetry when measuring flow in vessel phantoms [54] and large vessels such as the aorta and superior and inferior vena cava[39, 55-60]. Few studies, however, have used PC-MRI to measure coronary flow because of the cardiac and respiratory motion of the vessels and their small diameter. Accuracy of PC-MRI can be severely limited in small vessels due to undersampling of velocity measurements across the vessel and by partial

volume effects at the vessel wall caused by insufficient spatial resolution [60, 61]. In 1999, Nagel, *et al.* showed significant underestimation of maximal flow velocity determined by MRI compared to ultrasound[51]. The underestimation was not as profound in navigator-echo gated scans with shorter acquisition times and hence more phases over the cardiac cycle compared to a breath-hold technique. Subsequent *in-vivo* studies of the coronary arteries with improved temporal resolution have decreased the disagreement with ultrasound to less than 10%[50, 62]. In addition to it's use for measuring blood flow, navigator echo-gated PC-MRI has recently been employed to measure velocity of the myocardium during cardiac contraction and relaxation with excellent accuracy compared to known motion in a phantom study and compared to Doppler echocardiography in human subjects[63].

Improvements in spatial resolution and signal-to-noise ratio (SNR) for cardiac imaging applications have been achieved by using higher field strength 3.0T scanners [64, 65]. Validation studies of 3.0T PC-MRI in larger diameter vessels have recently been performed showing good precision and accuracy at high flow rates; but the accuracy of navigator echo gated 3.0T PC-MRI for low flow rates in small diameter vessels as is seen in coronary artery flow has to this point not been evaluated [66].

Determination of *In Vivo* Wall Shear Stress

For Newtonian fluid flow, wall shear stress is defined by the equation:

$$WSS, \tau = \eta * \nabla \bullet \vec{v} \qquad [2.1]$$

where η is the viscosity of the fluid (in this case, blood) and $\nabla \bullet \vec{v}$ is the dot product of the gradient vector and velocity vector, also known as the shear rate, of the fluid at the

wall. In the simplified case of axially dominated flow through a cylinder, Equation [2.1] can be rewritten as:

$$WSS, \tau = \eta * \frac{\partial v}{\partial r} \qquad [2.2]$$

in which $\frac{\partial v}{\partial r}$ is the change of velocity along the radial direction of the vessel. This equation can be further simplified assuming the Poiseuille flow model with a parabolic velocity profile as:

$$WSS, \tau = \frac{32\eta Q}{\pi D^3} \qquad [2.3]$$

where Q is the volumetric flow rate and D is the diameter of the vessel. This simplification is used in all studies of coronary wall shear stress that do not employ computational fluid dynamics but ignores local variances in the coronary geometry in which cross-sections are not perfectly circular, flow in a direction that is not in the axial direction, and assumes a steady, parabolic velocity profile. From these expressions, it can be seen that either the volumetric flow rate or velocity profile must be known to calculate WSS – specifically the velocity profile at the vessel wall.

Using the Poiseuille flow assumption and Equation 2.3, Doriot, *et al.* calculated average coronary WSS at the inflow and outflows of coronary bifurcations[67]. Vessel diameters and cross-sectional areas were measured from bi-plane X-ray angiography while velocity measurements were acquired by an intravascular Doppler flow-wire. By this approach, however, half of their patient data was discarded because conservation of mass (total inflow being equal to total outflow) was not sufficiently satisfied by their measurements. The study assumed circular vessel cross-sections and could not

investigate time varying WSS. In addition to the limitations described above, studies using X-ray angiography or intravascular ultrasound require the invasive and potentially dangerous use of coronary catherization. MRI is the only established technique to measure coronary velocity in a non-invasive manner.

Wall Shear Stress Calculation by MRI

PC-MRI alone has been used to determine WSS but has problems with partial volume effects. In this instance, the pixels at the blood-lumen boundary invariably contain velocity signal from both the moving blood and stationary vessel wall. Also, the poor spatial resolution of MRI in relation to the diameter of the coronary arteries – only 2-5 voxels of data can be acquired across the vessel diameter – makes it difficult to obtain an accurate velocity profile. A study by Tang, *et al.* determined that as many as 16 pixels must be acquired across the diameter of a vessel to calculate an accurate velocity profile[68]. It has been shown that using MRI alone to calculate WSS frequently underestimates true blood flow velocity and can result in large errors (>15%) in WSS calculation[69-73]. In general, direct extrapolation of WSS from *in-vivo* MRI has been unsuccessful because of inadequate spatial resolution to develop a sufficient velocity profile near the vessel wall.

Wall Shear Stress Calculation by Computational Fluid Dynamics

CFD with MRI

Another proposed solution has been to combine MRI geometry and velocity scans with computational fluid dynamics (CFD). CFD uses a computer mesh of a control volume (i.e. a blood vessel) and calculates the spatial and temporal fluid velocity profiles through the entire volume given boundary condition flow profiles at the entrance and exit of the volume. This technique has been used to examine WSS in larger vessels such as the aorta and carotid arteries[74, 75]. Several studies have examined the relative importance of either the geometric or flow boundary conditions in calculations of WSS. Changes in flow of 10% or less have not demonstrated discernable effects on WSS magnitude or distribution in CFD simulations of blood flow in the carotid artery bifurcation [76-80].

While more robust than earlier methods, a major shortcoming of using MRI and CFD to determine WSS is that the MRI-determined geometries are not sufficiently accurate or repeatable to specify geometric boundary conditions for the CFD simulation. In two independent studies, time-averaged WSS calculations from repeated MRI scans of the carotid bifurcation varied by 37% and 40%[76, 79]. While the in-plane resolution of MRI is very good, the through-plane resolution (or slice thickness) is frequently an order of magnitude larger. This can create discrepancies in three-dimensional model geometries if the orientation of the image slices is not perfectly reproduced.

CFD with Bi-plane Angiography and Intravascular Ultrasound

An improvement upon the spatial resolution weakness of MRI can be found in CFD models that determine vessel geometry using bi-plane X-ray angiography and intravascular ultrasound (IVUS). Although it requires invasive catheterization, this technique acquires high resolution, two-dimensional vessel cross-sections by intravascular ultrasound and positions those cross-sections along a three-dimensional vessel centerline determined by bi-plane angiography. Where the majority of these studies are lacking is in their choice of velocity boundary conditions. Krams, *et al.* used biplane angiography and intravascular ultrasound to generate a mesh for CFD analysis of WSS but did not have patient-specific flow data and instead made calculations for a series of uniform, constant flow velocities[29]. Another study calculated a steady flow rate for CFD simulation by timed filling of a coronary artery section with radio-opaque contrast during dye injection[81]. While more patient-specific than the previous study, neither of these steady flow simulations can be used to analyze dynamic changes of WSS during the cardiac cycle.

Unsteady flow CFD simulations allow for the calculation of parameters such as oscillatory WSS index and WSS angle deviation. Several studies have paired bi-plane angiography and IVUS vessel models with unsteady velocity curves; but have used standardized flow curves reported in previous literature rather than patient-specific velocity measurements[82-84].

CFD with CT and MRI

Thus far, there have been no published attempts to develop a CFD model of coronary artery blood flow combining the strengths CT and MRI. Both imaging modalities are noninvasive procedures. PC-MRI has been well established as a technique to measure blood flow velocity in larger vessels. CT coronary angiography offers isometric three-dimensional spatial resolution and is already used to generate three-dimensional visualizations for clinical assessment of the coronary arteries. Chapter 6 of this dissertation establishes a technique in which CT is used to generate a geometric model and 3.0T PC-MRI is used to acquire patient-specific coronary artery blood flow velocity measurements for CFD analysis.

CHAPTER 3

CORONARY ARTERY MOTION *

Introduction

The constant motion of the human heart has been the predominant motivator for innovation in CT technology over the past fifteen years. Were the heart in some way able to circulate blood without contraction and relaxation, the only benefit of decreased CT gantry rotation times would be a slight reduction in radiation dose. In fact, other technological advancements such as multi-detector scanners, multi-sector reconstruction techniques, and dual source scanners *increase* radiation dose to affect improvements in image quality for cardiac scans. These recent improvements to CT technology are all designed to improve temporal resolution and minimize blurring and other artifacts caused by movement of the heart during image acquisition. To that end, it is advantageous for images to be acquired (or reconstructed) during periods of the cardiac cycle in which there is the least amount of motion.

Current clinical practice for cardiac CT is to acquire data over the entire cardiac cycle and then reconstruct images at 10% increments of the entire cardiac cycle – letting the physician who reads the study decide which image or images are best for diagnostic purposes. In cases where only one or two phases of the cardiac cycle are used for

* A version of the research presented in this chapter has been published in the *Journal of Cardiovascular Magnetic Resonance*. [1]

evaluation, there is excessive exposure of radiation to the patient as well as unneeded image data that must be retained in the institution's archives. Recent development of adaptive tube current modulation its inclusion in the current generation of CT scanners allow the current in the x-ray tube to be decreased or increased in real-time according to the patient's ECG – potentially reducing dose by 40-60%. But what periods of the cardiac cycle are better times for image acquisition? Can generalizations be made across patient populations? Or even across different anatomical regions of the heart?

This chapter serves to answer these questions by analyzing the motion of three main coronary arteries in a series of patients: the left anterior descending (LAD), left circumflex (LCX), and right (RCA) coronary arteries. These vessels were chosen for study for several reasons: they are primary objects of interest in cardiac imaging studies; the LAD, LCX, and RCA spread over wide regions of the heart's external surface; and branch points of the coronary arteries can be easily identified and tracked by angiography studies. This initial study will provide both an analysis of "rest periods" during the cardiac cycle that would be preferable for image acquisition as well as detailed courses of coronary motion that will be used in Chapter 4 to provide realistic motion for a coronary phantom in an evaluation of CT imaging.

Methods

Digitally archived, ECG-gated, bi-plane, angiography films of 15 patients with coronary artery disease were reviewed. The patients were all males with average age of 55 years (range: 45-68). The average heart rate of patients reviewed for this study was 66 beats per minute (range: 49-82). Each patient had undergone routine diagnostic cardiac

catheterization with bi-plane, cine angiography and simultaneous ECG recording. Angiography was performed during breath-hold to minimize the effects of respiratory motion. Digital images were recorded at 30 frames per second and stored on optical disk for future review.

Landmarks (usually branch vessels) along the proximal, middle, and distal regions of the LAD, LCX, and RCA that could be seen on both orthogonal views were identified and tracked over the cardiac cycle. An example of two angiography views for an RCA is shown in Figure 3.1 with markers at the three regional landmarks. Frame-to-frame displacement was determined for each landmark over the cardiac cycle. Displacement was measured in three perpendicular directions (two on one angiographic view and one on the other orthogonal view), hence three-dimensional motion was evaluated.

Spatial coordinates of the landmarks were transformed to take into account the capturing angles of the two cameras used to acquire the angiography images so position

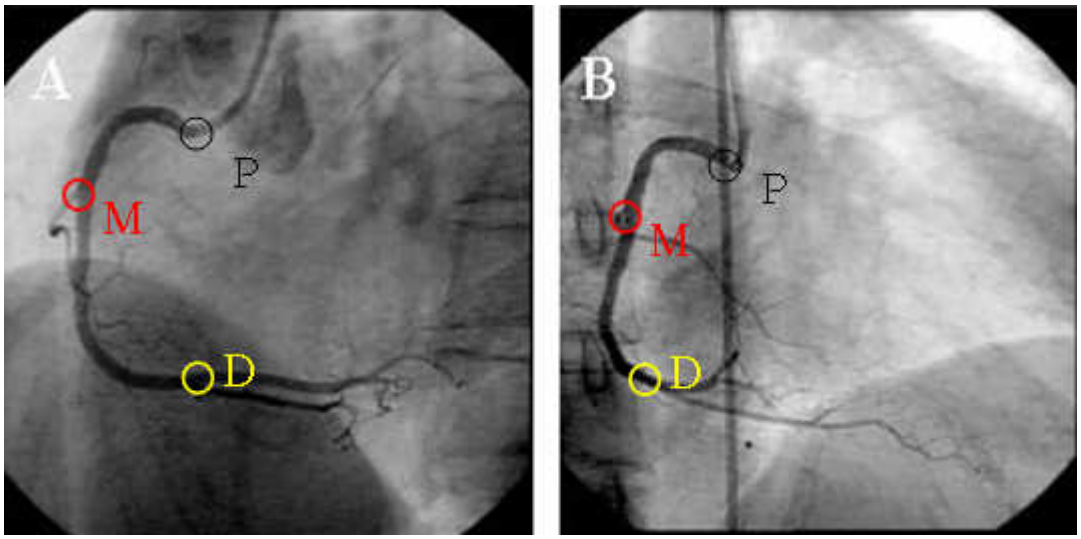

Figure 3.1 Bi-plane angiography frame of RCA with regional markers

and displacement data for the landmarks existed in a standard, orthogonal axis coordinate system relative to the human body (left-right, anterior-posterior, and cranial-caudal). In order to pool results from patients with different heart rates, the data was interpolated to 5% intervals of the cardiac cycle. Curves of displacement versus time in the cardiac cycle were created, and maximum and average displacements were determined for each vessel segment. Incremental displacement was defined as the distance traveled over 5% of the cardiac cycle. Similar in nature to frame-to-frame displacement, values of incremental displacement are proportional to velocity. In the accompanying graphs of incremental displacement, regions where incremental displacement is low indicate periods of the cardiac cycle of decreased coronary motion.

A period of low motion was defined as any period in which the three-dimensional displacement $[(\Delta x^2 + \Delta y^2 + \Delta z^2)^{1/2}]$ from one cine frame to the next was less than a set threshold value. Displacement was analyzed at a threshold value of 1.0mm per frame, corresponding to a speed of less than 30 mm/sec. The duration of low motion periods for each artery and their location in the cardiac cycle were identified and recorded for comparison. Location and duration of the periods were defined from the original cine images acquired at 30 frames per second – without interpolation to 5% intervals of the cardiac cycle.

Results

Since the primary outcomes of this study are three-dimensional trajectories of the three coronary arteries, a large portion of this Results section will be in the form of graphs or tables that illustrate and summarize that motion. Graphs of coronary artery

motion are presented as averages over the patient population and have been interpolated to percentages of the patients' respective cardiac cycle. In these graphs, the cardiac cycle is displayed on the x-axis where 0% - 100% is represents the period between two R-waves. Plotted on the y-axis are distances of excursion during coronary motion defined in one of two ways: either total displacement from where a regional marker was at 0% of the cardiac cycle or incremental displacement for how much a marker has been displaced over the previous 5% of the cardiac cycle. Total displacement plots the trajectory of the artery over time whereas incremental displacement is proportional to the velocity of the artery.

Detailed Coronary Artery Motion

Figure 3.2 displays the average three-dimensional motion trajectories of the three coronary arteries in our patient population. The largest maximum total coronary displacement was 16.1mm observed in the mid segment of the RCA (maximum mean displacement of the patients). Maximum displacement of the other arteries was 9.7mm in the distal LCX, and 6.1mm in the mid LAD. A comparison of the arteries' total and incremental displacements can be seen in Figure 3.3. This shows that on average, the RCA experiences a greater range of motion as well as greater speeds of motion than either the LAD or LCX. Maximum RCA displacement was up to 2.5 and 3.2 times greater than the LAD and LCX, respectively, and average RCA displacement was 2.1 and 2.2 times greater than the LAD and LCX displacement, respectively.

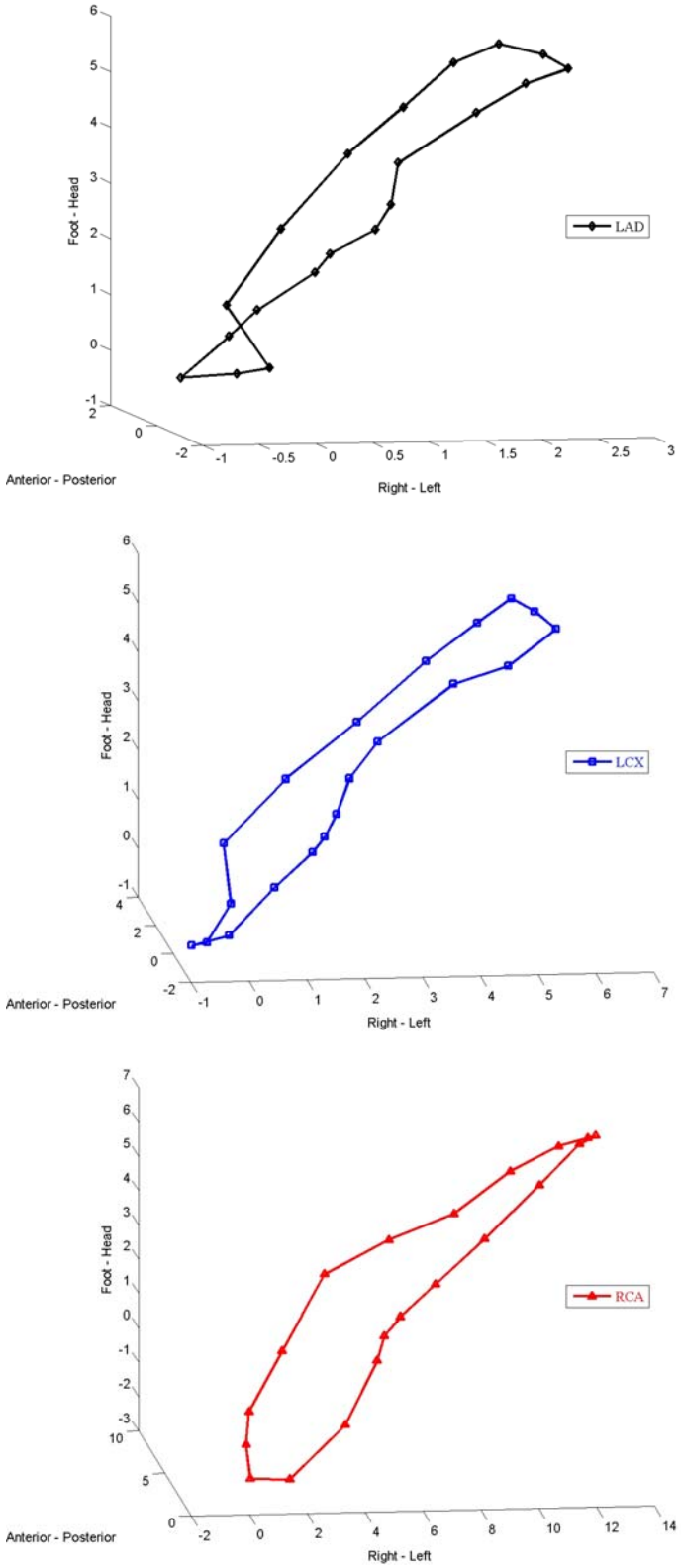

Figure 3.2 Three-dimensional trajectories of mid LAD, LCX, and RCA

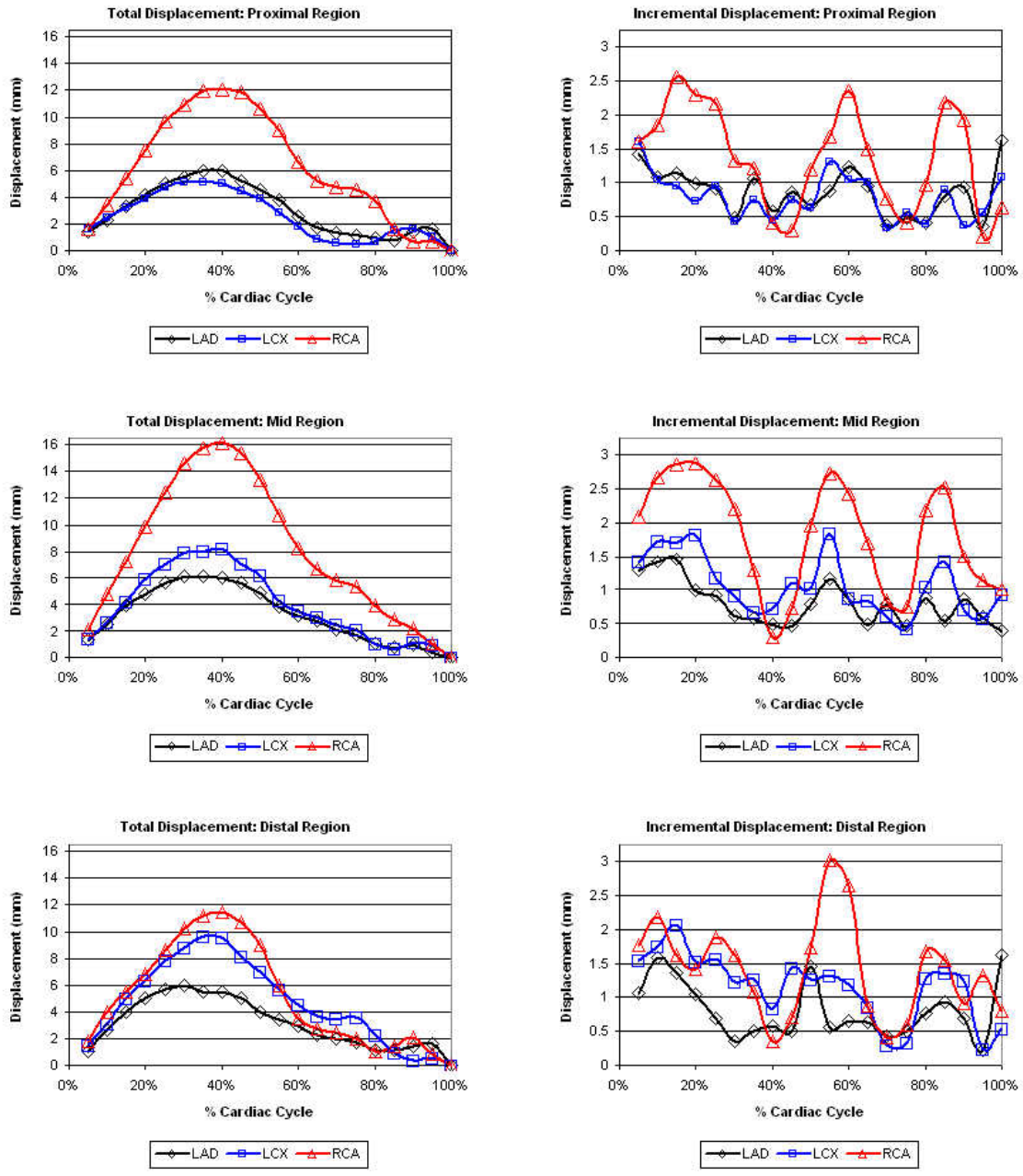

Figure 3.3 Total and incremental displacement of the coronary arteries

Table 3.1 Orthogonal Components of Coronary Artery Motion

	Right – Left	Anterior – Posterior	Cranial – Caudal
LAD	26%	15%	59%
LCX	33%	19%	48%
RCA	48%	22%	31%

Table 3.1 summarizes the contribution of coronary motion components in each of the three orthogonal directions. The motion of the LAD and LCX (averaged over the proximal, mid, and distal segments) was predominantly in the cranial-caudal (CC) direction compared to the right-left (RL) direction or the anterior-posterior (AP) direction. On average, more than half the motion of the LAD was in the CC direction (59±11%) with some movement in the RL direction (26±7%) and little motion (15±5%) in the AP direction. The LCX showed similar characteristics with predominant motion in the CC direction (48±10%) compared to the RL direction (33±7%) and the AP direction (19±5%). The majority of motion in the RCA, however, was observed to be in the RL direction (48±7%) with relative motion in the AP and CC directions of 22±5% and 31±9%, respectively. While the magnitude of motion in each direction varied, the timing of rest periods was consistent in each direction.

Rest Periods

All three coronary arteries had two periods of relatively low motion, when frame-to-frame displacement was <1mm. These periods are illustrated in Figure 3.4 broken down by artery and by segment. The first period occurred at 34±8% of the cardiac cycle after completion of ventricular systole. The average length of the first period was 118msec (range 0-231msec). The temporal location of the first rest period varied greatly among the different regions of the three coronary arteries. In three subjects, there was no systolic period of low motion. The second period occurred at 72±5% of the cardiac cycle, after relaxation of the ventricles. This second period was generally longer than the first period, lasting an average of 187msec (range 66-330msec). The timing of the second period of low motion was less varied in the segments of the different arteries. Frame-to-frame displacement increased again in late diastole during atrial systole. The length of each rest period was plotted against heart rate and an inverse relationship was noted – as the heart rate increased, the duration of rest shortened.

Data was also analyzed for time periods during which frame-to-frame displacement was < 0.5mm. Under this restriction, the number of rest periods decreased by 64% and the average duration of the remaining rest periods also decreased 62msec. 29 out of 45 artery segments studied had no systolic rest period. 19 out of 45 artery segments studied had no rest period in the entire cardiac cycle.

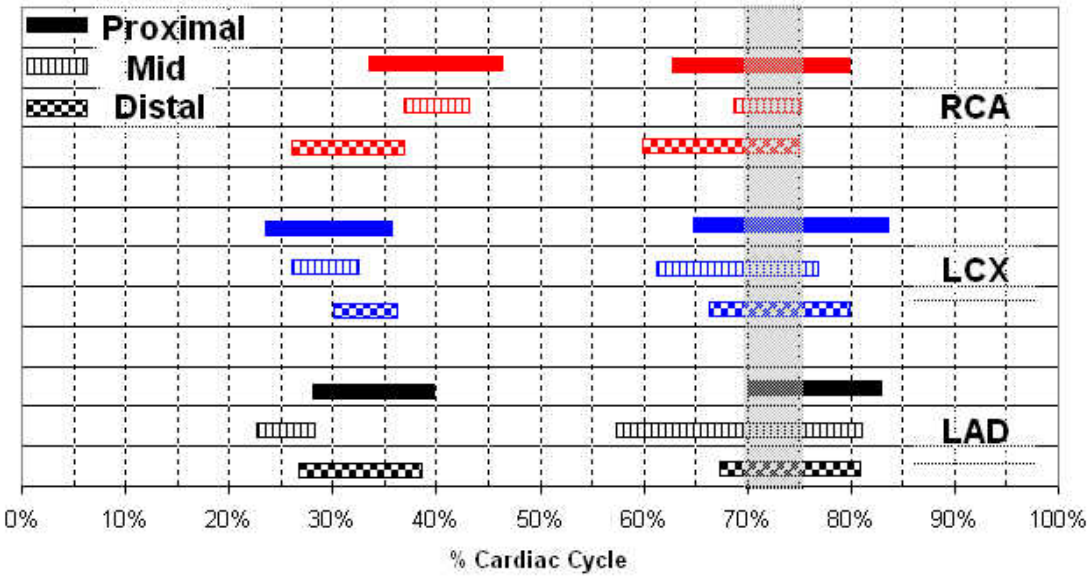

Figure 3.4 Average duration and location of coronary artery rest periods

Discussion

This study quantitatively described the motion of the coronary arteries in three dimensions. The overall displacement of the RCA was 2.1±0.7 times that of the LAD and 2.1±1.5 times that of the LCX. Two periods in the cardiac cycle were seen where all three coronary arteries have relatively little coronary motion (<1mm/frame or 30mm/sec). The first of these periods was located at the completion of ventricular systole (34±8% of the cardiac cycle) with duration of 118±78msec. The temporal location of this rest period, however, varied significantly among the three coronary arteries. No acquisition window was able to capture the rest period of all segments of all arteries at the same time. A second period of low motion was seen at mid-diastole (72±5% of the cardiac cycle) with duration of 187±119msec. This period was more consistent throughout the three

coronary arteries and allowed for a window of 6% of the cardiac cycle during which, on average, all segments of the LAD, LCX, and RCA are “at rest”.

It is important to note that these results represent averages across the collection of artery segments studied. There was significant variation between subjects. For example, a 100msec acquisition window at 72% of the cardiac cycle would miss the period of low motion in 9 of 45 artery segments studied (3 segments had no diastolic rest period). Also in 9 of the artery segments, the rest period was only 66msec. Any acquisition window or reconstruction window >66msec will create some degree of blurring due to motion in these instances. When the allowed motion threshold was decreased to <0.5mm/frame (15mm/sec), the occurrence and duration of rest periods decreased substantially and did not allow for a single acquisition window to cover each artery segment.

The amount of motion varied to some extent along the length of the coronary arteries. In the right coronary artery, the mid segment of the vessel experienced 1.6±0.4 times as much motion as that of the proximal region of the vessel. The distal segment of the LCX experienced 1.6±0.8 times the motion as that of the proximal LCX. No significant variation in displacement was seen along the length of the LAD. Despite differences in amount of movement, the proximal, middle, and distal vessels of all three coronaries still show the same temporal location of relative quiescence at end systole and in mid-diastole. Motion along anterior-posterior, right-left, and cranial-caudal axes also showed similar timing of rest periods. The majority of motion observed in the LAD and LCX occurred in the CC direction (59±11% and 48±10%, respectively) while 48±7% of the RCA motion occurred in the RL direction.

In the vast majority of patient studies, the least motion and longest rest periods were observed in the proximal region of the three coronary arteries. This is arguably the most important region to image. Clinical studies have found that the largest percentage of stenotic lesions in the coronary arterial tree occur in the proximal regions of the arteries – most prevalently in the proximal LAD[85, 86]. In addition, the larger amount of motion in the distal vessels as well as the smaller size of these vessels make those segments more difficult to image.

Conclusion

The goal of this chapter was to characterize the three-dimensional motion of the RCA, LAD, and LCX coronary arteries. Two primary outcomes were attained from the data. First, a set of detailed, time-resolved trajectories of the coronary arteries that will define the motion of an imaging phantom in Chapter 4 to evaluate multi-detector CT. Second, a better understanding of rest periods during coronary motion that can be applied in a clinical setting. Minimizing the amount of cardiac motion during image acquisition is critical in MRI and CT imaging. This work can be seen as assistance in the planning of current imaging protocols while at the same time pointing out that the current technology may still be lacking in temporal resolution for optimal "freezing" of cardiac motion. The next chapter details experiments evaluating the relationship between temporal resolution and image quality in today's state-of-the-art CT scanners.

CHAPTER 4

DETERMINATION OF CORONARY GEOMETRY BY MULTI-DETECTOR CT

Introduction

As was mentioned in the introduction to this dissertation in Chapters 1 and 2, CT has several advantages over MRI for the determination of detailed coronary geometry. These advantages include superior spatial resolution, better vessel contrast, and shorter image acquisition time with less data averaging. Over the past decade, CT technology for both image acquisition and reconstruction has improved rapidly – so quickly, in fact, that clinical studies evaluating the usefulness of these advancements struggle to keep pace. As studies of eight-detector scanners were being published, 16-detector scanners were being introduced. As 16-detector studies came out, new 32 and 64-detector scanners became commercially available. Studies of these sorts most frequently were designed to qualitatively score image quality of coronary examinations and also to quantitatively compare stenosis severity determined by CTCA with the conventional gold standard of x-ray angiography. Stenosis severity measurements typically lump stenosis measurements into categories of >50%, 50-75%, 75-90% and 90% to total occlusion. As new scanners were introduced, markers of performance such as sensitivity, specificity, positive predictive value, negative predictive value, and percent of coronary artery segments excluded from assessment have tended to improve [87]. This is all well and good for the clinical setting. Lesions of 50% stenosis or less are usually ignored, mild stenoses may

be monitored and medicated but are not typically cause for invasive intervention, and severe stenoses more often result in immediate angioplasty, stenting, or bypass.

For fluid dynamic analysis, however, a more detailed geometric quantification is required. The standard patient-enrolled studies are ill-suited for this type of analysis for several reasons. Primarily, it is impossible to know the true geometry of a patient's coronary artery for comparison with measurements by CT. Physiologic parameters such as the vessel geometry and the heart rate are also highly variable among the patient population. Follow up studies to assess repeatability would be problematic due to the radiation dose that would be imparted to the patient. For all of these reasons, a study using a coronary vessel phantom with known geometry is desirable to quantitatively assess the accuracy of anatomic measurements by new CT scanners.

The overall goal of this chapter is to evaluate the accuracy of measurements taken from images of a coronary artery phantom acquired by a 64-detector CT scanner. These findings will validate the use of CT-acquired geometries for calculations of coronary WSS by commercial CFD software.

Methods

Experimental setup for the work detailed in this chapter involved several independent steps. First, a series of vessel phantoms were developed to model stenotic coronary arteries with varying geometries. These phantoms needed to have known geometries for comparison with CT measurements while also being compliant enough to mimic *in vivo* coronary artery curvature. Second, a method of imposing three-dimensional motion to the vessel phantoms was developed to simulate the cyclical

motion of the heart as described in the previous chapter. This technique needed to be repeatable with high accuracy yet flexible to allow simulation of multiple heart rates. Finally, there must be a consistent method of analyzing the resulting CT images.

Phantom Construction

A mold was designed with the simplified geometry of a stenosed coronary artery to create a CT phantom. The mold consisted of four parts – two outer pieces to form the vessel wall and two inner pieces to create the vessel lumen. The outer vessel wall measured 8cm long with a diameter of 8mm. The inner mold consisted of a brass rod with a diameter of 4mm. With help from the Emory University machine shop, the rod was mounted on a lathe and narrowed at its midpoint to form an "inverted stenosis" with diameter of 2.3mm. This process was repeated to create two additional molds: one with vessel diameter of 4mm and stenosis of 1.8mm and the second with vessel diameter of 2mm with stenosis of 1.1mm. The two 4mm diameter phantoms are representative of a proximal vessel with stenoses of 68% and 79%. The smaller, 2mm diameter phantom is representative of a 71% stenosis in the distal region of a coronary artery. The rods were then cut in half at their midpoint and a pin was inserted into the two ends so that they could be pulled apart and reattached easily. The inner vessel molds were fitted with two cylindrical spacers to elevate the mold to the vertical center of the outer chamber. For illustration, see Figure 4.1. A two-part silicone elastomer (Sylgard 184, Dow Chemical) was then cast around the solid model. Sylgard 184 was selected based on its tissue-mimicking attenuation and compliance. Once the silicone has cured, the vessel could be separated from the brass mold. Standard tube fittings were then attached at both ends of

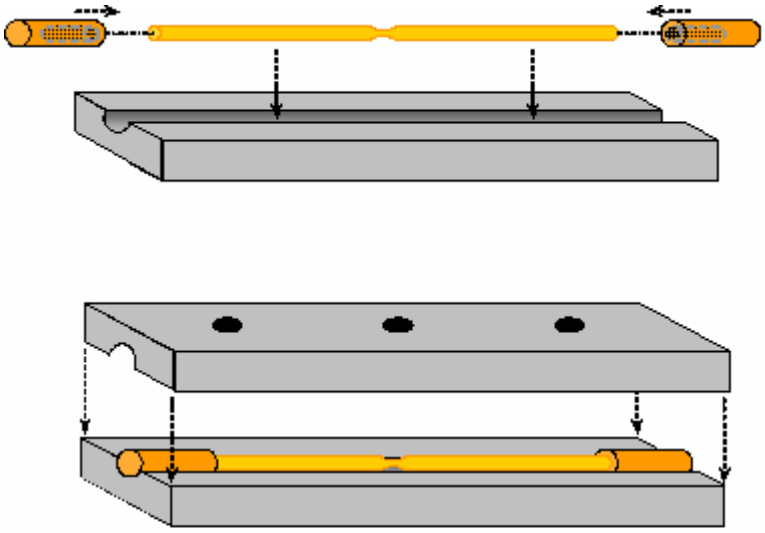

Figure 4.1 Schematic of phantom vessel mold

the vessel to allow for the injection of a contrast agent for CT studies. The resulting vessel phantom is transparent and compliant enough to be wrapped around a curved surface. The three phantom vessels were affixed to the exterior of a water bottle to simulate *in vivo* curvature of the coronary arteries. The water bottle was glued to a mounting plate that could be attached to the face of a motion stage used to generate three-dimensional motion during the imaging session.

Phantom Motion

Physiologic, three-dimensional motion was imposed on the phantom model by a three-axis motion stage (Cross Automation, Atlanta, GA). The motion stage is pictured in Figure 4.2. Motion is generated by three orthogonally mounted linear motors (Parker Hannafin Corp, Atlanta, GA) and controlled by a single computer and servo controller

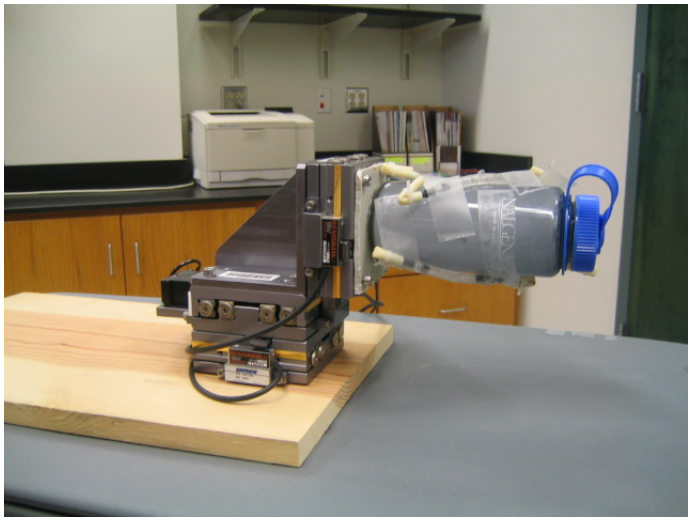

Figure 4.2 CT motion stage with vessel phantoms

(Galil Motion Control, Rocklin, CA). Vessel motion parameters including position, velocity, and time were defined as described in the results section of Chapter 3. As generating independent motion for each segment of the vessel model is physically infeasible with a rigid body phantom, the trajectory of the proximal LAD was used. The proximal LAD has been shown to be the most prominent location for coronary atherosclerosis, especially near its bifurcation with the circumflex artery[15, 17]. Program code was written to define this step-by-step motion over the course of a simulated cardiac cycle. This code was designed to easily facilitate changes in velocity in order to either increase or decrease the simulated heart rate while maintaining the same trajectory. Motion parameters were adjusted to simulate a range of heart rates to represent the variance seen clinically in the patient population as well as a range of effective temporal resolution (Table 4.1) – as described in Chapter 2: Multi-sector Reconstruction. The same motion trajectory was maintained for all experiments. Only the velocity of motion was altered to change the simulated heart rate. In addition to

Table 4.1 Heart Rate and Temporal Resolution for CT Motion Studies

Heart Rate	Static	56 bpm	61 bpm	68 bpm	85 bpm
Temporal Resolution	N/A	84 msec	159 msec	108 msec	119 msec
T. Res. As % of Cardiac Cycle	N/A	8%	16%	12%	17%

generating the programmed motion, the servo controller also outputs a 5V pulse at the start of each motion cycle. This pulse was passed through a converter box that was in turn connected to the CT scanner's ECG monitor to serve as a trigger for retrospective cardiac gating.

CT Scan Protocol

A clinical CT scanner (SOMATOM Sensation 64, Siemens Medical Solutions, Forchheim, Germany) was used to obtain images of the vessel phantom. The vessel phantom was filled with CT contrast agent (Visipaque, Amersham Health, Inc) diluted with water at a concentration of 30µg iodine/mL to achieve an attenuation coefficient typical of vessel contrast seen in *in vivo* CTCA. Motion conditions previously described were imposed on the model. Data was acquired continuously over the duration of the scan and images were reconstructed using a two-sector reconstruction protocol. This scan protocol has been developed by the manufacturer and is commonly used in the clinic for CTCA of human subjects. Standard x-ray settings of 120keV voltage and 80mA tube current were used. Images were reconstructed at the 70% interval of the simulated cardiac cycle. This is the time period during which the phantom experiences the least amount of motion along its programmed trajectory. All three vessel phantoms could be

mounted on the motion stage and imaged at the same time. Five scans were acquired at the simulated heart rates outlined in Table 4.1.

Image Analysis

Image analysis was performed by two cardiac radiologists experienced in the reading of CTCA cases. All analysis was performed on dedicated workstations in the Emory Clinic imaging lab. These workstations are equipped with software for cardiac CT image analysis and 3D volume rendering (CardIQ, GE Healthcare). The radiologists were blind to the vessels' dimensions as well as the simulated heart rate of each image. Following their standard protocol for human CTCA case review, the stacks of axial images were first reviewed and then a multiplanar reconstruction (MPR) of each vessel was generated to assess stenosis severity. Manual measurements of the vessels were taken on both sides of the stenotic region and at the narrowest point of the stenosis. Example images of measurements taken from four MPRs are shown in Figure 4.3. In addition to this quantitative assessment, the readers were also asked to score the overall image quality of each vessel on a scale from 1 to 4 as detailed in Table 4.2 with 4 being

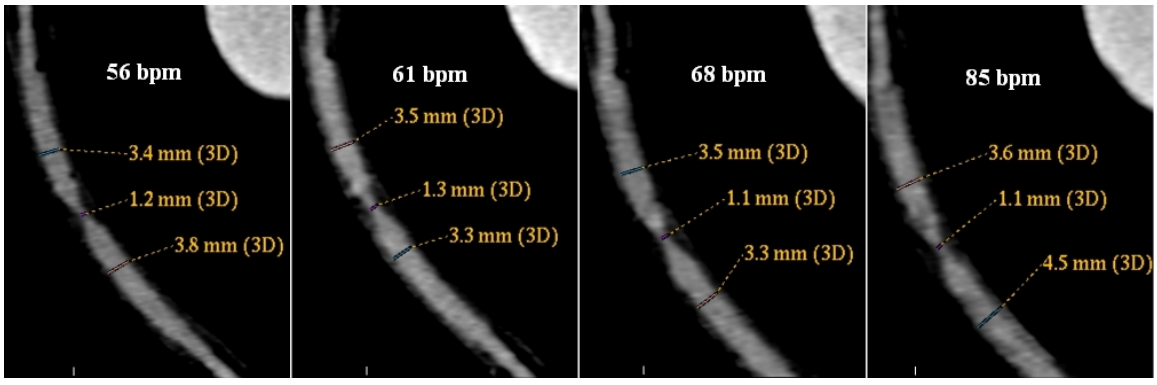

Figure 4.3 Multiplanar reconstructions of phantoms with diameter measurements

Table 4.2 Image Scoring Guidelines for CT Studies

4	Excellent. No motion artifacts, very sharply delineated contours.
3	Good. Minimal motion artifacts, sharply delineated contours.
2	Moderate. Some motion artifacts, slight-contour blurring, but still assessable.
1	Poor. Pronounced motion artifact and blurring, not readable.

superior image quality. The phantom studies were read once, then re-randomized, and assessed again several days later to double the number of measurements.

Vessel Sharpness

Cross-sectional images of the vessel phantoms were analyzed to obtain a measure of vessel sharpness, or how well the image delineates the boundary between the contrast-enhanced vessel lumen and the vessel wall – or the surrounding myocardium in the *in vivo* situation. Using image processing software (Matlab, Mathworks, Natick, MA), the two-dimensional image gradient was calculated. The image gradient is the rate at which the magnitude of the image changes in all directions. A line was drawn across the vessel at six different angles in 30° increments from horizontal. Image intensity and magnitude of the image gradient were plotted along the line. Linear interpolation was used to estimate values between pixels. The maximum gradients on both sides of the vessel/vessel wall boundary were averaged to yield an estimate of vessel sharpness. Figure 4.4 displays the image magnitude and image gradient for one vessel cross-section. In the corresponding graph of the image gradient, markers ‘A’ and ‘B’ denote the boundary between vessel wall and vessel lumen.

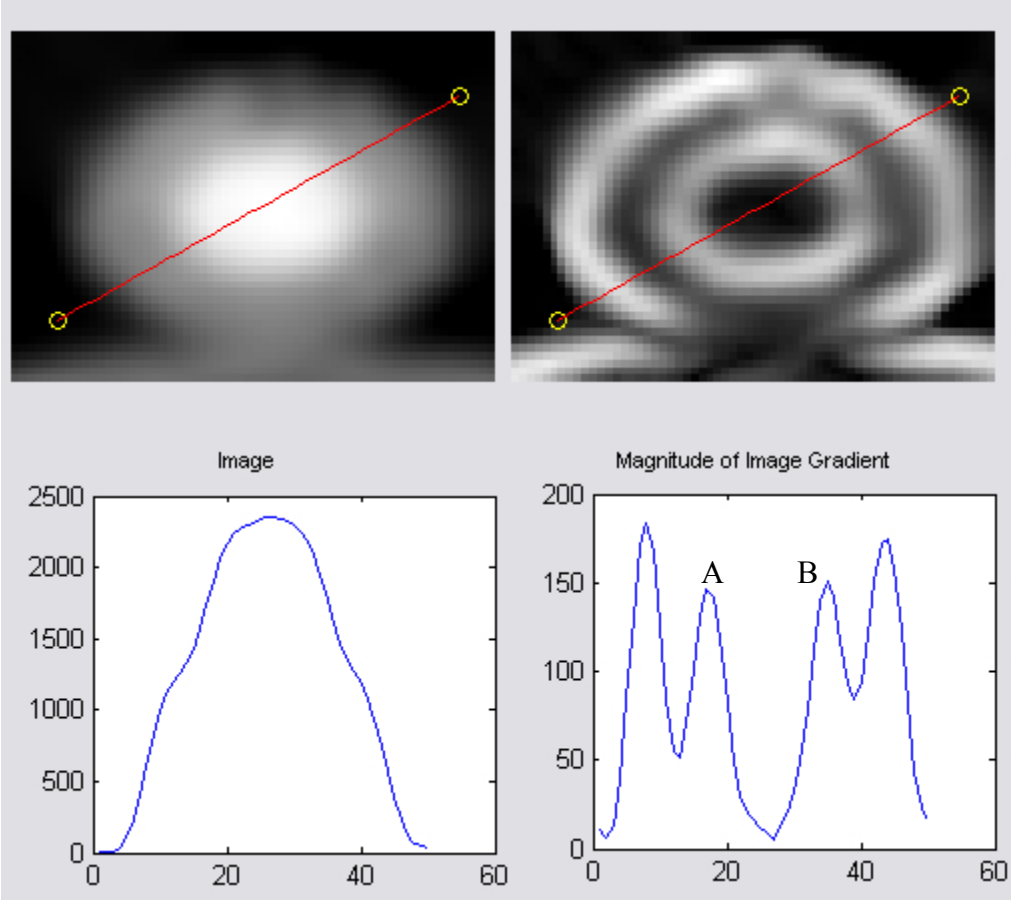

Figure 4.4 Vessel sharpness calculation

Results

CTCA scans were first acquired of the vessel phantoms at rest and then in motion at four simulated heart rates. Table 4.3 displays the average measurements with standard deviations over the four assessments – two repeated readings by two viewers. M1 and M2 denote measurements taken above and below the stenosis, respectively. The known dimensions of the mold used to create the vessel phantoms are included in parentheses. All measurements are reported in millimeters.

Table 4.3 Measurements of Coronary Phantom CT Geometry

		Static	56 bpm	61 bpm	68 bpm	85 bpm
Vessel 1	M1 (2.0mm)	1.8 ± 0.3	1.6 ± 0.2	1.6 ± 0.2	1.9 ± 0.3	UA
	Stenosis (1.08mm)	1.1 ± 0.3	0.9 ± 0.3	0.9 ± 0.2	0.8 ± 0.1	UA
	M2 (2.0mm)	1.9 ± 0.4	1.7 ± 0.3	1.6 ± 0.3	2.0 ± 0.2	UA
	Quality	2.6 ± 0.5	1.8 ± 0.5	1.8 ± 0.5	2.0 ± 0.0	1.0 ± 0.0
Vessel 2	M1 (4.0mm)	3.9 ± 0.3	3.7 ± 0.1	3.8 ± 0.1	3.8 ± 0.3	3.3 ± 0.5
	Stenosis (2.26mm)	1.9 ± 0.2	1.3 ± 0.1	1.5 ± 0.2	1.5 ± 0.2	1.6 ± 0.3
	M2 (4.0mm)	3.9 ± 0.3	3.7 ± 0.1	3.8 ± 0.3	3.6 ± 0.1	3.6 ± 0.2
	Quality	3.4 ± 0.5	2.8 ± 0.5	2.8 ± 0.5	2.8 ± 0.5	2.0 ± 0.0
Vessel 3	M1 (4.0mm)	3.8 ± 0.3	3.6 ± 0.2	3.6 ± 0.1	3.2 ± 0.7	3.5 ± 0.3
	Stenosis (1.82mm)	1.4 ± 0.1	1.4 ± 0.0	1.7 ± 0.2	1.4 ± 0.3	1.3 ± 0.3
	M2 (4.0mm)	3.9 ± 0.2	3.8 ± 0.3	3.8 ± 0.3	3.1 ± 0.9	3.3 ± 0.8
	Quality	2.9 ± 0.7	2.3 ± 0.5	2.5 ± 0.6	2.3 ± 0.5	1.3 ± 0.5

UA – This vessel was unassessable due to poor image quality

Vessel Phantom Geometry Measurements

Two cardiac radiologists reviewed and assessed three coronary artery stenosis phantoms at rest and at four simulated heart rates. Of all the vessels, only the small diameter vessel – 2mm with 1mm stenosis – at 85 beats per minute was deemed unassessable due to extensive motion artifact. A high level of precision was demonstrated by the small standard deviations seen in Table 4.3. The vast majority of

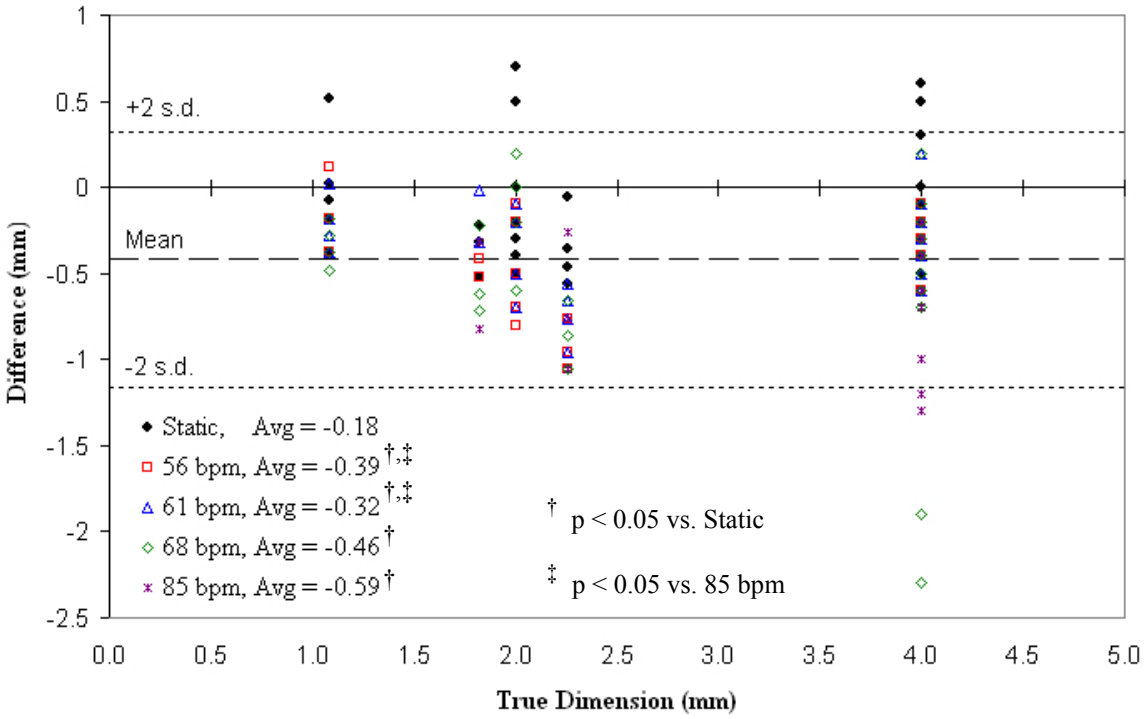

Figure 4.5 Bland-Altman plot of CT vessel measurements

standard deviations were smaller than the CT voxel resolution of 0.4mm. There was, however, a small trend of underestimating the vessel dimensions. This is shown in a Bland-Altman plot (Figure 4.5) and by linear regression (Table 4.4).

Average measurement errors for each scan are included in the legend of Figure 4.5 and show a small trend of underestimation compared to the known dimensions of the vessel molds. The average error for all measurements of the static vessels was 0.18mm (7%) – well below the 0.4mm spatial resolution of the scans. Average error for diameter measurements over all vessels in motion was 0.42mm (17%) – equivalent to the length of one reconstructed pixel. While the average error in measurement was not greater than two pixels for any heart rate, measurement errors seen in all motion scans were

Table 4.4 Linear Regression Coefficients for CT Vessel Measurements

	Static	56 bpm	61 bpm	68 bpm	85 bpm
Slope (y = *m*x)	0.95	0.89	0.91	0.84	0.83
Pearson's Correlation (r)	0.97	0.96	0.97	0.90	0.92

significantly larger than errors from static imaging and error in the 56 bpm and 61 bpm scans were significantly lower than the 85 bpm scan ($p < 0.5$).

Linear regression analysis was constrained by setting an intercept of zero. This is a reasonable constraint for measurements of length where neither the true nor measured dimensions can be negative. Measurements of the vessels with no motion were the most accurate with a linear regression slope of 0.95 and Pearson's correlation value of 0.97. Measurements of the vessels in motion tended to underestimate the known dimensions by 9-17%. Both the error and correlation coefficients were poorer for the faster heart rates of 68 and 85bpm compared to the lower heart rates of 56 and 61bpm; but a strong linear relationship ($r \geq 0.9$) between the known and measured dimensions was seen at all heart rates. It is important to note that this linear regression analysis and Bland-Altman plot do not take into account that the smaller, 2.0mm diameter vessel was not assessable when scanned at 85 beats per minute. No significant difference was seen between 56, 61, and 68 bpm heart rates.

Vessel Sharpness

One contrast-filled, 4mm vessel was analyzed for vessel sharpness using the image gradient under three motion conditions – no motion, 48bpm, and 64bpm. At the

Table 4.5 Vessel Sharpness Measurements

	Average Vessel Sharpness	Standard Deviation	p-value†
Static	157.4	20.7	
48 bpm	163.7	16.8	0.57
64 bpm	159.1	24.1	0.90

† vs. Static

time of this analysis, raw image data was no longer available for higher heart rates. Average vessel sharpness values with standard deviations are reported in Table 4.5. An unpaired-sample, two-tailed T-test was performed and no statistical difference ($p < 0.05$) was observed between any of the motion conditions.

Image Quality

Each vessel was scored for image quality on a scale from 1 to 4 with 1 denoting an unreadable scan and 4 denoting excellent image quality with well delineated vessel boundaries. These scores are included in Table 4.3. On average, the static images were scored higher (2.95) than the images of the vessels in motion (2.08). Images acquired during the 85 bpm scan faired the worst for each vessel with an average score of 1.42. Such motion artifact was seen in the small diameter vessel at 85 bpm to prevent stenosis measurement altogether. Comparing one vessel to another, the 2.0mm vessel with 1.08mm diameter (71%) stenosis was scored the lowest followed by the 4.0mm vessel with 1.82mm diameter (79%) stenosis. The best image quality was seen in the 4.0mm vessel with 2.26mm diameter (68%) stenosis. As was the case with measurement errors of the vessel diameters, all scans taken during motion had significantly poorer image

quality scores ($p < 0.05$) that those of the static vessel and scans at 85 bpm were significantly worst of the group. No significant difference was seen between 56, 61, and 68 bpm heart rates.

Discussion

When modeling fluid flow by way of CFD, accurate geometry of the volume of interest is of the utmost importance. The small size, tortuosity, and constant motion of the coronary arteries have made them a difficult target to image *in vivo*. A new state-of-art in CT technology in the way of 64-detector scanners and advanced multisector image reconstruction algorithms have been proposed in this dissertation as a modality capable of the accurate depiction and modeling of coronary artery geometry for CFD analysis. The results from this study show that accurate geometry can be obtained at low heart rates; but that measurement accuracy and image quality both decreased at the higher heart rate of 85 bpm.

Cardiac radiologists performed blinded measurements of vessel diameter just as they would if reading human cases. While, on average, these measurements underestimated the known geometries of the vessel phantoms, the observed error was very small – ranging from the length of one half to less than one and one half pixels of the reconstructed images. For a typical proximal region of a coronary artery, this is equivalent to an error of approximately 10%. High marks for accuracy have also been shown in two *in vivo* studies comparing minimal lumen area quantification by CTCA and intravascular ultrasound [88, 89].

Greater errors and poorer image quality were seen at the higher heart rates. This was an expected result. As the speed of motion increases, motion artifact and blurring will also increase. It can be noted that in the clinical situation, cardiac patients are most often medicated with beta blockers to steady and lower their heart rate. The dosage of beta blockers is typically adjusted to achieve a heart rate below 70 bpm. A recent study evaluated image quality of 16-detector CTCA in people with and without beta blockers[90]. Diagnostically acceptable images were seen in 100% of the proximal and middle regions of the left main coronary arteries and LADs of the group medicated with beta blockers (mean heart rate: 54 bpm, range: 48-69 bpm.) In the non-medicated group (mean heart rate: 69 bpm, range: 47-97 bpm), only 92% of the left main coronary arteries, 96% of proximal LADs, and 88% of middle LADs were of diagnostic image quality. Another study using a 64-slice scanner found a significant difference in total vessel length that could be visualized without motion artifact for patients with a heart rate less than 65 bpm compared to patients with heart rate greater than 65 bpm[91].

It was also seen that measurement accuracy and image quality were affected by the size of the vessels. Images of the smallest vessel phantom with diameter of 2.0mm were most greatly affected by an increase in the heart rate. At 85 bpm, images of this vessel were unassessable. Similarly, phantom vessel 3 had a greater degree of stenosis than vessel 2 and was given lower scores for image quality. This was also an anticipated result. Smaller diameter vessels should be more affected by motion artifact given their smaller ratio of vessel diameter to distance traveled. This was also seen in the study by Shim, *et al.* in which 88% of middle LAD segments were of diagnostic image quality compared to 96% of the proximal LAD regions of non-medicated patients. Likewise in

the group with beta blockers, only 87% of middle LCX regions were assessable compared to 100% of the proximal LCX.

Vessel sharpness measurements over a smaller subset of heart rates, however, did not show any statistical difference from a static vessel. It was expected that as the speed of motion increases, blurring of the vessel wall also increases – which will decrease the image gradient across the vessel wall. Further study at higher heart rates may be needed to more robustly evaluate this measurement. Raw data from scans at higher heart rates were no longer available at the time the vessel sharpness technique was developed.

In comparison among the scans in motion, scans at 85 bpm demonstrated both significantly larger error in diameter measurements and significantly poorer image quality scores. While a heart rate of 85 bpm and its corresponding temporal resolution (119msec) do result in the largest image reconstruction window as a percentage of the cardiac cycle (17%), no other statistically significant relationship was seen between measurement accuracy or image quality and temporal resolution or temporal resolution as a percentage of the cardiac cycle. It can be inferred from this that a high heart rate has a greater impact on quantitative and qualitative image quality than does the temporal resolution of the scan.

Findings presented in this study and the work of other authors show multi-detector CT coronary angiography capable of highly accurate measurements of coronary artery anatomy for large vessels at low heart rates. Both measurement accuracy and general image quality suffer, however, as the heart rate increases and vessel diameter decreases.

Conclusion

The overall goal of this chapter was to evaluate the accuracy of measurements taken from images of a coronary artery phantom acquired by a 64-detector CT scanner. Phantom arteries of varying diameter and stenosis severity were imaged using a standard, clinical CTCA protocol while undergoing physiologic motion generated by a three-dimensional motion stage. Measurements of vessel phantom geometries and image quality scoring by cardiac radiologists showed that measurements from CTCA scans are highly accurate at low heart rates and larger vessel diameters. No significant difference was measured among simulated heart rates below 70 bpm. CT still struggles, however, to generate diagnostic quality images at higher heart rates above 70 bpm. Under these constraints, coronary artery geometries reconstructed from CT can be used for CFD analysis of blood flow and be assumed to represent accurate *in vivo* geometry of the coronary artery tree. Now with a basis for physical boundary conditions, the next step is to acquire velocity boundary conditions of blood flow for the CFD model. Chapter 5 evaluates the ability of high field 3.0T MRI to measure coronary blood flow.

CHAPTER 5

EVALUATION OF SMALL VESSEL FLOW USING PC-MRI AT 3.0T

Introduction

Despite the high interest in determining coronary flow on a patient-specific basis, this has proved to be quite difficult. Most measures of coronary flow are either invasive and hence cannot be used unless clinically indicated (such as invascular ultrasound), or lack the ability to accurately and reproducibly measure coronary flow (transesphogeal echocardigraphy), or both (thermodilution methods, angiographic grading).

In this study we evaluated the use of navigator echo gated PC-MRI at 3.0T in a flow phantom under controlled flow conditions and subsequently applied the technique to obtain velocity waveforms of the proximal left anterior descending (LAD), left circumflex (LCX), and right coronary arteries (RCA) in healthy volunteers. Our hypothesis is that phase velocity mapping, when combined with navigator echo gating, is a robust technique for making accurate measurements of flow in the proximal coronary arteries. The purpose of the study was to 1) evaluate the accuracy of navigator echo gated, 3.0T PC-MRI in an in vitro study with low velocity and flow rates representative of the coronary arteries, and 2) apply the technique in a series of volunteers to obtain in vivo measurements of coronary blood flow in the left anterior descending (LAD), left circumflex (LCX), and right coronary arteries (RCA).

Methods

Phantom Construction

The coronary model used was a 4.0 mm diameter, non-compliant plastic tube. The tubing was placed on top of a left ventricle phantom model consisting of two concentric Plexiglas cylinders filled with polyvinyl alcohol cryogel (PVA) to simulate myocardium. (Figure 5.1) Steady, laminar flow through the model was provided by a variable speed flow pump (CardioFlow 1000, Shelley Medical Systems, Toronto, Canada) at programmed rates of 2.00mL/s, 2.25mL/s, and 2.50mL/s to simulate a range of typical coronary artery flow rates.

Respiratory motion was provided by an animal respirator which was attached to an inflatable bag placed under the ventricular phantom. The respirator inflated and deflated the bag at a rate of 10 cycles/minute with an excursion of 15-20 mm at the center of the model. The circulating fluid was a 60% glycerin, 40% water mixture designed to approximate the viscosity and T1 properties of blood. Bags of saline were positioned around the phantom to simulate static tissue. Flow rates determined from the MR images

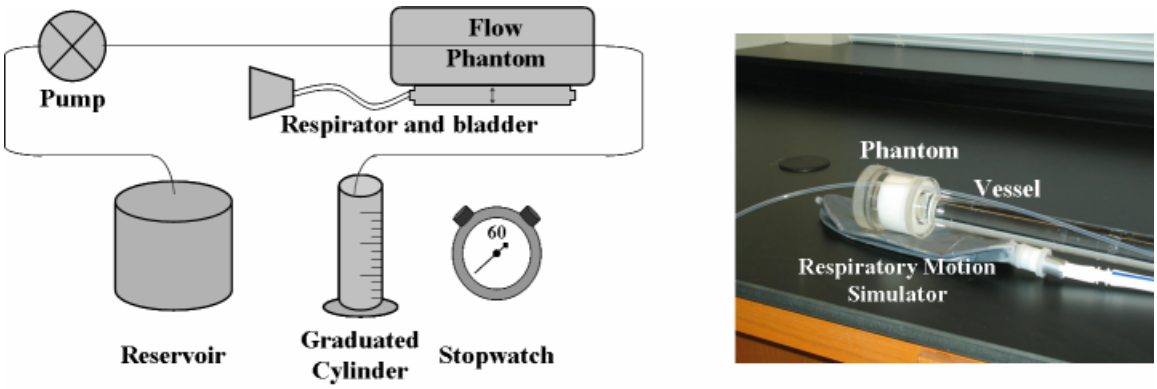

Figure 5.1 Small vessel flow phantom

were compared with flow measured by timed collection of the pump's output during the scan in a graduated cylinder.

PC-MRI Imaging Sequence

All scans were performed on a Philips Medical Systems Intera 3.0 Tesla scanner equipped with a 5-element cardiac phased array coil (Phillips Medical Systems, Best, The Netherlands). For the phantom studies, a single slice plane was oriented perpendicular to the plastic tubing for velocity measurements. The PC-MRI scan sequence used for these studies was a segmented FLASH sequence (3 lines/segment), with flow encoded and non-encoded images acquired in separate heartbeats. Other imaging parameters were: 256mm^2 FOV, 4mm slice thickness, 256x256 matrix, TR/TE/α = 7.0/3.5/15, and the through-plane velocity encoding value was set to 40cm/s. A 60 beats per minute physiology simulator was used to acquire velocity data at 17 temporal phases. The navigator echo was placed over the ventricle phantom and monitored the simulated respiratory motion at the start of each heartbeat. When the air-PVA interface was within 2 mm of the peak displacement, data from that simulated cardiac cycle was accepted; otherwise the phase encoding step was acquired in the next cardiac cycle. Background phase correction was performed by standard methods [92].

Phantom Flow Validation

To assess repeatability, a total of 36 flow scans were acquired (14 scans at 2.0 and 2.5mL/s, 8 scans at 2.25mL/s) over multiple imaging sessions. The PC-MRI images were transferred to a dedicated workstation and evaluated using the FLOW v2005

software package (AZL, Lieden, The Netherlands)[93]. Regions-of-interest (ROI) were drawn for each cross-section on the magnitude images and then copied to the velocity encoded images for each of the time frames. The software then multiplies the velocity values by the pixel area for all pixels within the ROI. A sum of all the pixel values equals flow through the vessel during the time point (phase) of the cardiac cycle represented by that image. Values of average cross-sectional velocity (cm/s) and flow (mL/s) for each time point were exported to a spreadsheet for comparison and analysis. The difference between flow measurements calculated by PC-MRI and by timed collection was analyzed as root mean squared (RMS) error:

$RMS = \frac{\sum \sqrt{(flow_{collection} - flow_{PC-MR})^2}}{N}$. This parameter retains the magnitude of the difference but not the sign such that positive and negative errors do not average out. Variability of the PC-MRI measurements was assessed by the standard error of the mean, defined as: $E = \frac{StdDev}{\sqrt{N}}$.

In Vivo Coronary Flow

Coronary artery blood flow was measured in nine volunteers (2 female, 7 male; age 22-38) with no previous history of cardiovascular disease for a total of 16 coronary vessels (6 RCA, 6LAD, 4 LCX). Informed consent was obtained prior to MRI scans. The protocol used to acquire coronary flow velocity scans is detailed here and summarized below in Table 5.1. Volunteers' heart rates were monitored by a four-lead ECG as they lay supine on the scanner table. To plan the flow measurements, a transverse stack of 35-40 slices was acquired over the heart using a navigator echo gated

Table 5.1 MRI Scan Parameters for *In Vivo* Protocol

		TR / TE / α	Resolution, mm
1	Scout	3.80 / 1.82 / 20°	1.76 x 1.76 x 10
2[a]	Balanced Fast-Field Echo 50 phase cine	3.79 / 1.89 / 45°	1.17 x 1.17 x 8.0
3[b]	Segmented Gradient Echo MRA 40 slices	5.39 / 1.63 / 20°	0.52 x 0.52 x 3.0
4[b,c]	Segmented Gradient Echo MRA Three-point planned	5.39 / 1.63 / 20°	0.52 x 0.52 x 3.0
5[b,c]	Phase Velocity Map	7.56 / 3.56 / 30° V_{enc} = 35cm/sec	1.05 x 1.05 x 4.0

[a] breath-hold scan; [b] navigator-echo gated scan; [c] for each coronary artery (LAD, LCX, and RCA)

3D "whole heart" coronary MR angiography sequence which has been described previously by Weber, *et al.* [94]. Briefly, image acquisition was gated to the ECG signal and occurred during a period of cardiac quiescence in mid-to-late diastole as determined by a 50 phase balanced fast-field echo cine scan. The navigator echo was placed over the right hemi-diaphragm and was acquired for each cardiac cycle. Total imaging time for the axial MRA stack was approximately 3 minutes during free breathing.

From this stack of transverse images, a scan plane was selected which passed through the coronary ostium and points in the mid and distal regions for each of the left anterior descending, left circumflex or the right coronary artery. The same navigator echo gated MRA sequence was used in the double oblique plane along the determined angles with 10 slices to ensure visualization of the vessel in the imaging plane. Example images from one volunteer are shown in Figure 5.2.

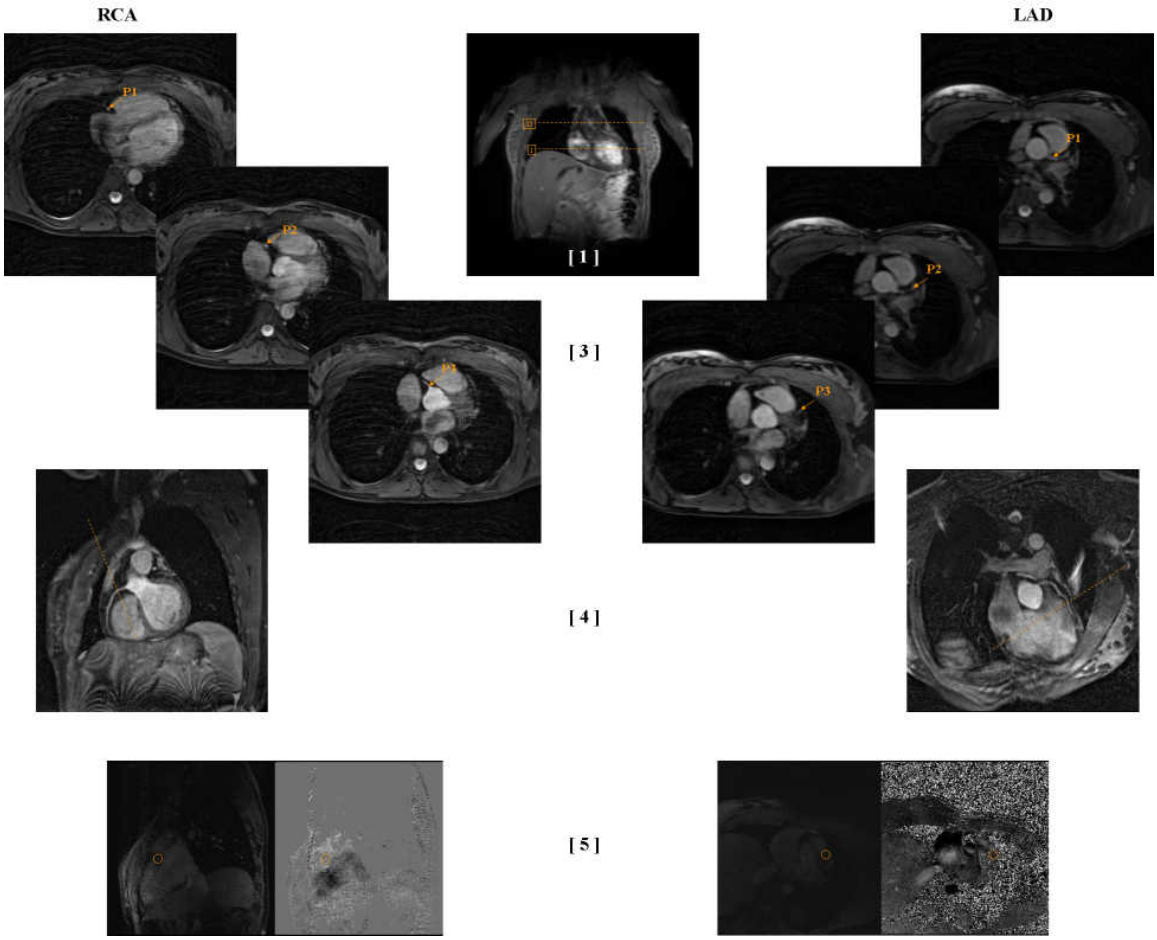

Figure 5.2 Volunteer coronary MRI protocol

Once the target artery was localized in-plane, a navigator echo gated PC-MRI scan was positioned perpendicular to a straight region of the coronary artery at a location of 2.6±1.3cm from the ostia of the RCA at the aorta, 3.0±1.2cm from the aorta along the LAD and 3.4±0.4cm along the LCX – making sure that the LAD and LCX scans were located distal to the left coronary artery bifurcation. Spatial resolution for the PC-MR scan was 1mm x 1mm in-plane with 4mm through-plane slice thickness. Through-plane velocity encoding was set to 35cm/s. The PC-MRI sequence described for the phantom

study was implemented and acquired velocity data for 11-19 cardiac phases depending on the subject's heart rate. Flow measurements were evaluated using the FLOW v2005 software package as described previously.

Results

Phantom Flow Validation

Flow measurements in the phantom model made with the navigator echo gated PC-MRI sequence agreed well with values obtained with timed collections at all flow rates (Table 5.2). Root mean squared (RMS) error in flow measurements over all imaging sessions was 15% and did not exceed 20% for any flow rate during any session. Standard error of the PC-MRI measurements ranged from 3% to 7% of the calculated flow rates.

Table 5.2 Accuracy of Flow Rates Measured by PC-MRI

True Flow Rate mean ± s.d. (mL/s)	PC-MRI Flow Rate mean ± s.d. (mL/s)	RMS Error (mL/s, %)	Standard Error (mL/s, %)
1.97 ± 0.02	1.89 ± 0.23	0.24 (12%)	0.06 (3%)
2.23 ± 0.02	2.30 ± 0.43	0.39 (18%)	0.15 (7%)
2.48 ± 0.01	2.36 ± 0.39	0.39 (16%)	0.10 (4%)
	Average over all flow rates	**0.34mL/s (15%)**	**0.11 (5%)**

In Vivo Coronary Flow

MR angiographic images of the coronaries and phase velocity images of LAD and RCA flow were successfully obtained in all subjects. Coronary artery blood flow velocity was measurable in 62/79 total cardiac phases of LAD flow, 51/51 phases of LCX flow, and 111/113 phases of RCA flow – 224/243 overall (92%). Flow in the remaining phases was not measurable due either to blurring from motion artifact or the vessel's proximity to the ventricular blood pool.

Average values of peak velocity, time-averaged velocity, and flow across all volunteers are reported in Table 5.3. Graphs of average time-resolved velocity curves for the LAD, LCX, and RCA are shown with standard deviations in Figure 5.3.

Table 5.3 Average Volunteer Coronary Flow

	Peak Velocity mean ± sd (cm/s)	Average Velocity mean ± sd (cm/s)	Average Flow mean ± sd (mL/min)
LAD	13.6 ± 6.9	6.8 ± 4.3	29.7 ± 17.4
LCX	13.6 ± 4.4	8.0 ± 3.8	28.4 ± 19.7
RCA	13.5 ± 5.3	6.0 ± 1.6	37.7 ± 19.0

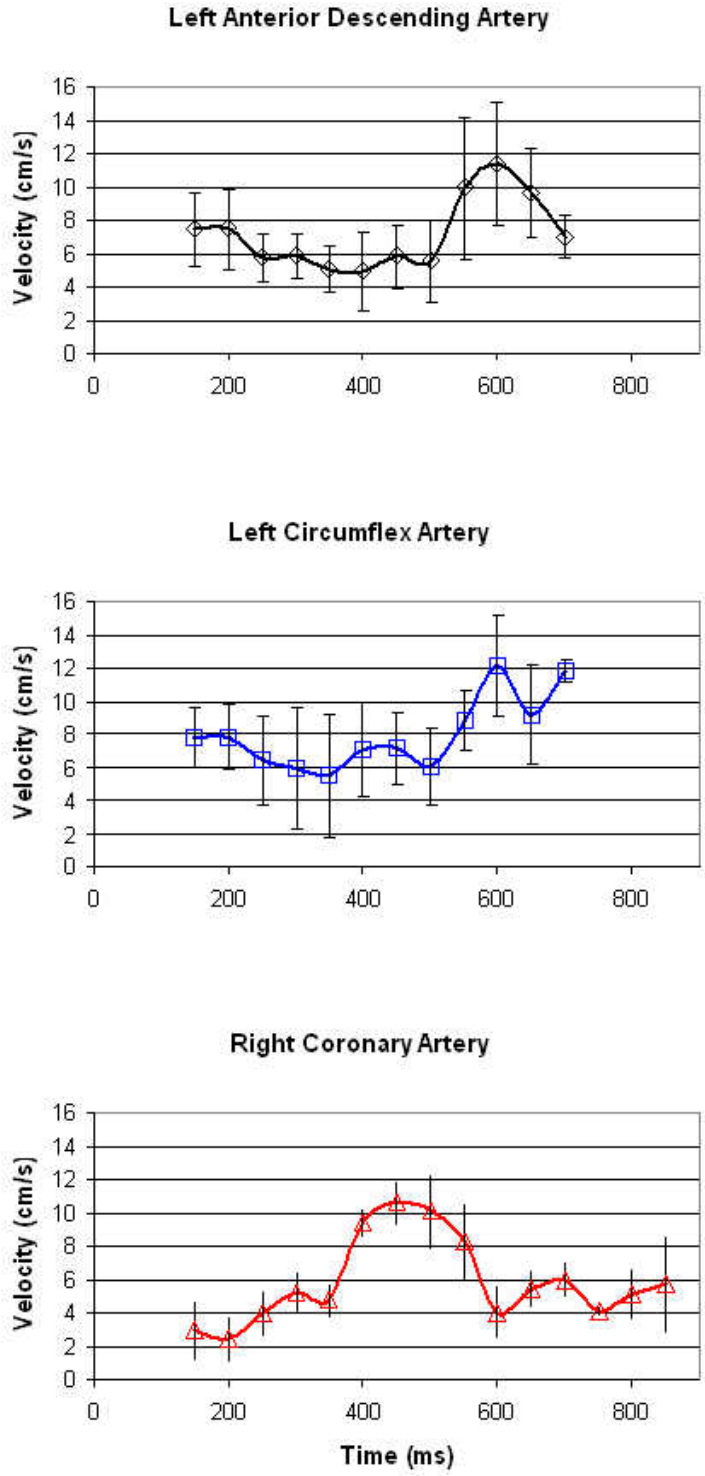

Figure 5.3 Average velocity curves for LAD, LCX, and RCA

Discussion

Phantom Flow Validation

Results from the phantom study showed navigator echo gated phase velocity mapping at 3.0T to have an average error of 15% of the known flow rate and a variability of 5% over repeated measurements. It was noted, however, that the error of the flow measurements varied to a greater degree from one scanning session to the next. The magnitude error for individual scans ranged from 6 – 20%, generally an acceptable range for clinical applications.

A 2005 study by Lotz, et al. has shown that 3.0T PC-MRI can be used to measure flow with a high degree of accuracy and precision in large diameter phantom vessels[66]. Their study reported an average error of only 0.6% ± 0.6% for a range of flow rates between 0.5 and 1.75 liter/minute (8.3-21.9mL/s) in a flow phantom with inner diameters greater than 10mm. Repeated measurements of a single flow rate resulted in deviations of 0.1%.

Larger errors presented in this chapter indicate that spatial resolution and motion remain limiting factors in the accuracy of PC-MRI flow measurements in small diameter vessels. A previous in vitro study of 1.5T small vessel PC-MRI concluded that 16 pixels or more are needed across the diameter of a vessel in order to consistently measure flow rates accurate to within 10%[61]. This allows better relative resolution and description of the peak velocities seen at the centerline of parabolic tube flow. Flow measurements in vessels with a lower pixel-to-diameter ratio tend to underestimate peak velocities and can also be affected by partial-volume artifacts at the vessel wall. No previous small diameter (<6mm) phantom studies at 3.0T were found for comparison with our PC-MRI

validation study. Results from our study demonstrated errors for 3.0T navigator echo gated PC-MRI of less than 20% as compared to flow measurements calculated by timed collection for a 4mm vessel phantom.

In Vivo Coronary Flow

Clear angiographic images of the LAD, LCX, and RCA were successfully obtained in all subjects. Cross-sectional views of the vessel lumens and blood flow were observed in 92% of total cardiac phases. These images allowed visualization of coronary vessel boundaries without motion artifact. Average flow rates and peak velocities of 29.7±17.4ml/min and 13.6±6.9cm/s were seen in the LAD. Corresponding values for the LCX were 28.4±19.7ml/min and 13.6±4.4cm/s. Average flow and peak velocity in the RCA were 37.7±19.0ml/min and 13.5±5.3cm/s. Time-averaged velocity of the blood flow was 6.8±4.3cm/s in the LAD, 8.0±3.8cm/s in the LCX, and 6.0±1.6cm/s in the RCA. High standard deviations can be attributed to several things including subject-to-subject variability, through-plane cardiac motion, or small sample size.

Peak blood flow in the RCA occurred predominantly in early to mid diastole as the surrounding myocardium relaxed after systolic contraction. Low flow during systole was also observed in the LAD and LCX but less of a peak was seen as flow was more evenly distributed across the diastolic portion of the cardiac cycle. These flow patterns are contrary to those seen in the aorta, carotid arteries, and most other peripheral arteries of the cardiovascular system. Peak flow in these arteries is typically seen during systole coinciding with the expulsion of blood from the left ventricle. Flow decreases during diastole after the aortic valve closes. In the cardiac vessels, however, contraction of the

surrounding myocardium during systole raises the pressure in the coronary arteries, decreasing the pressure gradient between the aorta and the coronary arteries and restricting coronary blood flow until the myocardium relaxes during diastole [95].

A noticeable phase shift can be seen between flow in the RCA and in the left coronary arteries – with the RCA experiencing an increase in flow prior to the LAD and LCX. A review of current literature does little to confirm or refute this finding. In one study, a phase shift between the right and left coronary circulation is demonstrated [96]. In another, there seems to be no phase shift [97]. And in yet another, a phase shift is seen in the opposite direction with peak flow in the left main coronary artery occurring before peak flow in the RCA [98].

Previous studies of breath-hold PC-MRI at 1.5T have presented varying results for velocities and flow rates in the coronary arteries. In an investigation of the effect of cardiac motion on flow assessment, Hofman, et al., found time-averaged velocity in six healthy subjects was 7±2cm/s and volume flow was 30±10ml/min in the RCA [99]. Another study of eight healthy volunteers presented mean flow rates of 59±15ml/min in the LAD and 38±10ml/min in the RCA [100]. Results presented in this chapter fall within the bounds of these earlier findings. The navigator echo PC-MRI protocol is free-breathing and advantageous for use in patients that may be noncompliant or unable to hold their breath repeatedly at the same location or for extended periods of time (>10s).

A significant issue to consider is inter-patient variability. The heart rate of volunteers in this study ranged from 50bpm to 105bpm. This alone causes difficulty in creating an "average" velocity curve or drawing broad conclusions about the population – without even considering the shape of the patients' velocity curves. A 2006 study by

Schiemann, *et al.* of eighty-three patients without coronary artery disease investigated flow curves in the LCA and RCA and found 61% of the vessels to have a biphasic velocity pattern[98]. The remaining velocity curves were monophasic or demonstrated reduced fluctuation nearing steady velocities. The peak velocities measured for each patient ranged from 16 - 30 cm/s in the LCA and 10 - 18 cm/s in the RCA. This variability suggests that an "average" velocity curve may be inappropriate for CFD modeling of patient-specific coronary flow or wall shear stress.

Conclusion

The goals outlined for this chapter were to evaluate the accuracy of small vessel velocity measurements obtained by 3.0T PC-MRI and to develop a protocol for the *in vivo* measurement of coronary artery blood flow velocity in human subjects. 3.0T PC-MRI was shown to have accuracy comparable to that of other techniques for velocity measurements in small diameter blood vessels. Human volunteer studies were successful in obtaining velocity waveforms for the LAD, LCX, and RCA coronary arteries. Average waveforms for those arteries were presented. Variation among the volunteers' respective waveforms, however, leaves open the question of whether a standardized velocity curve would be appropriate for use in patient-specific CFD calculations of WSS. The following chapter of this dissertation seeks to answer this question by developing a three-dimensional coronary artery model from CT scans for CFD analysis and comparing wall shear stress simulations for that model using three different sets of velocity boundary conditions.

CHAPTER 6

CFD CALCULATION OF CORONARY ARTERY WALL SHEAR STRESS

Introduction

In the previous two chapters, this dissertation has established the accuracy of multi-detector CT and 3.0T PC-MRI for acquiring measurements of coronary artery geometry and blood flow velocity, respectively. Phantoms with known geometries and known flow rates have been used as surrogates for *in vivo* imaging of human subjects. While a necessary step for validation, the ultimate goal is development of a clinical application. This chapter details the incorporation of the previous chapters' work with human subjects for a clinically relevant application – the calculation of coronary artery WSS and the spatial and temporal distribution of regions with high or low WSS.

This study is not concerned only with the methodology of creating WSS simulations from patient-specific imaging data. In the original motivation section and problem statement, the allure of coronary blood flow modeling without MRI was established due to the prevalence of implanted devices in patients awaiting heart transplants. To assess the importance of MRI-acquired, patient-specific, time-resolved velocity curves, coronary artery WSS will be calculated from CFD models using patient-specific artery geometry and one of three different velocity boundary conditions. The velocity boundary conditions that will be compared are (1) patient-specific, time-resolved velocity from 3.0T PC-MRI; (2) population-averaged, time-resolved velocity from a

series of volunteer coronary artery velocity measurements; and (3) patient-specific, steady velocity. The goals of this study were to create an image based, patient-specific CFD model for calculating coronary artery WSS using multi-detector CT coronary angiography and 3.0T PC-MRI and to determine the necessity of patient-specific, time-resolved velocity boundary conditions for calculating WSS distributions.

Methods

Several steps were involved in the experimental methods for this study from initial image acquisition to the three-dimensional model construction to the CFD simulation and subsequent analysis of WSS values and distribution.

Subjects

Two non-symptomatic, adult male volunteers (age: 46 and 54) with no known coronary artery disease were recruited to this study. Approval for the study was granted from the Emory University Institutional Review Board (IRB). Informed consent was obtained from subjects prior to the study.

Image Acquisition

The CTCA and PC-MRI imaging protocols used in this study have been detailed at length in the previous chapters and so will only be recalled briefly here. Subjects first underwent a CT coronary angiography scan on a 64-detector scanner (Somatom Sensation 64, Siemens Medical Solutions, Erlangen, Germany) at the Emory Clinic

Cardiac Imaging Center. Standard CTCA protocol was followed including retrospective ECG-gating and timed scanning after intravenous contrast injection. Axial images were acquired for full volume coverage of the heart. The data set was then transferred to a dedicated workstation for post-processing.

The MRI protocol followed was the same as described in the "*In vivo* Coronary Flow" section of the previous chapter. The lone exception to that protocol was that the vessel of interest for this study was the left main coronary artery (LM) proximal to the LAD – LCX bifurcation rather than the LAD and LCX, themselves. Flow in the RCA was not considered in this study. A series of MRA scans were acquired to provide a planar view of the LM and the LAD – LCX bifurcation. A velocity-encoded PC-MRI scan was positioned midway along the length of the LM between the aorta and the bifurcation. Adequate spacing on either side of the scan plane is important due to cardiac motion that may bring either the aorta or the bifurcation into the thickness of the scan slice at some point of the cardiac cycle. This can be especially problematic in subjects with short LM arteries. Velocity-encoded images of LM blood flow were acquired for 15 cardiac phases in Subject #1 and for 14 cardiac phases in Subject #2. Images were transferred to a dedicated workstation for analysis using the FLOW software package and velocity data was calculated as previously described.

Patient-Specific, Time-Resolved WSS Simulation

Vessel Model Construction

Raw CTCA data was processed by a cardiac radiologist using the CardIQ image processing platform (GE Healthcare, Chalfont St. Giles, UK). Using a 3D vessel

segmentation program, seed points were planted at the proximal end of the LM and at the distal ends of the branch vessels of the left coronary artery tree (LAD, LCX, first diagonal, second diagonal, and obtuse marginal). Cross-sectional contours of the vessel lumens were segmented at 2mm increments along each artery's centerline and written to the header file of a three-dimensional DICOM image as a series of vertices. Since the actual DICOM image itself could not be read into a solid geometry program, the vertex data embedded in the header file had to be extracted. This was accomplished using an in-house program written by Dr. Tracy Faber in the Emory University Hospital Department of Radiology. For the purposes of this study, only vertex data from the LM and proximal regions of the LAD (24mm and 25mm) and LCX (20mm and 26mm) were included in the vessel model for CFD analysis.

Three-dimensional vertex data was imported to the GAMBIT solid geometry and mesh construction program (Fluent Inc., Lebanon, NH) for development of the vessel

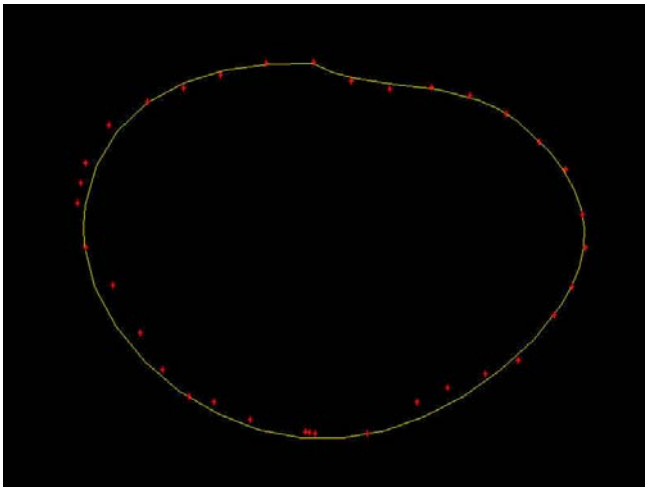

Figure 6.1 Example of vessel cross-section vertex data and NURBS curve

model. Each cross-sectional vessel contour consisted of a series of vertices. Depending on the local diameter of the vessel, the cross-section could be defined by as few as 7 or as many as 70 or more vertices. For each cross-section, a nonuniform rational B-spline (NURBS) curve was fit to the vertex data to form a continuous edge to define the cross-section (Figure 6.1). A tolerance value of 0.2mm was allowed in the calculation of the NURBS curve. This tolerance is equal to half the length of one pixel from the reconstructed CT data and constrains the curve to the area of the raw data vertices without forcing the curve through each vertex. While it may seem like a trivial difference, this step allows for a smoother cross-section, smoother resulting vessel, and better representation of the physiological anatomy.

A problem encountered in one subject, and which could be expected to be seen in the patient population, is that of calcium deposits near the coronary artery lumen. Because the CT attenuation of calcium is close to that of the CT contrast agent used, automated segmentation programs will often be unable to distinguish a boundary between the contrast agent inside the vessel and calcium deposits outside the vessel. An example

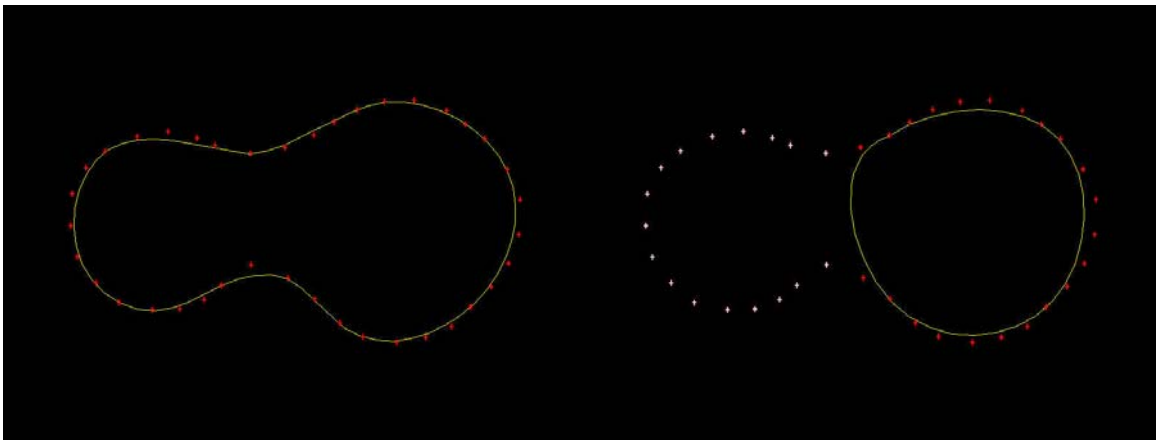

Figure 6.2 Vessel cross-section with calcium deposit and corrected NURBS curve

of such a situation is illustrated in Figure 6.2. In this instance, it was necessary to manually select only those vertices believed to mark the vessel boundary and exclude vertices around the calcium deposit. The use of a NURBS curve to define the vessel cross-section allows for a smooth connection across the gap without having to guess where vertices would have been located had the calcium not been present. This manual correction usually must be done for two or more consecutive cross-sections depending upon the size of the calcium deposit along the length of the vessel.

Once a NURBS edge has been defined for each cross-section, NURBS surfaces are used to form an enclosed vessel. One surface is defined using the cross-sections from the beginning of the LM to the end of the LAD. Another surface is defined using the cross-sections from the start of the bifurcation to the end of the LCX. These surfaces are then used to create vessel volumes of their corresponding regions – an LM-LAD and an LCX volume. Those two volumes are then merged together to form one contiguous volume. Once the control volume has been established, a tetrahedral meshing scheme is utilized to mesh the vessel volume with tetrahedral volume elements with a maximum edge length of 0.3mm (Figure 6.3). This size was chosen for the volume elements because it is small enough to allow sufficient velocity data points across a vessel cross-section for accurate shear rate calculation while not being so small to extend the computation time of the CFD analysis beyond a reasonable period or cause a divergence in the CFD solution.

In total, the first vessel model had 247,053 tetrahedral volume elements inside the vessel lumen and 22,892 triangular faces along the vessel wall. The second model had 202,221 tetrahedral volume elements inside the vessel lumen and 22,148 triangular faces

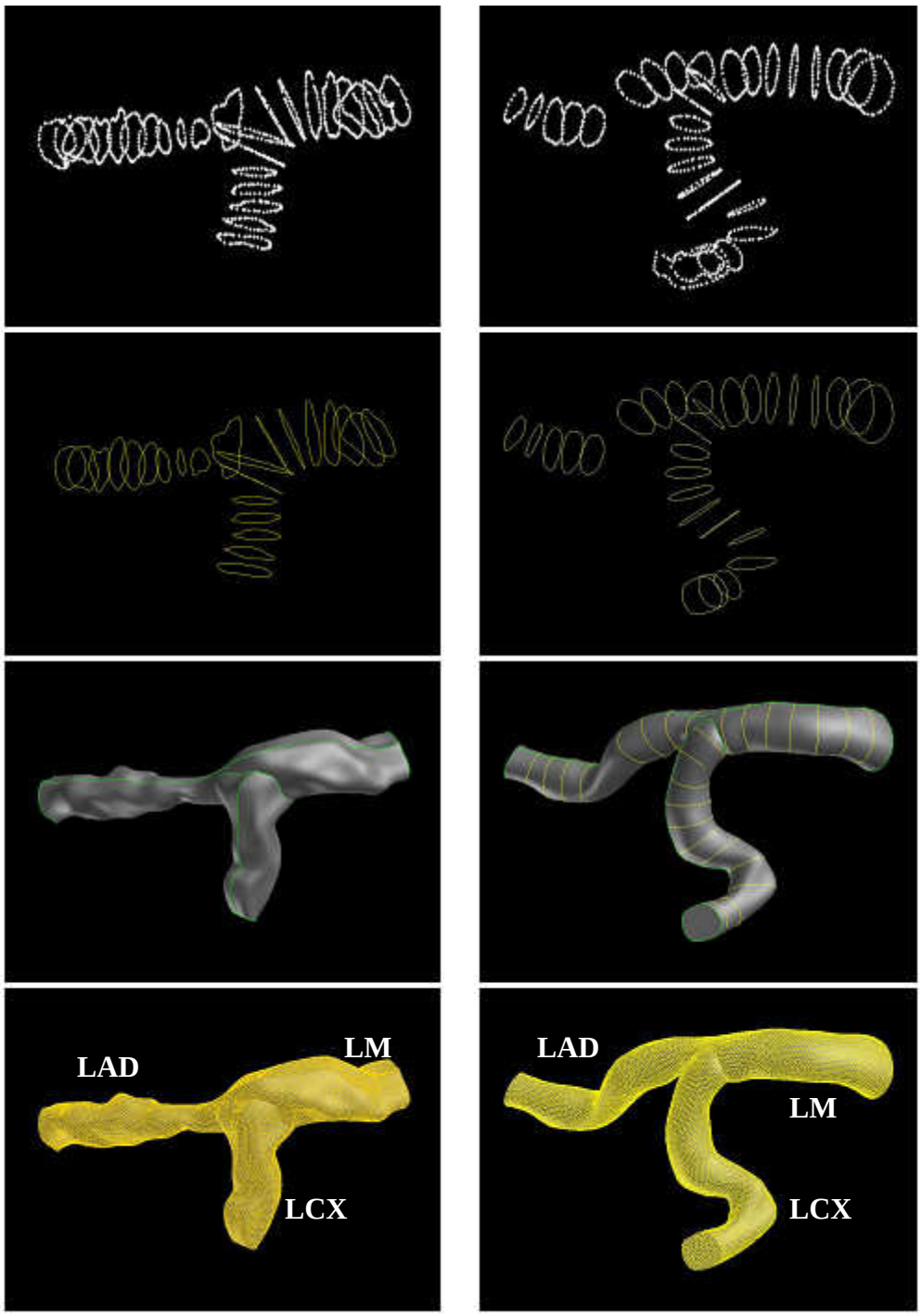

Figure 6.3 Progression of vessel model construction for two subjects

along the vessel wall. The inlet face of the proximal LM was defined as a "Velocity Inlet" for purposes of CFD modeling while the outlet faces of the LAD and LCX were both defined as constraint-free "Outflows." The control volume was defined as a fluid.

Velocity Boundary Conditions

Three different velocity boundary conditions were chosen for comparison of WSS calculation – patient-specific, unsteady flow; patient-specific, steady flow; and population-averaged, unsteady flow.

Patient-specific, unsteady velocity curves were taken from the subjects' MR-PVM scans of blood flow through the LM coronary artery. Linear interpolation was performed on each subject's velocity curve to increase the temporal resolution of the unsteady CFD simulation – a total of 27 cardiac phases for Subject 1 and 29 cardiac phases for Subject 2. The time between each velocity point was 24 milliseconds – equal to half the temporal resolution of the PC-MRI scan. The CFD simulation could only include segments of the cardiac cycle during which velocity measurements had been acquired. For this reason, the first 150ms of the cardiac cycle were omitted because of the navigator-echo pulse. This is not expected to greatly affect the WSS calculation as typically there is low coronary flow during this period of systole. Cross-sectional average velocity at each cardiac phase was used opposed to a spatially defined velocity profile for all nodes of the vessel lumen.

Patient-specific, steady flow was defined as the average velocity of blood flow over all cardiac phases acquired by the patient-specific PC-MRI scans. This value was 4.0cm/s for Subject 1 and 3.7cm/s for Subject 2.

Population-averaged, unsteady flow was defined by the collection of volunteer coronary velocity measurements detailed in Chapter 5 of this dissertation. While flow velocity was not measured in the LM for that study, LM flow can be calculated based upon the average velocity curves for the LAD and LCX. Assuming the absence of other branching vessels, flow in the LM is equal to the summation of the average velocities in the LAD and LCX multiplied by their respective cross-sectional areas. Velocity in the LM can then be calculated by dividing LM flow by LM cross-sectional area. Using the average LAD and LCX velocity curves from Chapter 5 and average dimensions of the left coronary tree found in previous literature [27], it was determined that blood flow velocity in the LM is approximately 70% that of the velocity in the LAD. Thus, the average LAD velocity curve presented in the previous chapter was scaled by 70% and used to represent a population-averaged, unsteady velocity curve for the LM.

CFD Simulation

It should be noted that this study is not intended to be an exhaustive study of coronary blood flow. Rather, the purpose of the study is a simple model approach to compare the results from a series of different velocity boundary conditions. While the image-based mesh offers improvements in geometric accuracy compared to previous models, the control volume is considered to be a motionless rigid body. Other authors have developed more complex models of cardiovascular blood flow taking into account factors such as vessel motion, compliance, and spatially resolved velocity inlet conditions and have shown that these factors have non-trivial contributions to the flow solutions. For a greater exploration of these effects, I recommend the publications and dissertation

of Suo Jin at Georgia Institute of Technology whose work with CFD in the aorta and coronary arteries laid much of the foundation for my CFD studies[75, 96, 101, 102].

The three-dimensional, tetrahedral mesh created from patient-specific, CT imaging was loaded into the CFD solver FLUENT (Fluent Inc., Lebanon, NH) for computational modeling of coronary artery blood flow. The control volume was treated as a Newtonian, incompressible fluid and assigned the rheological properties of human blood – density of 1060kg/m^3 and viscosity of 0.0027N·s/m^2. For simulations using patient-specific and population-averaged, unsteady velocity boundary conditions, the default settings were accepted for an unsteady, 1st-order implicit solution approach to the Navier-Stokes equations of fluid flow. Short subprograms were written to define the time-resolved velocity values for each patient-specific and population-averaged velocity curve. These programs were then applied as uniform velocity boundary conditions at the LM inlet of the coronary artery mesh. For simulations using patient-specific, steady flow, the calculated average velocity value over the course of each subject's cardiac cycle was assigned as a constant velocity at the LM inlet.

The FLUENT CFD package utilizes an iterative approach to solving the Navier-Stokes and continuity equations – proceeding until the error, or residual, from one solution to the next is below a set convergence criterion. Again, default settings for convergence criteria (0.001) were accepted for residuals of continuity as well as x-, y-, and z-velocities. Each phase of the unsteady simulations and the solution to the steady simulation were allowed to iterate until convergence was reached. At this point, the direction and magnitude of velocity was known for every tetrahedral cell within the control volume at each cardiac phase. Values of WSS for each node along the vessel

walls were calculated by FLUENT and exported to MATLAB (The Mathworks, Inc., Natick, MA) for further analysis.

Time-Averaged WSS Comparison

As was discussed in Chapter 5, different people can have different coronary artery velocity curves: biphasic, monophasic, etc. [100] Thus, it may not be prudent to compare a patient-specific simulation against a population-averaged unsteady simulation on a phase-by-phase basis. In order to compare WSS between two different unsteady flow simulations or between an unsteady flow simulation and a steady flow simulation, time-averaged WSS must be analyzed. Values of WSS for each node along the vessel walls from all simulations were imported into MATLAB. For the two unsteady simulations, time-averaged WSS and WSS oscillation, or range, for each node was calculated over the cardiac cycle. For those time-averaged WSS values and the WSS values from the steady-state simulation, the average WSS and standard deviation were calculated for the entire vessel.

Areas of High/Low WSS Comparison

We compared areas of locally high or low time-averaged WSS relative to the whole vessel as calculated by using different velocity boundary conditions for the CFD model. Areas of each vessel were said to have high or low WSS if the time-averaged WSS value for a given node was more than one standard deviation above or below the mean WSS value for the entire vessel. These regions of relatively high or low WSS could then be compared across the three simulations. The patient-specific, time-resolved

simulation was considered the gold standard for comparison. If a node with high or low WSS in the two simplified models corresponded to a high/low WSS node in the gold standard model, that node was said to be "coincident with" the gold standard. The overall *percent coincidence* of a simplified model was defined as the ratio of coinciding high/low WSS nodes in that model to the total number of high/low WSS nodes in the patient-specific, time-resolved model. Linear regression analysis was also performed on WSS values within these regions to determine the fit of each simplified CFD model to the patient-specific model.

Results

Patient-Specific, Time-Resolved WSS Simulation

Wall shear stress was calculated for the left coronary artery bifurcation of two subjects using an image-based model of the coronary vessels and a patient-specific, time-resolved velocity curve of blood flow through the LM. Sample frames of the WSS distributions can be seen in Figure 6.4.

In the example shown in Figure 6.4, areas of high WSS can be seen at the inlet of the LM, the outlet of the LCX, and along a mild stenosis of the LAD immediately distal to the bifurcation. It should be noted that WSS values at the inlet of the LM are artificially high due to the use of a uniform velocity profile boundary condition. The boundary condition is defined as a uniform velocity across the face of the inlet rather than a developed, Poiseuille flow profile. In actuality, LM flow has been observed to exhibit a more parabolic velocity profile with dominant flow towards the myocardial side of the

vessel. Coronary artery flow becomes fully developed in five to seven millimeters so as not to affect WSS calculation for the remainder of the vessel model [96, 102]. A short entry region of 2mm was excluded from analysis of total vessel average WSS for comparison of the different CFD simulations to omit high WSS caused by the uniform velocity profile. WSS is elevated at the truncated outlet of the LCX and the LAD stenosis due to narrowing of the vessel. Areas of low WSS can be seen at the epicardial surface of the bifurcation and the distal shoulder of the LAD stenosis.

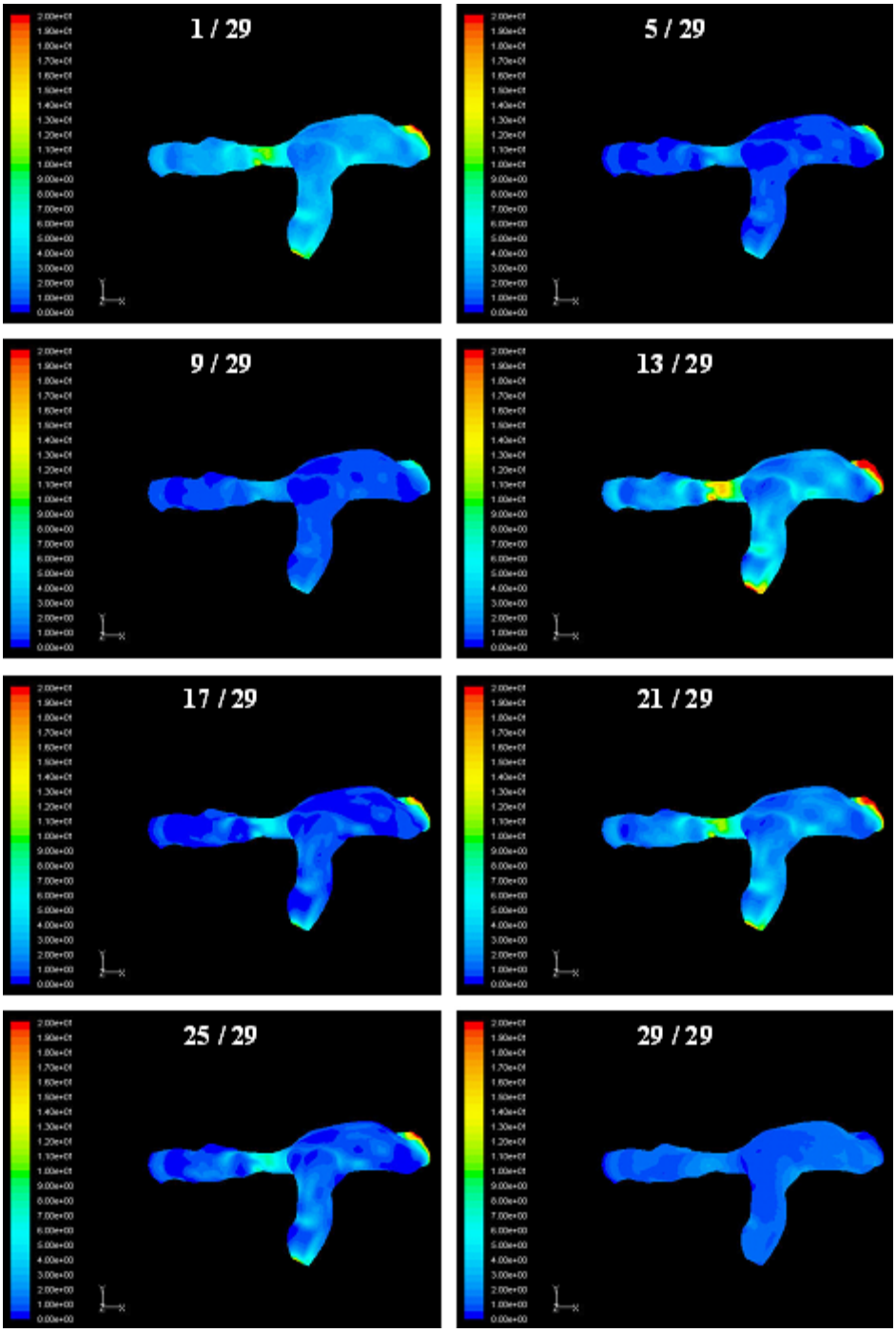

Figure 6.4 Surface plots of patient-specific WSS over cardiac cycle

Time-Averaged WSS Comparison

Time-averaged WSS is presented for all simulations of both subjects in Figure 6.5. Vessel-average WSS and WSS range are listed in Table 6.1. For the patient-specific, unsteady flow calculations, time-averaged WSS values ranged from 1-26 dynes/cm^2 (whole vessel average: Subject 1 = 2.19 dynes/cm^2, Subject 2 = 6.51 dynes/cm^2). The patient-specific, steady state calculations resulted in a WSS range of 1-23 dynes/cm^2 (whole vessel average: Subject 1 = 1.85 dynes/cm^2, Subject 2 = 4.09 dynes/cm^2). Using population-averaged, unsteady flow boundary conditions resulted in a WSS range of 1-28 dynes/cm^2 (whole vessel average: Subject 1 = 2.50 dynes/cm^2, Subject 2 = 6.06 dynes/cm^2). Point-to-point comparison of time-averaged WSS was performed for each simplified model against the reference standard using a paired-sample

Table 6.1 Time-Averaged WSS Calculations

		Patient-Specific, Unsteady	Patient-Specific, Steady	Population-Averaged, Unsteady
Subject 1	Average WSS, dynes/cm^2	2.19 ± 2.11	1.85 ± 1.98†	2.50 ± 2.38†
	Range, dynes/cm^2	14.06	15.96	13.69
Subject 2	Average WSS, dynes/cm^2	6.15 ± 3.05	4.09 ± 2.40†	6.06 ± 3.20†
	Range, dynes/cm^2	25.41	23.07	27.69

† point-to-point comparison *not equal* to Patient-Specific, Unsteady ($p < 0.01$)

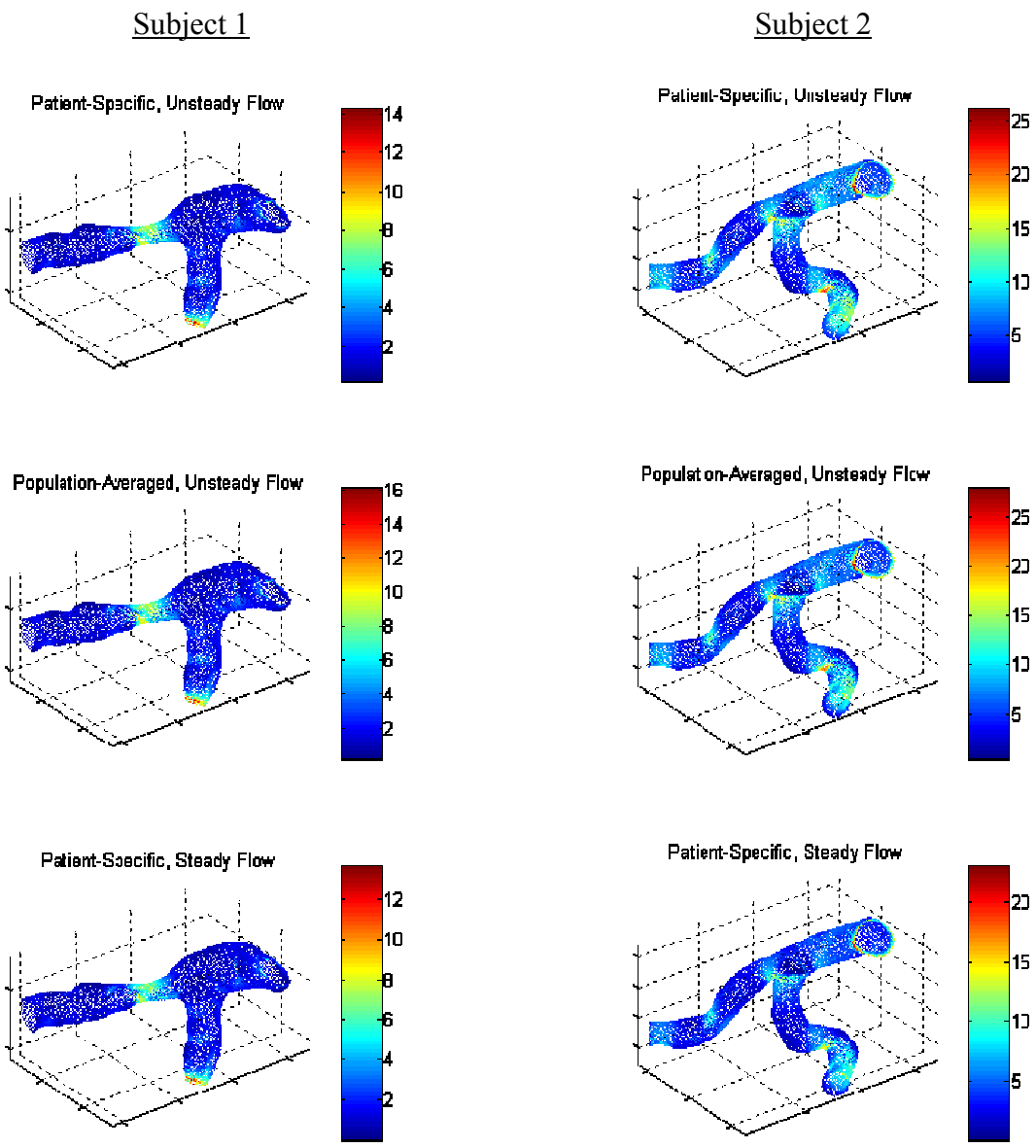

Figure 6.5 Time-averaged WSS for all CFD simulations

t-test. All comparisons found that there was a non-zero difference between each simplified model and the reference standard (for both subjects) at a significance level of less than 1%.

Areas of High/Low WSS Comparison

Regions of high and low time-averaged WSS were defined in each simulation relative to the overall vessel average WSS. Regions were classified as high or low WSS if their magnitude was greater than one standard deviation above of below the whole vessel mean WSS. These regions were then compared between the patient-specific, unsteady flow simulation and the two CFD simulations using simplified velocity boundary conditions of population-averaged, unsteady flow and patient-specific, steady flow. A 'percent coincidence' was defined to measure the accurate representation of high or low WSS regions by the two simplified models. A summary of those results can be found in Table 6.2. The regression equation approximates the relationship between WSS values calculated by the reference standard model and the simplified model – with 'x' being the time-averaged WSS value calculated by the patient-specific, unsteady CFD

Table 6.2 Coincidence of High/Low WSS to Patient-Specific Model

Subject	Boundary Conditions	% Coincidence	Regression	r
1	Population-averaged, Unsteady	99	1.13x + 0.03	0.99
	Steady Flow	93	0.94x – 0.29	0.99
2	Population-averaged, Unsteady	87	1.05x – 0.75	0.99
	Steady Flow	79	0.79x – 1.00	0.99

simulation. Plots showing regions of low or high WSS and the performance of the two simplified models are shown in Figure 6.6.

Figure 6.6 plots regions of high or low WSS as calculated by the reference standard, patient-specific, unsteady simulation compared with the two simplified models. In each figure, areas shown in purple represent regions that were calculated to have high or low WSS by *both* the reference standard and the simplified model. It is this region that is used to calculate the percent coincidence metric. Areas plotted in red denote that an area exhibited high or low WSS in *only* the reference standard CFD simulation and not the simplified model. Regions of blue are areas of high or low WSS in *only* the simplified model that are *not* present in the reference standard model. Visually, percent coincidence is defined as the number of purple nodes divided by the sum of purple and red nodes.

For Subject 1, the population-averaged, unsteady CFD simulation accurately identified 99% of nodes in the vessel model exhibiting high or low WSS by the reference standard boundary conditions. Linear regression analysis of WSS values within these coinciding regions showed a very strong linear correlation (Pearson's correlation coefficient, $r \geq 0.99$) with slope of 1.13 – meaning that, on average, the population-averaged CFD model overestimated WSS calculated using the patient-specific model by 13%. Using patient-specific, steady flow velocity boundary conditions, CFD simulation accurately identified 93% of nodes in the vessel model exhibiting high or low WSS by the gold standard boundary conditions. Linear regression analysis again showed a very strong linear correlation with slope of 0.94 ($r \geq 0.99$).

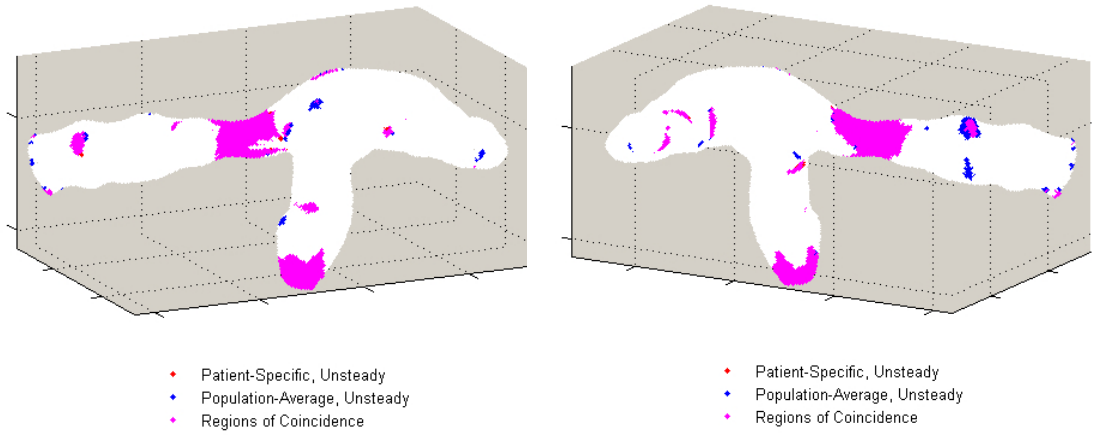

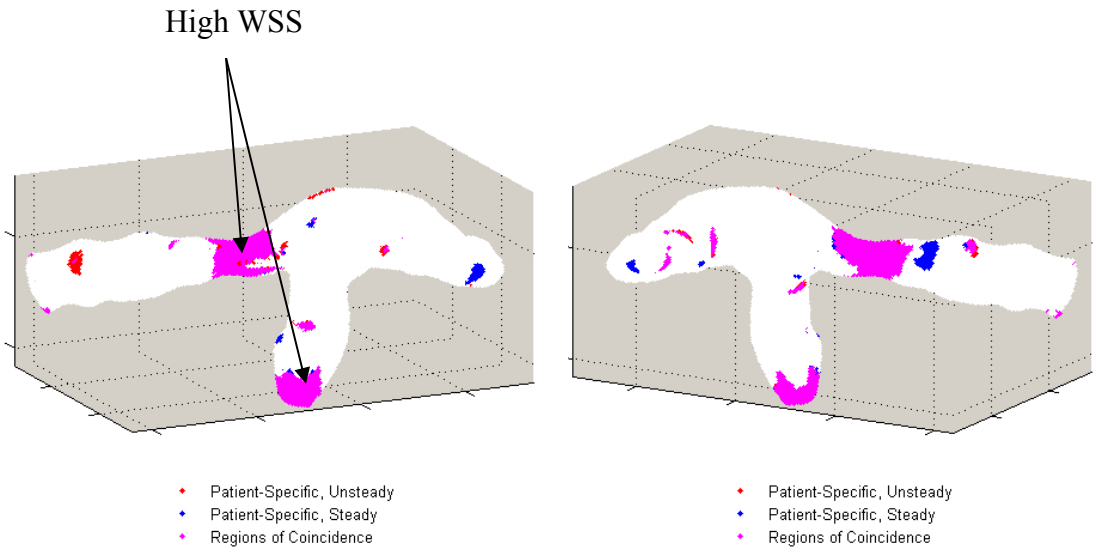

Figure 6.6a Regions of high/low WSS coincidence (Subject 1)

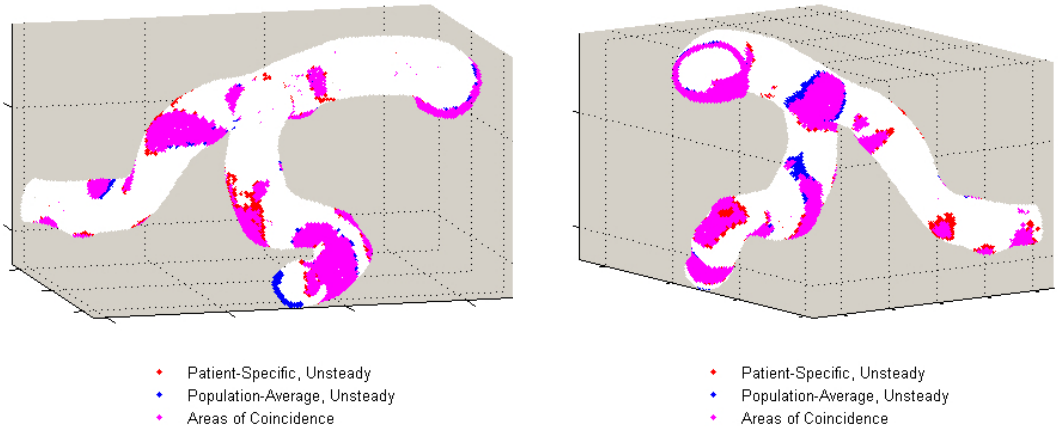

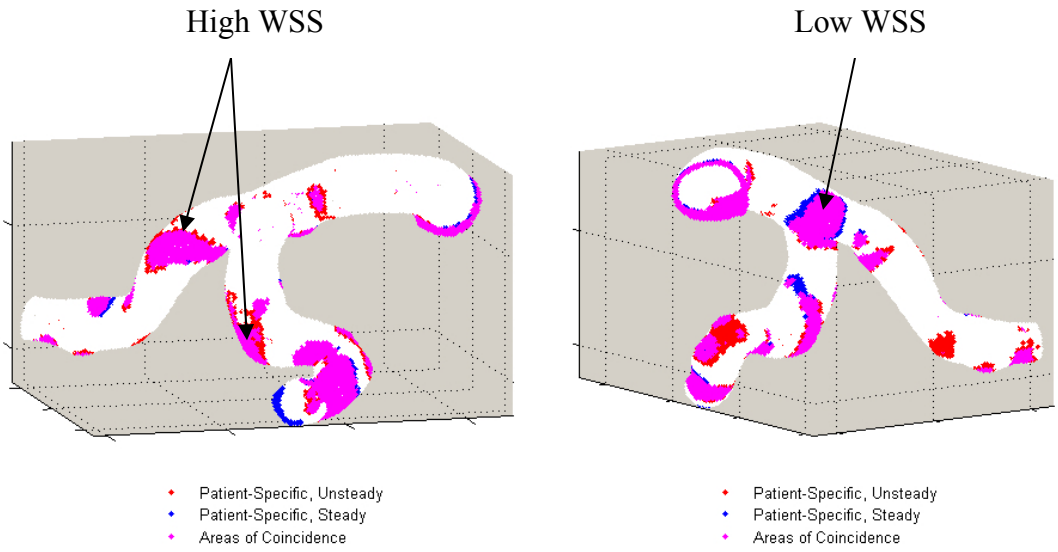

Figure 6.6b Regions of high/low WSS coincidence (Subject 2)

For Subject 2, the population-averaged, unsteady CFD simulation accurately identified 87% of nodes in the vessel model exhibiting high or low WSS by the gold standard boundary conditions. Linear regression analysis showed a very strong linear correlation with slope of 1.05 ($r \geq 0.99$). Using patient-specific, steady flow velocity boundary conditions, CFD simulation accurately identified 79% of nodes in the vessel model exhibiting high or low WSS by the gold standard boundary conditions. Linear regression analysis again showed a very strong linear correlation with slope of 0.79 ($r \geq 0.99$).

Discussion

In this study, a noninvasive, image-based technique was developed to simulate *in vivo* coronary artery blood flow and calculate patient-specific WSS along the LM and proximal regions of the LAD and LCX. This technique uses multi-detector CT for high resolution modeling of coronary artery geometry and 3.0T MR-PVM for temporally resolved measurements of coronary artery blood flow. Spatially and temporally resolved WSS distributions were calculated for two subjects. Time averaged WSS was calculated using patient-specific, time-resolved velocity as well as two simplified velocity boundary conditions. It was determined that neither a population-averaged, time-resolved velocity curve nor patient-specific, steady velocity could accurately reproduce WSS values that had been calculated using the patient-specific, time-resolved CFD model. Areas of locally high or low WSS, however, could be located with high degrees of accuracy using either of the simplified velocity models.

Patient-Specific, Time-Resolved WSS Simulation

Calculated WSS distributions of the two subjects demonstrated several expected characteristics. Subject 1 had a mild stenosis in the proximal LAD. High WSS was observed at this stenosis accompanied by a region of low WSS at the distal shoulder of the stenosis where the vessel diameter increased. Subject 2 had a region of low WSS along the myocardial wall of the LM bifurcation and areas of high WSS along the outer walls of curvature of the LAD and LCX distal to the bifurcation.

Time-Averaged WSS Comparison

Whole vessel average WSS was 2.2 dynes/cm^2 for Subject 1 and 6.1 dynes/cm^2 for Subject 2. Maximum local WSS over the course of the cardiac cycle was 27.7 dynes/cm^2 and 28.1 dynes/cm^2 for Subjects 1 and 2, respectively. These values are in line with whole vessel average (>5 dynes/cm^2) and maximum WSS (35 dynes/cm^2) reported by Jin *et al.* using an unsteady CFD simulation [102]. Soulis, *et al.* performed a steady-state CFD simulation of left coronary blood flow and presented much higher WSS values for the LM and proximal LAD and LCX [103]. Their simulation, however, used a steady flow velocity of 17cm/s, which is more typical of *peak* velocity seen in diastole than a time-averaged velocity. Time-averaged velocity of blood flow measured in our subjects was 4.0cm/s and 3.7cm/s. Using a higher velocity value will naturally lead to higher WSS values.

Areas of High/Low WSS Comparison

A metric of percent coincidence was defined to measure how well CFD simulations using simplified velocity boundary conditions locate areas of regionally high or low WSS compared to a CFD simulation using a patient-specific, unsteady velocity boundary condition. Two simplified boundary conditions were examined: unsteady flow using a population-averaged velocity curve and steady flow using time-averaged, patient-specific velocity measurements. Using the same geometric mesh for each simulation allowed for a point-to-point comparison of over 10,000 nodes for each subject.

For Subject 1, a very strong correlation of areas of low or high WSS was seen between the patient-specific, unsteady CFD model and the two simplified models. Of particular interest for WSS calculation are regions of stenosis. These areas are known to have high WSS at the proximal shoulder and within the stenosis and low WSS at the distal shoulder. Examination of the mildly stenotic region of Figure 6.6a shows that there is almost complete agreement between the reference standard and simplified simulations – indicated by purple coloring with very little red or blue.

The simplified simulations of Subject 2's coronary flow did not perform as well with 87% coincidence using population-averaged, unsteady flow and 79% coincidence using patient-specific, steady flow. Inspection of Figure 6.6b, however, reveals that the simplified CFD simulations did locate the same areas of low or high WSS seen in the patient-specific, unsteady simulation – only with smaller regions in some instances. This is seen in the figure as areas of purple with a red margin – red denoting areas of high or low WSS that the simplified models did not identify.

In a linear regression analysis of WSS magnitude within the aforementioned areas of high or low WSS, use of patient-specific, steady velocity boundary conditions tended to underestimate calculated WSS. Using population-averaged, unsteady velocity boundary conditions overestimated WSS magnitude in both subjects. If more subjects were studied, it is expected that the population-averaged model would also underestimate true WSS in some instances. These results show that, if one is merely interested in locating areas of high or low WSS and not calculating accurate WSS magnitude, using simplified velocity boundary conditions are sufficient to attain that goal.

Limitations

Several limitations must be pointed out in this study. First, only two subjects have been studied. While the qualitative performance of the two simplified CFD models was very good for both subjects, the quantitative *percent coincidence* was somewhat different. Inclusion of more subjects would allow for a better evaluation of the simplified models. The main reason more subjects were not studied was the removal of Emory Hospital's 3.0T magnet. From that point, velocity data could not be measured using 3.0T PC-MRI and the subsequent increase in patient load for the hospital's two 1.5T magnets limited the availability of research time for velocity scans at the lower field strength. Image quality was poor for the PC-MRI velocity scans of Subject 1. Cardiac motion took the cross section of the LM out of the slice plane in a few phases and velocity values for those time points were interpolated from other cardiac phases. In addition, the CT vessel model for Subject 1 was somewhat irregular. The structure of the coronary arteries should be smooth with cross sections roughly circular in shape because all sides of the

vessel wall experience the same pressure. This smooth appearance was demonstrated in Subject 2. The model for Subject 1, however, had several unevenly shaped contours and the vessel had the appearance of a sinewy surface like a muscle. The cause for this is unknown. One possible improvement in this area would be better smoothing of the vessel in the axial direction – either in the surface generation algorithm or by decreasing the space between cross sectional contours. The WSS values reported for Subject 1 are also below those reported in previous studies. This could be due in part to the poor image quality of the PC-MRI scans for that subject. The placement of the velocity inlet at a narrowed region of the LM artery could also decrease the WSS calculations.

Conclusion

The goals of this study were to create an image based, patient-specific CFD model for calculating coronary artery WSS and to determine the necessity of patient-specific, time-resolved velocity boundary conditions for calculating WSS distributions. CFD models were created for two subjects using three-dimensional meshes from segmented vessel contours acquired by a 64-detector CT scan and time-resolved, blood flow velocity measurements acquired by 3.0T MR-PVM. Comparison of WSS calculations from those patient-specific, unsteady flow simulations with simplified simulations show that patient-specific velocity curves are not required to identify regions of the coronary arteries that exhibit low or high WSS. The use of either steady flow or population-averaged, unsteady flow for CFD modeling can allow WSS calculation without the need for MRI velocity measurements that currently exclude many cardiac patients with implanted devices.

CHAPTER 7

CONCLUSIONS

The Problem Revisited

Before providing a summary of the findings from this project, it is appropriate to recall the original goal set forth at the start. As stated in Chapter 1, the overall problem statement reads: "*this thesis intends to evaluate the quantitative accuracy of the imaging modalities involved in creating a patient-specific CFD model of coronary WSS as well as determine the importance of patient-specific flow for such a model.*" Several studies have been presented to accomplish this task involving three different coronary artery imaging modalities and the simulation coronary artery blood flow with a variety of velocity boundary conditions.

Overview of Findings

Chapter 2 provided background information on the suggested causal relationship between atherosclerosis and low or oscillating WSS. An overview was given for the *in vivo* visualization of the coronary arteries using multidetector CT and MRI. It was noted that a void of research existed in the quantitative evaluation of those two imaging modalities due primarily to rapidly changing state-of-the-art technologies and the more qualitative nature of their use in clinical practice. Finally, different methods of modeling coronary artery blood flow and WSS were discussed with a focus on the lack of non-invasive, patient-specific modeling techniques.

Results presented in Chapter 3 established average, three-dimensional trajectories for the three primary coronary arteries during cardiac motion. This was accomplished by the study of bi-planar angiography films of a series of patients. Two important results came from this chapter. First, time-resolved, three-dimensional trajectories were obtained and then used later in Chapter 4 to simulate coronary artery motion. Second, a better understanding of coronary artery motion rest periods was attained. In almost all subjects, a period existed at 72% of the cardiac cycle during which the LAD, LCX, and RCA all exhibited a low degree of motion.

Chapter 4 used the information gained in the previous chapter to evaluate the quantitative accuracy of coronary artery geometry measurements by 64-detector CT. A coronary artery phantom of known dimensions was positioned on a motion stage to simulate *in vivo* coronary artery motion. The vessels were imaged at rest and at different heart rates. Errors in vessel diameter measurement were less than half a millimeter (approximately the length of one pixel) for scans under 70 bpm. Results from this study led to the conclusion that multi-detector CT coronary angiography is capable of generating highly accurate measurements of coronary artery anatomy of large vessels at low heart rates. This validates the first half of the requirements for a patient-specific model of coronary blood flow using CFD. Both the accuracy of measurements and general image quality suffered, however, at faster heart rates and smaller diameter vessels.

Chapter 5 then moved on from coronary geometry to measure the time-resolved velocities of coronary artery blood flow. Protocols were developed for 3.0T phase contrast imaging of the coronary arteries with cardiac and respiratory gating. The

accuracy of velocity measurement by this technique was evaluated using a steady flow phantom and determined to have an average error of 15%. This value is larger than error rates seen for velocity measurement in the aorta and other large diameter vessels – illustrating the importance of spatial resolution relative to the size of the vessel of interest. Errors of less than 20% in these measurements, however, are typically accepted in the clinical setting. Results from CFD simulations in Chapter 6 also show that a high degree of accuracy in velocity measurement may not be necessary for accurate calculation of WSS. In addition to validation of the PC-MRI protocol, the technique was also applied to a series of volunteers to yield average velocity curves for the LAD, LCX, and RCA.

Finally, Chapter 6 detailed the construction of an image-based, patient-specific CFD model of coronary artery flow. A three-dimensional mesh was constructed from segmented 64-detector CT coronary angiography images. Patient-specific, time-resolved coronary velocities were acquired using the PC-MRI protocol outlined in Chapter 5. Distributions of coronary WSS surrounding the left coronary artery bifurcation were then calculated and compared using patient-specific, unsteady velocity boundary conditions and two simplified boundary conditions: a population-averaged, unsteady velocity curve and patient-specific, steady velocity averaged over the subject's cardiac cycle. Results from this comparison for two subjects reveal that while CFD simulations using population-averaged, unsteady velocities were more accurate than steady state simulations, both simplified models were able to locate regions of locally high or low WSS with a high degree of accuracy.

Research Implications

Good research must be able to stand on its own. Beyond that, it should also lend support to further research endeavors. The findings presented in this dissertation offer contributions to several fields of research.

- Three-dimensional, time resolved motion for three segments of the main coronary arteries has been determined. This can be used in several ways. First, further phantom studies can be performed to evaluate other aspects of multidetector CT such as visualization of calcium deposits or stents. These phantom studies can evaluate single scanners or be used to compare capabilities across scanners – such as 64-detector CT and dual-source CT. Time resolved coronary motion can also be applied to advanced CFD modeling of coronary blood flow.
- Average, time resolved velocity curves in the coronary arteries have been reported for the LAD, LCX, and RCA. This data can be used in conjunction with CT geometry as boundary conditions for CFD studies of coronary artery blood flow. This allows study of WSS throughout the coronary arteries and comparison of WSS values to lesion distribution and vessel pathology through either *in vivo* IVUS or histology on explanted coronary arteries.
- The comparison metric of *percent coincidence* can be further used to investigate the effect of different CFD simulation characteristics such as vessel motion, vessel compliance, and different solution schemes. It is important to know what physiological aspects of coronary blood flow are essential to accurate WSS calculation and what aspects offer only minor contributions.

Clinical Implications

One aspect of my research that I have enjoyed over the past five years has been its proximity to the clinical arena. I have worked side-by-side with radiologists, cardiologists, and many wonderful imaging nurses and technicians. In addition to the ability to evaluate new CT technology as mentioned previously, the findings of this dissertation also have clinical implications.

- Identification of "rest periods" during the cardiac cycle will allow clinicians to take advantage of new CT technology such as tube current modulation. This technique decreases the amount of radiation delivered to a patient during periods of the cardiac cycle that will not be reconstructed later for image analysis.
- Similarly, knowing the limitations of CT image quality at high heart rates reinforces the standard clinical use of beta blockers to lower and stabilize patients' heart rates during examination. This will remain an important clinical practice until the temporal resolution of CT imaging is reduced even lower.
- Measurements taken by multidetector CT were shown to have a high degree of accuracy. This finding may lead clinicians to choose CT over invasive coronary angiography techniques as a diagnostic or exploratory tool to evaluate coronary stenoses. The availability of immediate intervention is a distinct advantage for catheterization but CT could certainly be used more as a screening tool.
- Likewise, velocity measurements by 3.0T navigator echo gated PC-MRI were shown to be very accurate. Currently, PC-MRI is used sparingly in the clinical setting; but as the technique develops, future uses could include imaging of

stenotic flow or aneurysm flow and investigation of ventricular contraction abnormalities.

Future Work

Just as this work was built upon the previous efforts of others, the findings presented in these pages present opportunities for further investigation in several areas.

Additional phantom studies of PC-MR could be performed using a motion stage to evaluate the effect of through-plane motion on the measurement of blood flow velocities. Current studies of *in vivo* coronary blood flow sometimes opt to correct for through-plane motion of the heart and sometimes opt not to do so. While subtracting out the motion of surrounding heart tissue certainly affects reported velocity *measurements* – but not the overall flow, the effect of the motion on the real *velocities* remains largely unknown. The motion stage utilized for CT studies in Chapter 4 is not suitable for a high magnetic field environment and so only respiratory motion was simulated in Chapter 5. Adaptations to the motion stage design, such as implemented by Jana Delfino [104], could allow for the imposition of cardiac motion to a coronary vessel flow phantom.

More work should also be done to advance the CFD model of coronary blood flow. This work could go in several different directions. The first would be to increase the number of subjects studied using the current technique. The current study was limited in size due to decreased availability of research time with the MRI scanners and removal of the 3.0T magnet at Emory Hospital. Increasing the size of the study would allow a more thorough analysis of the suitability of simplified velocity boundary conditions for CFD simulation of coronary blood flow.

Improvements can also be made in the formation of the three-dimensional vessel model. While the model of Subject 2 was very smooth with circular or elliptical cross-sections, the model of Subject 1's coronary anatomy had almost a muscular look with irregular cross-sections that could not be reconciled by excluding calcified regions. Improvements in smoothing of both the vessel contours and the length of the vessel would result in a model more comparable to the *in vivo* anatomy.

Another direction would be to increase the complexity of the CFD model. This can be done in a number of ways: expanding the geometry mesh to include the entire left coronary tree, expanding the geometry mesh to include the aorta and model entry flow from the aorta to the coronary arteries, incorporating vessel motion into the CFD model, and incorporating vessel compliance into the CFD model. With the exception of the incorporation of vessel compliance, these conditions have been modeled individually to some extent by other authors without either the high resolution, image-based mesh or patient-specific velocity boundary conditions presented here. Including aortic flow and the distal regions of the coronary artery tree would more closely replicate the *in vivo* condition. Vessel motion and compliance have been shown to be important in modeling flow characteristics of the aorta [75]. Motion of the coronary arteries has been shown to decrease the calculated WSS magnitude in one CFD model [84]; but the affect of vessel compliance in small diameter vessels such as the coronary arteries has not been investigated.

Finally, studies should be conducted toward the original motivation of this research – the correlation of *in vivo* WSS to vessel pathology. Studies can proceed to follow patients on the heart transplant list – even those with implanted devices that

contraindicate examination by MRI. Imaging can be done prior to transplant and then WSS modeling can be compared to histological analysis of the explanted arteries. With careful consideration to issues of radiation dose, this could also be expanded to longitudinal studies to study the change in WSS and atherosclerotic lesion development as vessels age. In this situation, I see promise in the continued improvements in spatial resolution and image quality of MR coronary angiography. Multi-detector computed tomography is currently the superior noninvasive imaging modality for visualization of the coronary arteries and for that reason was chosen for this thesis work; but I believe that advances in 3D MR angiography sequences will be on par with and perhaps surpass the quality of CT in the near future.

Final Thoughts

The domains of bench top or desktop research and the medical clinic continue to be separated by less and less space. Future improvements in the understanding of atherosclerotic lesion pathology may lead to correlations between the type of lesion and its hemodynamic environment – leading in turn to better understanding or prediction of the "vulnerable plaque" opposed to lesions less likely to have an endpoint of vessel occlusion or plaque rupture leading to heart attack or stroke. As *in vitro* studies advance the knowledge of the physiologic characteristics of atherosclerosis and lesion development, it is anticipated that clinical imaging series might be performed on a patient, followed by analysis of the hemodynamic characteristics of the patient's coronary flow, and then followed by either surgical or pharmacological intervention as required. This hemodynamic analysis could one day be incorporated into the image review

workstations currently used for such analyses as 3D reconstruction, multiplanar image reformatting, calcium scoring, contour detection, and cardiac function. This work is further proof of the merging of engineering science with clinical medicine – a trend that is certain to continue to the mutual benefit of researchers and patients alike.

APPENDIX A

MOTION STAGE CODE FOR PROXIMAL LAD

This appendix contains a sample program to encode the trajectory of the proximal segment of the LAD for the Galil Motion Control servo controller as detailed in Chapter 4. Lines beginning with "NOTE" are read by the controller but are not compiled. These lines serve as comments to explain the functioning of the program. In the NOTES sections, command lines are typed in **bold** and user-input variables or values are in *italics*. Executable code must be entered in ALL CAPS. The user-controlled variable 'HRM' manipulates the speed of motion and the simulated heart rate according to Table A.1. This variable must be defined by the user through the command line **>HRM = [*number*]** before execution of the program.

Table A.1 Heart Rate Modification Values

HRM	Heart Rate
1	57
1.1	61
1.25	67
1.7	80

NOTE: Text following '#' denotes the name of a program. The command line **>XQ**

NOTE: **#NAME** will execute all lines of code following the #NAME label until

NOTE: the end command, 'EN', is reached.

#LMLADP

NOTE: The command 'DP' defines the current three-dimensional position of the motion

NOTE: stage to be the three coordinates that follow. In this case, establishing the

NOTE: origin for the experiment.

DP 0,0,0

NOTE: The command 'SH' instructs the motors to turn on. The alternate command 'MO'

NOTE: turns the motors off.

SH

NOTE: The command 'LM' sets the mode of motion definition to Linear Mode for the

NOTE: axes that follow.

LM XYZ

N=0

#LOOP

N=N+1

NOTE: The Linear Interpolation command defines motion in the following way

NOTE: **LI [*3D coordinates for endpoint*] < [*Initial velocity*] > [*Ending velocity*]**

NOTE: and linearly interpolates intermediate velocities for that phase of motion

NOTE: 'HRM' is a user-controlled variable designed to allow easy manipulation of the

NOTE: velocity and in turn the simulated heart rate. Corresponding values of

NOTE: HRM and heart rate are found in Table A.1

LI -4618,-2558,13237 < 71256*HRM > HRM*54471

LI 5614,114,9336 < 54471*HRM > HRM*57359

LI 5788,1891,9722 < 57359*HRM > HRM*49055

LI 6562,2952,6670 < 49055*HRM > HRM*45857

LI 4417,1679,7860 < 45857*HRM > HRM*24299

LI 2277,1148,4137 < 24299*HRM > HRM*53153

LI 9550,4653,382 < 53153*HRM > HRM*29110

LI 3548,3524,-2982 < 29110*HRM > HRM*42764

LI -6547,-3620,-4145 < 42764*HRM > HRM*33558

LI -2970,-1939,-5698 < 33558*HRM > HRM*43803

LI -6815,-122,-5504 < 43803*HRM > HRM*61440

LI -7295,-4002,-9043 < 61440*HRM > HRM*47472

LI -5249,-1269,-7809 < 47472*HRM > HRM*19101

LI -746,-2147,-3071 < 19101*HRM > HRM*24094

LI -1776,-3581,-2692 < 24094*HRM > HRM*20212

LI -3327,-1402,-1818 < 20212*HRM > HRM*40343

LI -3970,-282,-7019 < 40343*HRM > HRM*46563

LI -4958,-3195,-7207 < 46563*HRM > HRM*18039

LI -1658,-2120,2403 < 18039*HRM > HRM*81277

LI 12171,10276,3240 < 81277*HRM > HRM*71256

NOTE: 'LE' denoted the end of the programmed sequence of motion. Motion will not

NOTE: begin until execution of the 'BGS' command

LE

BGS

NOTE: 'SB1' and 'CB1' turn on and off an output voltage channel that serves as a
NOTE: surrogate R-wave that is sent to an ECG converter box that is connected
NOTE: to the CT scanner. The command 'AV 4618' establishes the duration of
NOTE: the voltage pulse. The pulse is turned on at the onset of motion and turned
NOTE: off after the x-axis has traveled a distance of 4618 units – the first motion
NOTE: step
SB1; AV 4618; CB1

NOTE: 'AMS' instructs the controller to wait until the after the commanded motion stops
NOTE: to continue on to the next line of code
AMS

NOTE: The Jump, 'JP', command directs the program to start over at the #LOOP
NOTE: command line if the internal counter variable 'N' is less than 3. In this
NOTE: case for a total of 3 cycles. This condition can be extended to run for any
NOTE: of cycles or the command line can be written only as 'JP #LOOP' for
NOTE: continuous repetition of the cycle until the abort command 'AB' or 'HX'
NOTE: is issued by the user
JP #LOOP, N < 3
EN

APPENDIX B

MATLAB PROGRAMS

This appendix contains copies of selected MATLAB functions that were created during the course of this work and used in analysis of Chapter 6.

SDmask.m

This function was created to extract nodes from the CFD mesh with WSS values greater than or less than one standard deviation above or below the vessel average WSS. The array 'set' exists as a four-dimensional array. The first three columns are the spatial coordinates of each node. The fourth column is the WSS value at the node. The exported array 'set_sd' returns the subset of node coordinates and WSS values.

```
% Function [set_sd]=SDmask(set,num)
% This function reads in a 4D dataset (three spatial coordinates) and creates a subset with
% 4th dimension value greater than 1 stdev above or less than 1 stdev below

function [set_sd]=SDmask(set,num)

if~exist('num')
   num = 1;
end

limit=length(set(:,1));
```

```
avg=mean(set(:,4));
stdev=std(set(:,4));
j=1;

for i=1:limit;
   if set(i,4) > avg + stdev*num
      set_sd(j,:)=set(i,:);
      j=j+1;
   elseif set(i,4) < avg - stdev*num
      set_sd(j,:)=set(i,:);
      j=j+1;
   end
   i=i+1;
end
```

overlap.m

This function was created to compare and check for matches in nodes between two datasets from different CFD simulations. It is used on the subsets of nodes following execution of the SDmask.m program. The export variables [num slope fit] return the 'percent coincidence' metric described in Chapter 6 along with the linear regression coefficients and Pearson's correlation coefficient for WSS values in the coinciding region.

```
% function [num slope fit] = overlap(set1,set2)
% To determine percentage overlap between two WSS datasets
% set1 is standard for comparison
% num = Ratio of 3D points in set2 coincident with points in set1
% slope = Linear regression coeffs for values of coincident datapoints
% fit = Pearson's correlation for values from set1 and set2

function [num slope fit] = overlap(set1,set2)

num=0;
same=0;
 limit = length(set1(:,1));
search = length(set2(:,1));

for i = 1:limit
    for j = 1:search
        if set1(i,1:3) == set2(j,1:3)
            same = same+1;
            match(same,1:4) = set1(i,1:4);
            match(same,5) = set2(j,4);
        end
    end
end

num = same/limit;
slope = polyfit(match(:,4),match(:,5),1);
fit = corr(match(:,4),match(:,5));
```

overlap_plot.m

This function was created to extend the function of overlap.m to include a three-dimensional plot of the coinciding WSS regions along with high/low WSS regions only computed by each respective CFD model. Arrays 'set1' and 'set2" are the same as overlap.m while 'base' is an array containing nodes of the entire vessel and serves as the background against which the colored regions are plotted.

```
% overlap_plot
% Program to display 3D vessel structure with regions of high/low WSS
%   Normal WSS displayed in grey
%   Patient-specific high/low WSS in red
%   Comparison high/low WSS in blue
%   Overlap between the two models in purple

function [bkgrd just1 just2 match] = overlap_plot(set1, set2, base)

same1 = 0;
notsame1 = 0;
 limit = length(set1(:,1));
search = length(set2(:,1));


for i = 1:limit
   check = 0;
   for j = 1:search
      if set1(i,1:3) == set2(j,1:3)
         same1 = same1 + 1;
```

```
            match(same1,1:3) = set1(i,1:3);
            check = 1;
        end
    end

    if check == 0
        notsame1 = notsame1 + 1;
        just1(notsame1,1:3) = set1(i,1:3);
    end
end


same2 = 0;
notsame2 = 0;

for i = 1:search
    check = 0;
    for j = 1:limit
        if set2(i,1:3) == set1(j,1:3)
            same2 = same2 + 1;
            check = 1;
        end
    end

    if check == 0
        notsame2 = notsame2 + 1;
        just2(notsame2,1:3) = set2(i,1:3);
```

```
    end
end

combined(:,1:3) = [match(:,1:3);just1(:,1:3);just2(:,1:3)];
comb = length(combined(:,1));
total = length(base(:,1));
notsame3 = 0;

for i = 1:total
    check = 0;
    for j = 1:comb
        if base(i,1:3) == combined(j,1:3)
            check = 1;
        end
    end

    if check == 0
        notsame3 = notsame3 + 1;
        bkgrd(notsame3,1:3) = base(i,1:3);
    end
end

figure; hold; grid on;
plot3(bkgrd(:,1),bkgrd(:,2),bkgrd(:,3),'.w')
plot3(just1(:,1),just1(:,2),just1(:,3),'.r')
plot3(just2(:,1),just2(:,2),just2(:,3),'.b')
plot3(match(:,1),match(:,2),match(:,3),'.m')
```

REFERENCES

1. Johnson, K.R., et al., *Three-dimensional, time-resolved motion of the coronary arteries.* J Cardiovasc Magn Reson, 2004. **6**(3): p. 663-73.

2. Fuster, V., *Human lesion studies.* Ann N Y Acad Sci, 1997. **811**: p. 207-24; discussion 224-5.

3. Casscells, W., M. Naghavi, and J.T. Willerson, *Vulnerable atherosclerotic plaque: a multifocal disease.* Circulation, 2003. **107**(16): p. 2072-5.

4. Nerem, R.M., et al., *The study of the influence of flow on vascular endothelial biology.* American Journal of the Medical Sciences, 1998. **316**(3): p. 169-75.

5. Nerem, R.M., M.J. Levesque, and J.F. Cornhill, *Vascular endothelial morphology as an indicator of the pattern of blood flow.* J Biomech Eng, 1981. **103**(3): p. 172-6.

6. Resnick, N., et al., *Fluid shear stress and the vascular endothelium: for better and for worse.* Prog Biophys Mol Biol, 2003. **81**(3): p. 177-99.

7. Carmeliet, P., et al., *Targeted deficiency or cytosolic truncation of the VE-cadherin gene in mice impairs VEGF-mediated endothelial survival and angiogenesis.* Cell, 1999. **98**(2): p. 147-57.

8. Dejana, E., R. Spagnuolo, and G. Bazzoni, *Interendothelial junctions and their role in the control of angiogenesis, vascular permeability and leukocyte transmigration.* Thromb Haemost, 2001. **86**(1): p. 308-15.

9. Schwartz, M.A. and M.H. Ginsberg, *Networks and crosstalk: integrin signalling spreads.* Nat Cell Biol, 2002. **4**(4): p. E65-8.

10. Shyy, J.Y. and S. Chien, *Role of integrins in cellular responses to mechanical stress and adhesion.* Curr Opin Cell Biol, 1997. **9**(5): p. 707-13.

11. Haga, M., et al., *Shear stress and cyclic strain may suppress apoptosis in endothelial cells by different pathways.* Endothelium, 2003. **10**(3): p. 149-57.

12. Jo, H., et al., *Differential effect of shear stress on extracellular signal-regulated kinase and N-terminal Jun kinase in endothelial cells. Gi2- and Gbeta/gamma-dependent signaling pathways.* Journal of Biological Chemistry, 1997. **272**(2): p. 1395-401.

13. Caro, C.G., J.M. Fitz-Gerald, and R.C. Schroter, *Atheroma and arterial wall shear. Observation, correlation and proposal of a shear dependent mass transfer mechanism for atherogenesis.* Proc R Soc Lond B Biol Sci, 1971. **177**(46): p. 109-59.

14. Clowes, A.W. and S.A. Berceli, *Mechanisms of vascular atrophy and fibrous cap disruption.* Ann N Y Acad Sci, 2000. **902**: p. 153-61; discussion 161-2.

15. Glagov, S., et al., *Hemodynamics and atherosclerosis. Insights and perspectives gained from studies of human arteries.* Arch Pathol Lab Med, 1988. **112**(10): p. 1018-31.

16. Haruguchi, H. and S. Teraoka, *Intimal hyperplasia and hemodynamic factors in arterial bypass and arteriovenous grafts: a review.* J Artif Organs, 2003. **6**(4): p. 227-35.

17. Ku, D.N., et al., *Pulsatile flow and atherosclerosis in the human carotid bifurcation. Positive correlation between plaque location and low oscillating shear stress.* Arteriosclerosis, 1985. **5**(3): p. 293-302.

18. Lehoux, S., F. Tronc, and A. Tedgui, *Mechanisms of blood flow-induced vascular enlargement.* Biorheology, 2002. **39**(3-4): p. 319-24.

19. Loth, F., et al., *Relative contribution of wall shear stress and injury in experimental intimal thickening at PTFE end-to-side arterial anastomoses.* J Biomech Eng, 2002. **124**(1): p. 44-51.

20. Caro, C.G., J.M. Fitz-Gerald, and R.C. Schroter, *Arterial wall shear and distribution of early atheroma in man.* Nature, 1969. **223**(211): p. 1159-60.

21. Cornhill, J.F. and M.R. Roach, *A quantitative study of the localization of atherosclerotic lesions in the rabbit aorta.* Atherosclerosis, 1976. **23**(3): p. 489-501.

22. Glagov, S., *Hemodynamic factors in localisation of atherosclerosis.* Acta Cardiol, 1965: p. Suppl 11:311+.

23. Glagov, S. and A.K. Ozoa, *Significance of the relatively low incidence of atherosclerosis in the pulmonary, renal, and mesenteric arteries.* Ann N Y Acad Sci, 1968. **149**(2): p. 940-55.

24. Friedman, M.H., et al., *Correlation between intimal thickness and fluid shear in human arteries.* Atherosclerosis, 1981. **39**(3): p. 425-36.

25. Malek, A.M., S.L. Alper, and S. Izumo, *Hemodynamic shear stress and its role in atherosclerosis.* Jama, 1999. **282**(21): p. 2035-42.

26. Zarins, C.K., et al., *Carotid bifurcation atherosclerosis. Quantitative correlation of plaque localization with flow velocity profiles and wall shear stress.* Circulation Research, 1983. **53**(4): p. 502-14.

27. Reig, J. and M. Petit, *Main trunk of the left coronary artery: anatomic study of the parameters of clinical interest.* Clin Anat, 2004. **17**(1): p. 6-13.

28. Krone, R.J., L. Johnson, and T. Noto, *Five year trends in cardiac catheterization: a report from the Registry of the Society for Cardiac Angiography and Interventions.* Cathet Cardiovasc Diagn, 1996. **39**(1): p. 31-5.

29. Krams, R., et al., *Evaluation of endothelial shear stress and 3D geometry as factors determining the development of atherosclerosis and remodeling in human coronary arteries in vivo. Combining 3D reconstruction from angiography and IVUS (ANGUS) with computational fluid dynamics.* Arterioscler Thromb Vasc Biol, 1997. **17**(10): p. 2061-5.

30. Oshinski, J.N., et al., *Two-dimensional coronary MR angiography without breath holding.* Radiology, 1996. **201**(3): p. 737-43.

31. Achenbach, S., et al., *Detection of coronary artery stenoses by contrast-enhanced, retrospectively electrocardiographically-gated, multislice spiral computed tomography.* Circulation, 2001. **103**(21): p. 2535-8.

32. Achenbach, S., et al., *Noninvasive coronary angiography by retrospectively ECG-gated multislice spiral CT.* Circulation, 2000. **102**(23): p. 2823-8.

33. Kim, W.Y., et al., *Coronary magnetic resonance angiography for the detection of coronary stenoses.* N Engl J Med, 2001. **345**(26): p. 1863-9.

34. Ohnesorge, B., et al., *Cardiac Imaging by Means of Electrocardiographically Gated Multisection Spiral CT: Initial Experience.* Radiology, 2000. **217**: p. 564-571.

35. Kopp, A., et al., *Coronary Arteries: Retrospectively ECG-Gated Multi-Detector Row CT Angiography with Selective Optimization of the Image Reconstruction Window.* Radiology, 2001. **221**: p. 683-688.

36. Kachelrieβ, M., S. Ulzheimer, and W.A. Kalendar, *ECG-correlated image reconstruction from subsecond multi-slice spiral CT scans of the heart.* Med Phys, 2000. **27**: p. 1881-1902.

37. Flohr, T. and B. Ohnesorge, *Heart rate adaptive optimization of spatial and temporal resolution for electrocardiogram-gated multislice spiral CT of the heart.* Journal of Computer Assisted Tomography, 2001. **25**(6): p. 907-23.

38. Pelc, N.J., et al., *Phase contrast cine magnetic resonance imaging.* Magn Reson Q, 1991. **7**(4): p. 229-54.

39. Rebergen, S.A., et al., *Magnetic resonance measurement of velocity and flow: technique, validation, and cardiovascular applications.* Am Heart J, 1993. **126**(6): p. 1439-56.

40. Bi, X. and D. Li, *Coronary arteries at 3.0 T: Contrast-enhanced magnetization-prepared three-dimensional breathhold MR angiography.* J Magn Reson Imaging, 2005. **21**(2): p. 133-9.

41. Weber, O.M., et al., *Free-breathing, three-dimensional coronary artery magnetic resonance angiography: comparison of sequences.* J Magn Reson Imaging, 2004. **20**(3): p. 395-402.

42. Cheng, L., et al., *Breath-hold 3D steady-state free precession coronary MRA compared with conventional X-ray coronary angiography.* J Magn Reson Imaging, 2006. **23**(5): p. 669-73.

43. Lethimonnier, F., et al., *Three-dimensional coronary artery MR imaging using prospective real-time respiratory navigator and linear phase shift processing: comparison with conventional coronary angiography.* Magn Reson Imaging, 1999. **17**(8): p. 1111-20.

44. Plein, S., et al., *Three-dimensional coronary MR angiography performed with subject-specific cardiac acquisition windows and motion-adapted respiratory gating.* AJR Am J Roentgenol, 2003. **180**(2): p. 505-12.

45. Sommer, T., et al., *Coronary MR angiography at 3.0 T versus that at 1.5 T: initial results in patients suspected of having coronary artery disease.* Radiology, 2005. **234**(3): p. 718-25.

46. Gerber, B.L., et al., *Coronary artery stenosis: direct comparison of four-section multi-detector row CT and 3D navigator MR imaging for detection--initial results.* Radiology, 2005. **234**(1): p. 98-108.

47. Kefer, J., et al., *Head-to-head comparison of three-dimensional navigator-gated magnetic resonance imaging and 16-slice computed tomography to detect coronary artery stenosis in patients.* J Am Coll Cardiol, 2005. **46**(1): p. 92-100.

48. Jahnke, C., et al., *Coronary MR imaging: breath-hold capability and patterns, coronary artery rest periods, and beta-blocker use.* Radiology, 2006. **239**(1): p. 71-8.

49. Oshinski, J.N., et al., *Two-Dimensional MR Angiography of the Coronary Arteries without Breath-holding.* Radiology, 1996. **201**: p. 737-743.

50. Keegan, J., et al., *The application of breath hold phase velocity mapping techniques to the measurement of coronary artery blood flow velocity: phantom data and initial in vivo results.* Magn Reson Med, 1994. **31**(5): p. 526-36.

51. Nagel, E., et al., *Noninvasive determination of coronary blood flow velocity with magnetic resonance imaging: comparison of breath-hold and navigator techniques with intravascular ultrasound.* Magn Reson Med, 1999. **41**(3): p. 544-9.

52. Wang, Y., et al., *Coronary MR Angiography: Selection of Acquisition Window of Minimal Cardiac Motion with Electrocardiographically-triggered Navigator Cardiac Motion Prescanning - Initial Results.* Radiology, 2001. **218**: p. 580-585.

53. Kim, W.Y., et al., *Impact of Bulk Cardiac Motion on Right Coronary MR Angiography and Vessel Wall Imaging.* Journal of Magnetic Resonance Imaging, 2001. **14**: p. 383-390.

54. Kilner, P.J., et al., *Valve and great vessel stenosis: assessment with MR jet velocity mapping.* Radiology, 1991. **178**(1): p. 229-35.

55. Gatehouse, P.D., et al., *Applications of phase-contrast flow and velocity imaging in cardiovascular MRI.* Eur Radiol, 2005. **15**(10): p. 2172-84.

56. Rebergen, S.A., et al., *Postoperative pulmonary flow dynamics after Fontan surgery: assessment with nuclear magnetic resonance velocity mapping.* J Am Coll Cardiol, 1993. **21**(1): p. 123-31.

57. Bakker, C.J., et al., *Accuracy and precision of time-averaged flow as measured by nontriggered 2D phase-contrast MR angiography, a phantom evaluation.* Magn Reson Imaging, 1995. **13**(7): p. 959-65.

58. Chatzimavroudis, G.P., et al., *Evaluation of the precision of magnetic resonance phase velocity mapping for blood flow measurements.* J Cardiovasc Magn Reson, 2001. **3**(1): p. 11-9.

59. Evans, A.J., et al., *Magnetic resonance imaging of blood flow with a phase subtraction technique. In vitro and in vivo validation.* Invest Radiol, 1993. **28**(2): p. 109-15.

60. Hoogeveen, R.M., C.J. Bakker, and M.A. Viergever, *Limits to the accuracy of vessel diameter measurement in MR angiography.* J Magn Reson Imaging, 1998. **8**(6): p. 1228-35.

61. Tang, C., D.D. Blatter, and D.L. Parker, *Accuracy of phase-contrast flow measurements in the presence of partial-volume effects.* J Magn Reson Imaging, 1993. **3**(2): p. 377-85.

62. Nagel, E., et al., *Noninvasive determination of coronary blood flow velocity with cardiovascular magnetic resonance in patients after stent deployment.* Circulation, 2003. **107**(13): p. 1738-43.

63. Delfino, J.G., et al., *Comparison of myocardial velocities obtained with magnetic resonance phase velocity mapping and tissue doppler imaging in normal subjects and patients with left ventricular dyssynchrony.* J Magn Reson Imaging, 2006.

64. Gutberlet, M., et al., *Comprehensive cardiac magnetic resonance imaging at 3.0 Tesla: feasibility and implications for clinical applications.* Invest Radiol, 2006. **41**(2): p. 154-67.

65. Gutberlet, M., et al., *Comparison of different cardiac MRI sequences at 1.5 T/3.0 T with respect to signal-to-noise and contrast-to-noise ratios - initial experience.* Rofo, 2004. **176**(6): p. 801-8.

66. Lotz, J., et al., *In vitro validation of phase-contrast flow measurements at 3 T in comparison to 1.5 T: precision, accuracy, and signal-to-noise ratios.* J Magn Reson Imaging, 2005. **21**(5): p. 604-10.

67. Doriot, P.A., et al., *In-vivo measurements of wall shear stress in human coronary arteries.* Coron Artery Dis, 2000. **11**(6): p. 495-502.

68. Tang, C., D. Blatter, and D.L. Parker, *Accuracy of phase contrast flow measurements in the presence of partial volume effects.* J Mag Res Imag, 1993. **3**: p. 337-385.

69. Frayne, R. and B.K. Rutt, *Measurement of fluid-shear rate by Fourier-encoded velocity imaging.* Magn Reson Med, 1995. **34**(3): p. 378-87.

70. Lou, Z., W.J. Yang, and P.D. Stein, *Errors in the estimation of arterial wall shear rates that result from curve fitting of velocity profiles.* J Biomech, 1993. **26**(4-5): p. 383-90.

71. Oshinski, J.N., et al., *Determination of wall shear stress in the aorta with the use of MR phase velocity mapping.* J Magn Reson Imaging, 1995. **5**(6): p. 640-7.

72. Oyre, S., et al., *Quantitation of circumferential subpixel vessel wall position and wall shear stress by multiple sectored three-dimensional paraboloid modeling of velocity encoded cine MR.* Magn Reson Med, 1998. **40**(5): p. 645-55.

73. Pipe, J.G., *A simple measure of flow disorder and wall shear stress in phase contrast MRI.* Magn Reson Med, 2003. **49**(3): p. 543-50.

74. Milner, J.S., et al., *Hemodynamics of human carotid artery bifurcations: computational studies with models reconstructed from magnetic resonance imaging of normal subjects.* J Vasc Surg, 1998. **28**(1): p. 143-56.

75. Jin, S., J. Oshinski, and D.P. Giddens, *Effects of wall motion and compliance on flow patterns in the ascending aorta.* J Biomech Eng, 2003. **125**(3): p. 347-54.

76. Glor, F.P., et al., *Reproducibility study of magnetic resonance image-based computational fluid dynamics prediction of carotid bifurcation flow.* Ann Biomed Eng, 2003. **31**(2): p. 142-51.

77. Kaazempur-Mofrad, M.R., et al., *Characterization of the atherosclerotic carotid bifurcation using MRI, finite element modeling, and histology.* Ann Biomed Eng, 2004. **32**(7): p. 932-46.

78. Papathanasopoulou, P., et al., *MRI measurement of time-resolved wall shear stress vectors in a carotid bifurcation model, and comparison with CFD predictions.* J Magn Reson Imaging, 2003. **17**(2): p. 153-62.

79. Thomas, J.B., et al., *Reproducibility of image-based computational fluid dynamics models of the human carotid bifurcation.* Ann Biomed Eng, 2003. **31**(2): p. 132-41.

80. Younis, H.F., et al., *Hemodynamics and wall mechanics in human carotid bifurcation and its consequences for atherogenesis: investigation of inter-individual variation.* Biomech Model Mechanobiol, 2004. **3**(1): p. 17-32.

81. Stone, P.H., et al., *Effect of endothelial shear stress on the progression of coronary artery disease, vascular remodeling, and in-stent restenosis in humans: in vivo 6-month follow-up study.* Circulation, 2003. **108**(4): p. 438-44.

82. Feldman, C.L., et al., *Determination of in vivo velocity and endothelial shear stress patterns with phasic flow in human coronary arteries: a methodology to predict progression of coronary atherosclerosis.* Am Heart J, 2002. **143**(6): p. 931-9.

83. Johnston, B.M., et al., *Non-Newtonian blood flow in human right coronary arteries: transient simulations.* J Biomech, 2006. **39**(6): p. 1116-28.

84. Ramaswamy, S.D., et al., *Fluid dynamic analysis in a human left anterior descending coronary artery with arterial motion.* Ann Biomed Eng, 2004. **32**(12): p. 1628-41.

85. Kyriakidis, M., et al., *Sex Differences in the Anatomy of Coronary Artery Disease.* J Clin Epidemiol, 1995. **48**(6): p. 723-730.

86. Montenegro, M.R. and D.A. Eggen, *Topography of atherosclerosis in the coronary arteries.* Lab Invest, 1968. **18**: p. 125-133.

87. Mollet, N.R., F. Cademartiri, and P.J. de Feyter, *Non-invasive multislice CT coronary imaging.* Heart, 2005. **91**(3): p. 401-7.

88. Caussin, C., et al., *Comparison of coronary minimal lumen area quantification by sixty-four-slice computed tomography versus intravascular ultrasound for intermediate stenosis.* Am J Cardiol, 2006. **98**(7): p. 871-6.

89. Ferencik, M., et al., *Improved vessel morphology measurements in contrast-enhanced multi-detector computed tomography coronary angiography with non-linear post-processing.* Eur J Radiol, 2006. **57**(3): p. 380-3.

90. Shim, S.S., Y. Kim, and S.M. Lim, *Improvement of image quality with beta-blocker premedication on ECG-gated 16-MDCT coronary angiography.* AJR Am J Roentgenol, 2005. **184**(2): p. 649-54.

91. Ferencik, M., et al., *Quantitative parameters of image quality in 64-slice computed tomography angiography of the coronary arteries.* Eur J Radiol, 2006. **57**(3): p. 373-9.

92. Walker, P.G., et al., *Semiautomated method for noise reduction and background phase error correction in MR phase velocity data.* J Magn Reson Imaging, 1993. **3**(3): p. 521-30.

93. van der Geest, R.J., et al., *Automated measurement of volume flow in the ascending aorta using MR velocity maps: evaluation of inter- and intraobserver variability in healthy volunteers.* J Comput Assist Tomogr, 1998. **22**(6): p. 904-11.

94. Weber, O.M., A.J. Martin, and C.B. Higgins, *Whole-heart steady-state free precession coronary artery magnetic resonance angiography.* Magn Reson Med, 2003. **50**(6): p. 1223-8.

95. Berne, R.M. and M.N. Levy, *Cardiovascular Physiology*. 7th ed. 1997, St. Louis: Mosby-Year Book.

96. Jin, S., *Investigation of Blood Flow Patterns and Hemodynamics in the Human Ascending Aorta and Major Trunks of Right and Left Coronary Arteries Using Magnetic Resonance Imaging and Computational Fluid Dynamics*, in *Department of Bioengineering*. 2005, Georgia Institute of Technology: Atlanta.

97. Keegan, J., et al., *Comparison of spiral and FLASH phase velocity mapping, with and without breath-holding, for the assessment of left and right coronary artery blood flow velocity.* J Magn Reson Imaging, 2004. **19**(1): p. 40-9.

98. Schiemann, M., et al., *MR-based coronary artery blood velocity measurements in patients without coronary artery disease.* Eur Radiol, 2006. **16**(5): p. 1124-30.

99. Hofman, M.B., et al., *Assessment of flow in the right human coronary artery by magnetic resonance phase contrast velocity measurement: effects of cardiac and respiratory motion.* Magn Reson Med, 1996. **35**(4): p. 521-31.

100. Marcus, J.T., et al., *Flow profiles in the left anterior descending and the right coronary artery assessed by MR velocity quantification: effects of through-plane and in-plane motion of the heart.* J Comput Assist Tomogr, 1999. **23**(4): p. 567-76.

101. Jin, S., J.N. Oshinski, and D.P. Giddens, *Effects of inflow conditions and wall motion on flow in the ascending aorta.* ASME BED, 2001. **50**: p. 13-14.

102. Jin, S., et al., *Flow Patterns and Wall Shear Stress Distributions at Atherosclerotic-Prone Sites in a Human Left Coronary Artery - An Exploration Using Combined Methods of CT and Computational Fluid Dynamics.* Conf Proc IEEE Eng Med Biol Soc, 2004. **5**(1): p. 3789-3791.

103. Soulis, J.V., et al., *Wall shear stress in normal left coronary artery tree.* J Biomech, 2006. **39**(4): p. 742-9.

104. Delfino, J.G., et al., *Three directional myocardial phase contrast tissue velocity imaging without breath holding: an in vivo and in vitro study.* Radiology, in press.